Prompt Gamma-ray 3D-Imaging for Cultural Heritage Purposes

Inaugural-Dissertation zur Erlangung des Doktorgrades
der Mathematisch-Naturwissenschaftlichen Fakultät
der Universität zu Köln

vorgelegt von
Ralf Schulze
aus Lemgo

Köln 2010

Berichterstatter:	Prof. Dr. J. Jolie Prof. Dr. A. Eckart
Tag der mündlichen Prüfung:	5.7.2010

There is something fascinating about science. One gets such wholesale returns of conjecture out of such a trifling investment of fact.

MARK TWAIN

Kurzzusammenfassung

Die Entwicklung von neuen und die Verbesserung existerender element-sensitiver, bildgebender Verfahren mit Hilfe von Neutronen verschiedener Energiebereiche war das Ziel des europäischen ANCIENT CHARM-Projektes. Während der vorliegenden Arbeit wurde als Teil dieses Projektes die Station für Prompte-Gamma-Aktivierungs-Analyse (PGAA) am Forschungsreaktor FRM 2 in Garching bei München modifiziert, um die ortsauflösende Bestimmung elementare Verteilungen zu ermöglichen. Da sich die PGAA-Station am FRM 2 zu Beginn der Arbeit noch in der Fertigstellung befand wurden erste Tests und die Erarbeitung von ersten Kalibrierungs- und Messprozeduren für die neue bildgebende Methode von der Budapester PGAA-Gruppe in Kooperation mit dem Institut für Kernphysik der Universität zu Köln am Budapester Forschungsreaktor vorgenommen. Auf Grund des höheren Neutronenflusses der Garchinger PGAA-Station wurden nach der regulären Inbetriebnahme der Station die benötigten Gerätschaften vom Budapester Reaktor zum FRM 2 verlegt. Dort wurden weitere Optimierungen vorgenommen und die Eigenschaften des Aufbaus charakterisiert. Nach ersten Testmessungen mit Repliken von archäologischen Objekten wurden mehrere Messungen an echten Objekten von ärchäologischem Interesse durchgeführt und analysiert. Hierbei wurden verschiedenen Messkonfigurationen angewendet. Neben bildgebenden 2D- und 3D-Messungen wurde auch eine neue Anwendung zur Messung dünner Oberflächenschichten im Bereich von eingen 100 μm entwickelt.

Für die quantitative Bestimmung von elementaren Verteilungen ist u. a. die genaue Kenntnis des Neutronenflusses an jeder gemessenen Position innerhalb der analysierten Probe nötig. Mit Hilfe der etablierten Methode der kalten Neutronen-Tomographie (NT) wurde ein Verfahren mit zugehöriger Software entwickelt, durch welches sich der erwartete Neutronenfluss innerhalb von Proben aus der mit NT gemessenen Abschwächungs-Verteilung für kalte Neutronen bestimmen lässt.

Zur regulären Inbetriebnahme der PGAA-Station am Garchinger Forschungsreaktor wurde u. a. ein neues Datenaufnahmesystem beigetragen, welches sowohl traditionelle PGAA-Messungen, als auch Messungen mit der neuen Methode der bildgebenden PGA erlaubt. Durch die hohe Automatisierung erlaubt die neue Datenaufnahme einen deutlich effektiveren Betrieb der PGAA-Station, als es bisher der Fall war.

Die neue, momentan am Institut für Kernphysik der Universität zu Köln entwickelte Software für die Analyse von γ-Spektren „HDTV“ wurde um einige Funktionalität zur Analyse von PGAA-Spektren erweitert. „HDTV“ ist als zukünftiger moderner Nachfolger für die bisher genutzte Software „TV“ vorgeschlagen und erleichtert bspw. die halb-automatische Analyse von vielen, ähnlichen γ-Spektren, was für das neue bildgebende PGA-Verfahren essenziell ist.

Abstract

The development of new, and the enhancement of existing element-sensitive imaging methods utilizing neutrons of different energy regions was the aim of the European ANCIENT CHARM project. During the present work the setup for Prompt Gamma-ray Activation Analysis (PGAA) at the research reactor FRM 2 in Garching near Munich was modified to enable the spatial mapping of elemental abundances in the analysed samples. Because the PGAA setup at FRM 2 was under construction at the beginning of the project first tests and the development of calibration and measurement procedures for the new imaging method were done by the PGAA group at the Budapest Research Reactor in cooperation with the Institute for Nuclear Physics of the University of Cologne. Due to the higher neutron flux at the PGAA setup at FRM 2 the equipment was transferred from the Budapest Research Reactor to FRM 2 after the PGAA setup at FRM 2 started its regular operation. After further optimizations and the characterization of the setup, measurements were started on replicas of real archaeological objects before several measurements on real objects were performed and analysed. Several measurement configurations were applied. Additional to 2D and 3D imaging measurements a new application for the measurement of thin surface layers in the order of a few 100 µm was developed.

For the quantitative analysis of elemental distributions the exact knowledge of the neutron flux at each measured position in the analysed sample has to be known. Based on the well-established cold Neutron Tomography (NT) method a method and software have been developed, which enables the calculation of the neutron flux inside samples with the map of attenuation properties obtained through NT.

A new data acquisition system was developed for the regular operation of the PGAA setup at FRM 2, which supports traditional bulk PGAA measurements as well as measurements in the new imaging configuration. The high automation of the system allows a significantly more efficient use of the available measurement time than it was the case before.

The new software “HDTV” for the analysis of γ-ray spectra, which is currently under active development at the Institute for Nuclear Physics of the University of Cologne, was extended by some functionality for the analysis of PGAA spectra. It is a proposed modern successor of the currently used software “TV” and allows the semi-automatic analysis of multiple, similar spectra, what is essential for the new imaging PGA method.

Contents

1. Introduction

1.1. The use of neutrons for imaging purposes

The neutron is an ideal probe for the elemental and structural analysis of objects from multiple fields of interest, e.g. geology, crystallography, or archaeology. As chargeless particles the penetratoin depth of neutrons is large compared to e.g. X-rays or protons and, depending on the used method, they can deliver the quantitative elemental composition of an investigated sample. Because neutrons interact with the nucleus, they can be used to identify different isotopes of one element.

Neutrons are in wide use for the bulk elemental, crystallographic or morphological analysis, but only few methods are established for position sensitive elemental distribution measurements [Spy87, SK87, Bal96, Bae01, Kar03]. It was thus seen as desirable to form a collaboration for the joint development of new, non-destructive, element sensitive, 3D neutron imaging methods.

1.2. The ANCIENT CHARM project

In 2006 the European ANCIENT CHARM[1] project [Gor07] started as a collaboration of ten European Institutes (tab. 1.1) from the fields of physics and radiochemistry, archaeology, restoration and conservation, and crystallography. The aim of ANCIENT CHARM was the improvement of existing, and development of new neutron based 3D elemental imaging methods for the purpose of cultural heritage studies. The main methods used during the project were (cold) Neutron Tomography (NT), Prompt Gamma-ray Activation Analysis (PGAA) which has been developed into the imaging method Prompt Gamma-ray Activation Imaging (PGAI), Neutron Resonant Capture Analysis (NRCA) with the corresponding imaging method Neutron Resonant Capture Imaging (NRCI), and the newly developed Neutron Resonant (Transmission) Tomography (NRT).

Special focus was put on the combined analysis of the data-sets from the different methods with the aim of compensating the disadvantages of one methods with the results obtained through another method. E.g. NT is a method, which acquires highly resolved ($\approx 100-500\,\mu$m) 3D images in a relatively short time, but does not deliver elemental compositions. PGAI on the other hand has a much lower resolution ($\approx 3-6$ mm) and requires much longer measurement times, but is able to deliver spatial elemental information. With the combination of these two methods (PGAI/NT), it is possible in some cases to obtain a quite accurate, high resolution elemental dis-

[1] **A**nalysis by **N**eutron resonant **C**apture **I**maging and other **E**merging **N**eutron **T**echniques: new **C**ultural **H**eritage and **A**rchaeological **R**esearch **M**ethods: http://ancient-charm.neutron-eu.net/ach/

Table 1.1.: List of institutes that participated in the ANCIENT CHARM project

Institute	City	Country
Universitá degli Studi di Milano-Bicocca	Milan	Italy
Universitá degli Studi di Roma Tor Vergata	Rome	Italy
Hungarian National Museum	Budapest	Hungary
Institute of Isotopes – Hungarian Academy of Sciences	Budapest	Hungary
Rheinische Friedrich-Wilhelms Universität Bonn	Bonn	Germany
Universität zu Köln	Cologne	Germany
European Commission – Joint Research Centre	Geel	Belgium
Leiden University	Leiden	Netherlands
Technical University Delft	Delft	Netherlands
Central Laboratory of the Research Councils	Didcot	United Kingdom

tribution in acceptable measurement times without performing a full PGAI scan of the sample [Ebe09].

The tasks of the ANCIENT CHARM project were divided into several work-packages which covered (amongst others):

1. Selection of adequate samples for the final *proof-of-concept* measurements,
2. development of procedures for sample preparation and sample transport from one measurement facility to another [Fes08],
3. fabrication of test and benchmark objects for the development and test of the different measurement methods [Kir08],
4. simulations for the design of new measurement setups and hardware [PC07, PC08, PC09a, PC09b],
5. development of PGAA into PGAI/NT and the construction of a new, high-flux PGAI/NT setup at the research reactor FRM 2[2] in Garching near Munich [Bel07, Kud08a],

[2] Forschungs-Neutronenquelle Heinz Maier-Leibnitz, Technische Universität München: http://www.frm2.tum.de/

6. development of NRCA into NRCI/NRT and the construction of a NRCI/NRT setup at the ISIS[3] pulsed neutron and muon source in Didcot, United Kingdom,

7. and the development of methods for the combination and mutual enhancement of the data-sets obtained by the different methods [Sch09, Sch10].

The main involvement of the Institute of Nuclear Physics of the University of Cologne was in tasks 5 and 7 of the list above, but there was also participation in tasks 4 and 6.

[3] ISIS Science and Technology Facilities Council, Rutherford Appleton Laboratory, Oxfordshire: http://www.isis.stfc.ac.uk

2. Neutron methods

2.1. Neutron properties

The free neutron is an unstable particle with a lifetime of 885.7(8) s. Its interesting feature for material analysis is that it is free of charge and can thus, unaffected of the atomic electron-shells, intrude deeply into materials. Neutron beams for material analysis are commonly created in nuclear research reactors or spallation sources.

The wavelength of a free neutron is given by the *de Broglie* equation:

$$\lambda = \frac{\mathrm{h}}{p} = \frac{\mathrm{hc}}{\sqrt{2E_{\mathrm{kin}}\,\mathrm{m_0c}}} \tag{2.1}$$

For neutrons at "room temperature", i.e. $T = 293.16\,\mathrm{K} \Rightarrow E_{\mathrm{kin}} = \mathrm{k}T = 25.26\,\mathrm{meV}$, one obtains the wavelength $\lambda = 0.1797\,\mathrm{nm}$ and the velocity $v_0 = 2198\,\mathrm{m/s}$. Neutrons of this energy are called *thermal neutrons*. For further classification according to the neutron energies, and corresponding temperatures, the neutron energy spectrum is divided loosely into several groups [Mol04, Byr95]: *Slow* or *cold neutrons* with energies below about 100 meV, *epithermal neutrons* with energies in the range of about 0.1 eV – 1 eV, *intermediate neutrons* with about 1 eV – 1 MeV, and *fast neutrons* with energies above 1 MeV.

The important parameter for the description of neutron interaction with materials is the cross-section σ_{total}, which describes the overall probability of a nuclear reaction, i.e. scattering (elastic and inelastic) or capture, of a neutron with the irradiated nucleus:

$$\sigma_{\mathrm{total}} = \sigma_{\mathrm{scattering}} + \sigma_{\mathrm{capture}}. \tag{2.2}$$

The cross-section of neutron capture reactions depends on the kinetic energy of the neutron. As a reference value for each isotope the neutron capture cross-section for thermal neutrons σ_0 is usually tabulated.

The energy dependence of neutron capture cross-sections shows a varying behavior in the different energy regions. Below thermal energy they follow the *1/v-law*:

$$\sigma(v) := \sigma_{\mathrm{capture}}(v) = \frac{v_0}{v} \cdot \sigma_0, \tag{2.3}$$

showing an inverse proportionality to the velocity. Going to higher neutron energies the validity of this law is reduced, as resonances, i.e. energy regions where the cross-section drastically increases in small energy windows, in the capture cross-section value start to appear. Most resonances lie in the range of eV – keV, but some exceptional elements (Cd, Sm, Gd, and Eu) already show resonances in the thermal and epithermal region [Mol04, Mug81, Mug84].

2.2. Neutron Tomography

2.2.1. Mathematical description

Tomography means the process of reconstructing the 2D-distribution of attenuation factors, elemental abundances or other sample properties[1] from 1D-projections of these properties [Cor63, Hou73]. Performing this operation for a set of stacked slices one obtains a 3D-distribution of these properties from their 2D-projections, the so-called radiographies. These radiographies are taken during the rotation of the investigated object[2] around an axis perpendicular to the detection system. For a parallel illuminating beam theoretically a rotation for 180° is enough, however in praxis it may be advisable to do a full 360° rotation of the sample to compensate for deviations from the ideal theoretical assumptions[3].

The principle of tomography is nicely explained in detail in e.g. [Kak88]. The following summary is based on this reference.

Mathematically spoken the process of tomography is the determination of a 2D point function in one plane $\mathrm{f}(x,y)$ from its straight line integral values $\mathrm{P}_\varphi(t)$ [Rad17, Rad86]:

$$\mathrm{P}_\varphi(t) = \int_{\text{line}} \mathrm{f}(x,y)\,\mathrm{d}s. \tag{2.4}$$

In praxis $\mathrm{f}(x,y)$ may be the distribution of neutron attenuation factors $\mu(x,y)$ in one slice while $\mathrm{P}_\varphi(t)$ is a measure for the summed up attenuation factors along one line at angle φ (fig. 2.1), i.e. the gray-value at "pixel" t in one slice of the radiography. Equation (2.4) is called the *Radon transform*. With a parametrization in polar coordinates

$$t = x\cos\varphi + y\sin\varphi, \tag{2.5}$$

we can rewrite (2.4) as

$$\mathrm{P}_\varphi(t) = \int_{-\infty}^{+\infty}\int_{-\infty}^{+\infty} \delta\left(x\cos\varphi + y\sin\varphi - t\right)\mathrm{f}(x,y)\,\mathrm{d}x\mathrm{d}y. \tag{2.6}$$

The key to the tomography problem is the Fourier-slice (or projection-slice) theorem [Bra56]. We take the 1D-Fourier transform of $\mathrm{P}_\varphi(t)$ and the 2D-Fourier transform of $\mathrm{f}(x,y)$:

$$\mathscr{P}_\varphi(\omega) = \int_{-\infty}^{+\infty} \mathrm{P}_\varphi(t)\cdot \mathrm{e}^{-2\pi\mathrm{i}\omega t}\,\mathrm{d}t, \tag{2.7}$$

$$\mathscr{F}(u,v) = \int_{-\infty}^{+\infty}\int_{-\infty}^{+\infty} \mathrm{f}(x,y)\cdot \mathrm{e}^{-2\pi\mathrm{i}(ux+vy)}\mathrm{d}x\,\mathrm{d}y. \tag{2.8}$$

[1] E.g. medical Computer Tomography (CT) maps X-ray attenuation factors in the human body, while medical Magnetic Resonance Imaging/Tomography (MRI/T) usually maps the distribution of hydrogen.

[2] In medical imaging it is common practice to rotate the detection system, not the "sample", i.e. the screened patient. This is equivalent to the rotation of the sample.

[3] E.g. in Neutron Tomography the effect of *beam hardening*, which describes the change of the neutrons energy distribution on their way through the sample, influences the reconstruction results.

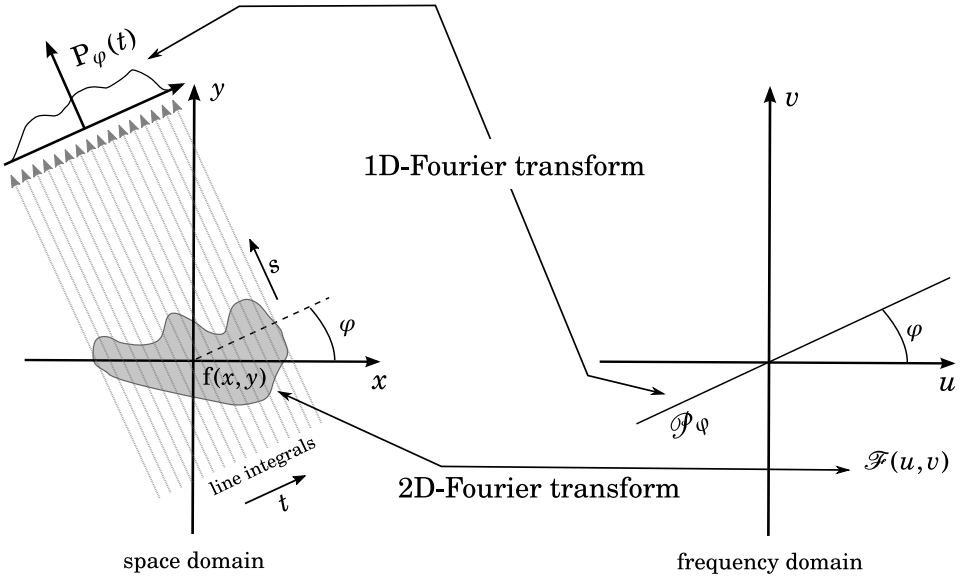

Figure 2.1.: The Fourier-slice theorem [Kak88, Pan83]

Looking at the special case $v = 0$ we obtain from (2.8)

$$\mathcal{F}(u,0) = \int_{-\infty}^{+\infty} \underbrace{\int_{-\infty}^{+\infty} \mathrm{f}(x,y)\,\mathrm{d}y}_{\mathrm{P}_{\varphi=0}(x)} \cdot \mathrm{e}^{-2\pi\mathrm{i}(ux)}\mathrm{d}x, \tag{2.9}$$

and thus, using (2.7) and (2.9)

$$\mathcal{F}(u,0) = \mathcal{P}_{\varphi=0}(u). \tag{2.10}$$

Equation (2.10) is valid for all angles φ, because for a rotated (t,s)-coordinate system

$$\mathcal{P}_{\varphi}(u) = \mathcal{F}(u,v) \tag{2.11}$$

is valid along a line which is rotated by φ with respect to the u-axis (fig. 2.1). Expressing eq. (2.6) in the (t,s)-coordinate system yields

$$\mathrm{P}_{\varphi}(t) = \int_{-\infty}^{+\infty} \mathrm{f}(t,s)\,\mathrm{d}s, \tag{2.12}$$

$$\overset{(2.7)}{\Rightarrow} \qquad \mathcal{P}_{\varphi}(\omega) = \int_{-\infty}^{+\infty}\int_{-\infty}^{+\infty} \mathrm{f}(t,s)\,\mathrm{d}s \cdot \mathrm{e}^{-2\pi\mathrm{i}\omega t}\,\mathrm{d}t. \tag{2.13}$$

For reconstruction purposes it is desired to transform (2.13) to Cartesian coordinates:

$$\mathcal{P}_{\varphi}(\omega) = \int_{-\infty}^{+\infty}\int_{-\infty}^{+\infty} \mathrm{f}(x,y) \cdot \mathrm{e}^{-2\pi\mathrm{i}\omega(x\cos\varphi + y\sin\varphi)}\,\mathrm{d}x\,\mathrm{d}y. \tag{2.14}$$

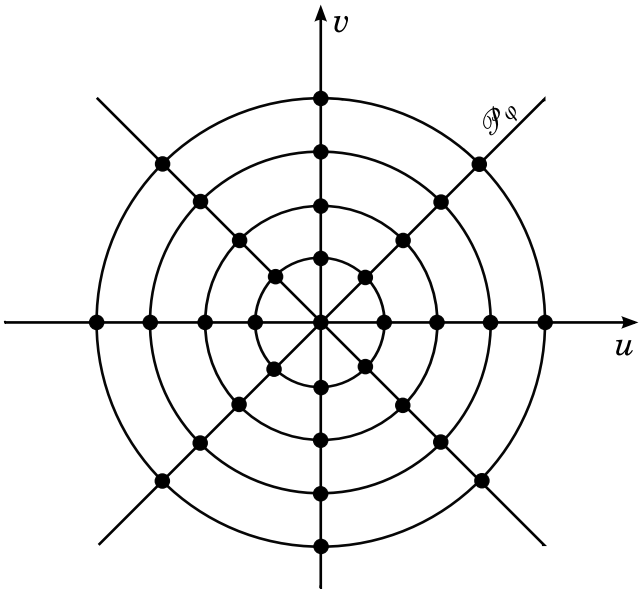

Figure 2.2.: Data point collection in the frequency domain by projections [Kak88, Pan83]

Inversion of the Fourier transform and using (2.11) with $(u,v) = (\omega\cos\varphi, \omega\sin\varphi)$ gives:

$$\mathrm{f}(x,y) = \int_{-\infty}^{+\infty}\int_{-\infty}^{+\infty} \mathscr{F}(u,v)\cdot \mathrm{e}^{-2\pi\mathrm{i}(ux+vy)}\,\mathrm{d}u\,\mathrm{d}v. \tag{2.15}$$

The Fourier-slice theorem can be summarized in words as:

> The 1D-Fourier transform $\mathscr{P}_\varphi(\omega)$ of a parallel projection $\mathrm{P}_\varphi(t)$ at angle φ yields one slice, which subtends an angle φ with the u-axis, in the 2D-Fourier transform $\mathscr{F}(u,v)$ of the projected distribution $\mathrm{f}(x,y)$ [Kak88].

With an infinite number of projections at different angles one could fill up the frequency domain by Fourier transformations of $\mathscr{P}_\varphi(t)$ and then determine $\mathscr{F}(u,v)$. The searched distribution $\mathrm{f}(x,y)$ is then obtained via (2.15).

In reality the number of projections is not infinite and thus the number of known values of $\mathscr{F}(u,v)$ is limited. Because the projections are taken along radial lines, their density increases near to the center of the (u,v)-coordinate system (fig. 2.2). The reconstruction is transferred to a Cartesian (x,y)-grid and due to the varying density of the data-points in the frequency domain they contribute differently to the Cartesian reconstruction cells. Hence the data-points in the frequency domain have to be weighted by their distance to the coordinate origin.

Transforming the right side of (2.15) to polar coordinates (ω,φ) and under exploitation of the symmetry $\mathscr{F}(\omega,\varphi+\pi) = \mathscr{F}(-\omega,\varphi)$ yields

$$\mathrm{f}(x,y) = \int_0^{\pi} \underbrace{\int_{-\infty}^{+\infty} \mathscr{F}(\omega,\varphi)\,|\omega|\cdot \mathrm{e}^{-2\pi\mathrm{i}\omega(x\cos\varphi+y\sin\varphi)}\,\mathrm{d}\omega}_{\mathrm{Q}_\varphi(x\cos\varphi+y\sin\varphi)}\,\mathrm{d}\varphi. \tag{2.16}$$

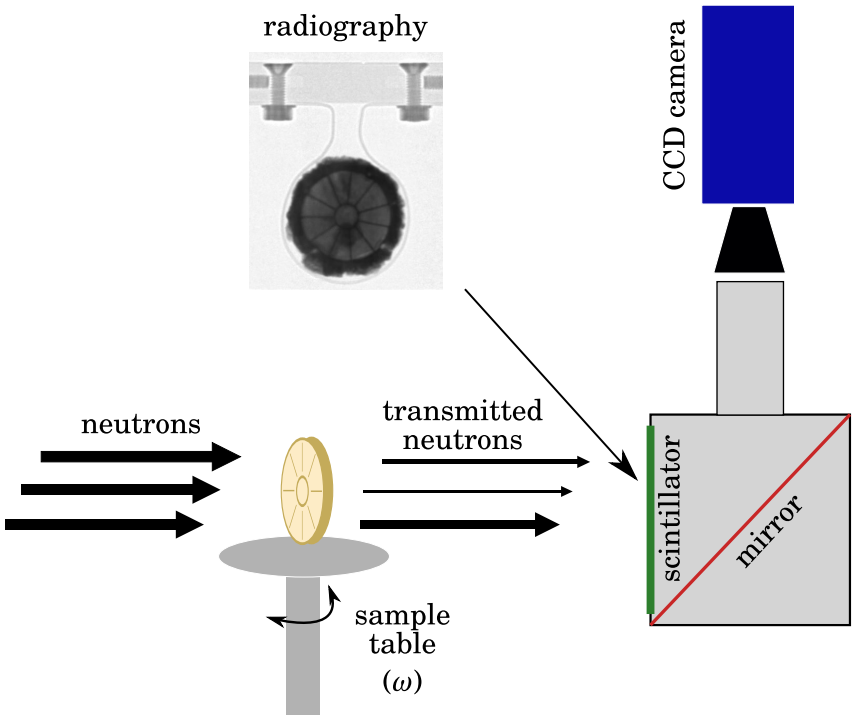

Figure 2.3.: A common Neutron Tomography setup

The term Q_φ is called *filtered projection* with filter $|\omega|$. For practical reasons like e.g. noise filtering it may be advisable to use adjusted filters (e.g. the Shepp-Logan filter [Kak88]). Equation (2.16) is the basis for the *filtered back-projection* algorithm that is commonly used for tomographic reconstructions. Another alternative approach, based on the algebraic analysis of the projections, is introduced in [Bal07]. It is claimed that this algebraic reconstruction procedure performs better for cases when the projection information is incomplete, e.g. only available for a limited angular region.

During this work the software OCTOPUS [Die04], which uses the filtered back-projection algorithm, was used for the tomographic reconstructions.

2.2.2. Cold Neutron Tomography

For cold Neutron Tomography (NT) the reconstructed property is the distribution of neutron attenuation factors inside the investigated object. Modern NT systems, as shown in figure 2.3, acquire the radiographies with CCD[4]-cameras, that collect the image information digitally. The sample is placed on a rotation table into the cold neutron beam. A neutron scintillator, made e.g. from a ZnS:Ag, phosphor, and ^{6}Li com-

[4] **C**harge-**c**oupled **d**evice

pound, is placed behind the sample. This scintillator performs the reaction [Die04]

$$\mathrm{n} + {}^{6}\mathrm{Li} \rightarrow {}^{3}\mathrm{H} + {}^{4}\mathrm{He} + 4.79\,\mathrm{MeV}. \tag{2.17}$$

The ^{3}H and ^{4}He atoms interact with the phosphor in the scintillation layer and create visible light, which is collected by a grayscale CCD-camera. To protect the camera from neutron damages it is positioned outside the neutron beam, normally under an angle of 90°. A silver-free[5] mirror reflects the light into the camera direction.

The theoretical number of projections of the sample one should acquire to obtain an optimal resolution is limited by the Nyquist theorem and results to:

$$\#p = \frac{\pi N}{2}, \tag{2.18}$$

with the number of projections $\#p$ and the number of pixels in one horizontal slice of the detection system N. In [Sch99] it is shown that for realistic resolutions of the commonly used detector systems this number can be further reduced to

$$\#p \approx \frac{N}{2 \ldots 3}, \tag{2.19}$$

without worsening the resulting reconstruction quality.

2.3. Prompt Gamma-ray Activation Analysis

2.3.1. Principle of the method

Prompt Gamma-ray Activation Analysis (PGAA) utilizes characteristic γ-radiation that is emitted after the interaction of a nucleus with low energetic (thermal or cold) neutrons for non-destructive elemental or even isotopic identification and quantification measurements. It is closely related to Neutron Activation Analysis (NAA). PGAA is extensively described in the existing literature, e.g. [Mol04, Alf95, Pau00], thus only a brief summary is given here.

The most important process for PGAA and NAA is the radiative (n,γ)-capture process. After the capture of a low energetic neutron (with an energy of a few meV) an excited compound nucleus is formed with an excitation energy of the neutron binding energy plus the kinetic energy of the neutron:

$$\mathrm{n} + {}^{\mathrm{A}}\mathrm{Z} \rightarrow {}^{\mathrm{A+1}}\mathrm{Z}^{*}. \tag{2.20}$$

The neutron's binding energy is the clearly dominating contribution, having values between about 6 MeV and 11.6 MeV for the known stable isotopes [Mol04]. The excited nucleus then decays with the emission of γ-radiation to its stable ground state, either directly or via energy levels between the excited and the ground state:

$${}^{\mathrm{A+1}}\mathrm{Z}^{*} \rightarrow {}^{\mathrm{A+1}}\mathrm{Z} + \gamma. \tag{2.21}$$

[5] The irradiation of silver with neutrons induces long living activation, which should be avoided.

The intervals between the energy levels in the compound nucleus define the energies of the emitted γ-rays, corrected for the recoil energy of the nucleus:

$$E_\gamma = E_{\text{Transition}} - E_{\text{Recoil}}, \tag{2.22}$$

$$E_{\text{Recoil}} = \frac{E_\gamma^2}{2\,m_{\text{A}}\,c^2}, \tag{2.23}$$

with the mass of the recoiling atom m_{A}. For light elements the recoil energies can be in the order of up to some keV, thus about 3 magnitudes lower than usual transition energies.

The time scale of the decay processes defines the classification of *prompt*, i.e. "immediate" γ-rays. One sensible definition for "promptness" can be given as:

> Gamma-rays are called *prompt*, when their decay times, following the neutron capture reaction, are much shorter than the time resolution of the acquisition system [Mol04].

Typical time resolutions are in the order of nano-seconds, which defines the upper limit for the classification as prompt γ-ray. The definition above clearly separates PGAA from NAA, where one looks at delayed γ-rays following the neutron capture process, emitted by the formed daughter nucleus, usually after a β^--decay. While for NAA the γ-ray spectra acquisition is done offline, i.e. *after* the irradiation of the analyzed sample, PGAA acquisition has to be done online, i.e. *during* the irradiation of the sample by the neutron beam. Of course this leads to a much higher γ-ray background in the PGAA spectra, which worsens the detection efficiency for many elements compared to NAA. Taking into account that for PGAA the γ-detector is usually placed farther away from the sample to avoid neutron damages, while for NAA the sample may be placed directly in front of the detector after sample activation (when the decay times of the investigated elements are long enough), the detection efficiency may be higher by a factor 50 or more for NAA [Sze08a]. Of course this is dependent on the investigated elements.

On the other hand PGAA is superior over NAA e.g. for some important light elements as H, B, N, Si, P, S, and Cl and some heavy elements as Cd, Gd, Sm and Hg [Yon96, Bae03, Fre08] which are difficult, or even impossible, to detect with NAA. It thus can be seen as a complementary method to NAA. Another advantage of PGAA over NAA is the faster availability of the measurement results and the usually shorter irradiation times necessary.

For imaging purposes (see chapter 2.4), where multiple measurements have to be performed on the same object at different positions and/or under different measurement angles, the focus of PGAA on "immediately" decayed energy levels has the indispensable advantage that subsequent measurements are not influenced by previous irradiations, at least as long as the prompt gamma-ray peaks do not interfere with longer living decay peaks.

2.3.2. Quantitative PGAA

PGAA is a quantitative method, i.e. it can deliver concentrations of elements in the investigated samples. However it is very difficult to obtain absolute values for the elemental masses inside a sample, due to factors like e.g. variations in the neutron flux over time, thus normally only a relative quantification is done. The elemental abundances are given relative to an internal standard element, that is present in the analyzed sample. One possible method for the quantification of elmental abundances is the *k_0-method* [Mol98, Pau95, Bae03, Lin03], which is originally coming from NAA [Sim75, Cor89].

The area of a peak at energy E_γ origination from the (n,γ)-reactions on element χ inside a sample volume V is given by [Mol98]:

$$\mathcal{N}_{\gamma,\chi}\left(E_\gamma\right) = \frac{\mathrm{N_A}\Theta_\chi I_{\gamma,\chi}}{\mathrm{M}_\chi} \cdot \int_V \int_{E_\mathrm{n}=0}^{\infty} \int_{t=0}^{\tau} \rho_\chi(V)\, \sigma_\chi(E_\mathrm{n})\, \Phi(E_\mathrm{n},t,V)\, \epsilon\left(E_\gamma,V\right) \mathrm{d}t\, \mathrm{d}E_\mathrm{n} \mathrm{d}V, \tag{2.24}$$

with the density $\rho_\chi(V) = \frac{\mathrm{d}m_\chi(V)}{\mathrm{d}V}$ of the elemental mass $\mathrm{d}m_\chi$ in volume $\mathrm{d}V$, the Avogadro number $\mathrm{N_A}$, the isotopic abundance Θ_χ of the element's isotope that emits the selected γ-rays, the relative intensity of the investigated γ-line I_γ, the atomic mass of the element M_χ, the (n,γ)-cross-section σ_χ, the neutron flux distribution ϕ at the selected volume, the overall detection efficiency ϵ of a γ-ray emitted in the selected volume and the acquisition time τ. For *small*, *homogeneous* samples and *constant shape* of the neutron flux distribution we can write [Gen00]:

$$\int_V \epsilon\left(E_\gamma,V\right) \mathrm{d}V = \epsilon\left(E_\gamma\right) \cdot \mathrm{f}(V), \tag{2.25}$$

$$\int_v \rho_\chi(V)\, \mathrm{d}V = m_\chi, \tag{2.26}$$

$$\phi(E_\mathrm{n},t,V) = \varphi(E_\mathrm{n},V) \cdot \mathrm{g}(t). \tag{2.27}$$

For the cold neutron region eq. (2.3) can be applied and we obtain for the peak ratios of element χ to the internal monitor element μ:

$$\frac{\mathcal{N}_{\gamma,\chi}\left(E_{\gamma,\chi}\right)}{\mathcal{N}_{\gamma,\mu}\left(E_{\gamma,\mu}\right)} = \frac{m_\chi \Theta_\chi I_{\gamma,\chi} \epsilon\left(E_{\gamma,\chi}\right) \sigma_{0,\chi}/\mathrm{M}_\chi}{m_\mu \Theta_\mu I_{\gamma,\mu} \epsilon\left(E_{\gamma,\mu}\right) \sigma_{0,\mu}/\mathrm{M}_\mu}. \tag{2.28}$$

The k_0-ratio of the elements χ and μ is then defined as:

$$k_{0,(\chi,\mu)} = \frac{\mathcal{N}_{\gamma,\chi}\left(E_{\gamma,\chi}\right)/m_\chi \epsilon\left(E_{\gamma,\chi}\right)}{\mathcal{N}_{\gamma,\mu}\left(E_{\gamma,\mu}\right)/m_\mu \epsilon\left(E_{\gamma,\mu}\right)} = \frac{\Theta_\chi I_{\gamma,\chi} \sigma_{0,\chi}/\mathrm{M}_\chi}{\Theta_\mu I_{\gamma,\mu} \sigma_{0,\mu}/\mathrm{M}_\mu}. \tag{2.29}$$

For the mass ratios of elements χ and μ one finally obtains:

$$\frac{m_\chi}{m_\mu} = \frac{1}{k_{0,(\chi,\mu)}} \cdot \frac{\mathcal{N}_{\gamma,\chi}\left(E_{\gamma,\chi}\right)/\epsilon\left(E_{\gamma,\chi}\right)}{\mathcal{N}_{\gamma,\mu}\left(E_{\gamma,\mu}\right)/\epsilon\left(E_{\gamma,\mu}\right)}. \tag{2.30}$$

The k_0-values for all isotopes are usually tabulated normalized to selected comparator isotopes, e.g. hydrogen [IAE07].

2.4. Prompt Gamma-ray Activation Imaging

2.4.1. Principle of the method

Conventional PGAA is a bulk method, i.e. it delivers no information about the spatial distribution of the elements inside the sample. One direct method to obtain the spatial elemental distribution is Prompt Gamma-ray Activation Imaging (PGAI). Through collimation or focussing of the neutron beam to a diameter of just few millimeter one limits the active measurement region to a small chord through the sample [Bae01]. This is called the PGAI *chord configuration* (fig. 2.4(a)). The sample is then placed on a moving table that is able to position it in (at least) two dimensions in front of the collimated neutron beam, thus allowing a two dimensional scan of the whole sample or only some positions of interest. The analysis of the spectra obtained at the different positions then delivers a 2D elemental map of the investigated object.

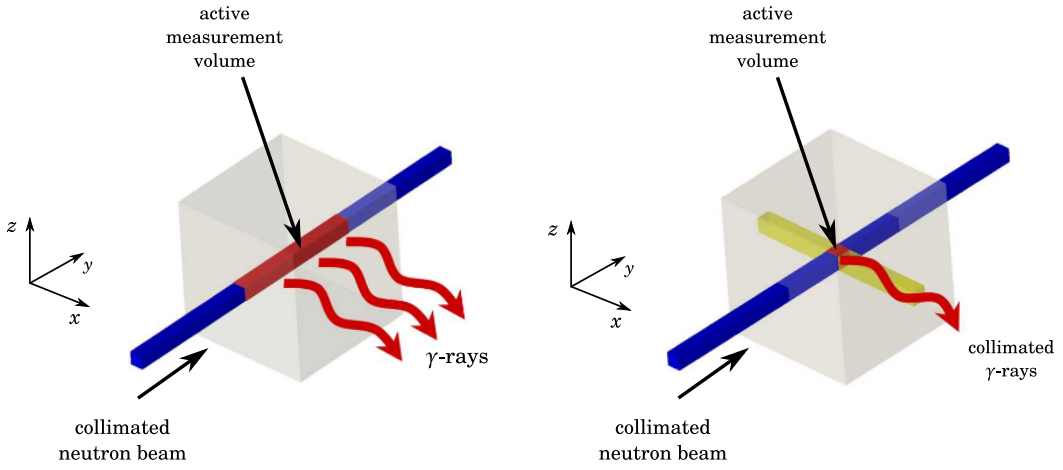

(a) chord configuration (b) isovolume configuration

Figure 2.4.: PGAI measurement configurations (after [Kis08])

For three-dimensional elemental mapping the above procedure can be further extended by a γ-ray detector collimation of a few square millimeter [Kas06a, Kas06b, Kis08]. The intersection of the neutron beam with the solid angle of the collimated γ-ray detector then defines the spatially fixed, active measurement volume, the so-called *isovolume* (fig. 2.4(b)). Again scanning of the sample is performed, but through the γ-collimation one now obtains the depth information about the elemental composition along the neutron beam, which leads to a 3D elemental map of the object. Clearly, a table which supports movements in at least (x,y,z)-directions is needed as sample support, now. Anyhow it is advisable to use a sample support that allows rotation of the sample with respect to the beam, to be able to optimize the beam path through the sample, e.g. to minimize self-shielding effects.

The physical dimensions of the isovolume limit the maximal achievable spatial resolution for the elemental mapping, hence it is desirable to make this volume as small

as possible. Of course the size of the isovolume directly influences the number of nuclear (n,γ)-reactions that can be detected and consequently the size of the isovolume should be chosen large enough to generate a "sufficient" number of γ-events per time-interval in the detector, to keep the necessary measurement time acceptably short. The choice of the isovolume dimensions is a compromise and has to be selected with regard to other parameters, like available neutron flux, detector efficiency, magnitude of γ-ray background, and the cross-sections of the expected elements of interest.

2.4.2. PGAI as a surface method

The idea of PGAI as surface method is to use the 2D-PGAI chord-configuration with a thin chord neutron beam and open γ-detector and to illuminate only a thin layer on the surface of the sample. With the help of neutron radiographies it is possible to align the sample in such a way that only a few hundred micrometer of the surface are illuminated (fig. 2.5). Care must be taken that only the desired sample position of the surface is illuminated by the neutron beam, because the unintended irradiation of other positions would give wrong additions to the collected spectra.

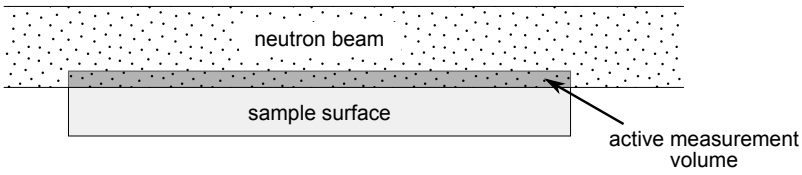

Figure 2.5.: Principle of surface PGAI measurements

The advantage of using neutrons for the investigation of a small surface layer is again the bigger penetration depth of neutrons compared to e.g. protons. With an accurate sample-positioning it is possible to investigate thin layers of a few hundred micrometer, which is much deeper than what can be reached with e.g. PIXE, which can only be used for depths of some tens of micrometer [Kud05a]. For adequate geometries it is even possible to create a qualitative depth profile of the elemental densities at the sample surface. This can be interesting for the investigation of e.g. gilding layers on cultural heritage objects.

One problem of PGAI as surface method is that it requires a free *line-of-sight* along the analyzed surface, which is not given for all geometries, e.g. it is not possible to investigate positions in small valleys or channels on the sample. Another drawback is the time-consuming sample positioning (see chapter 4.3) and the need for a neutron radiograph.

Very first experiments with this PGAI configuration were conducted for this work and are described in chapter 4.3.

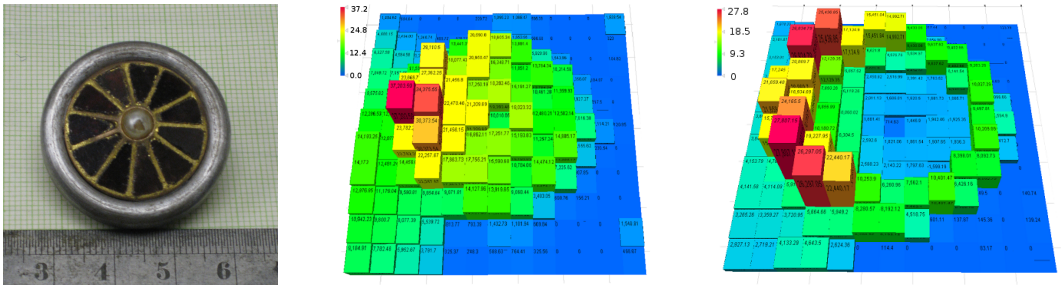

(a) Fibula replica (b) Copper intensities (c) Iron intensities

Figure 2.6.: Uncorrected elemental concentrations for copper and iron measured with a 2D-PGAI scan of the fibula replica (a). The γ-detector was positioned on the left side of the replica. ((b) and (c) courtesy of the Department of Nuclear Research, Institute of Isotopes, Hungarian Academy of Sciences, Budapest)

2.4.3. Quantitative PGAI

For the quantitative determination of elemental ratios with PGAI equation (2.24) that describes the peak areas generated from a small sample volume is valid in principle, but in contrast to the considerations in chapter 2.3.2 the k_0-method cannot be applied without corrections. Equation (2.30) was deduced for small, homogeneous samples. Obviously the approximation of a "homogeneous" sample makes no sense for an imaging method.

The problematic parameters for an elemental quantification are the neutron flux $\Phi_\chi(E_\mathrm{n}, V)$ at the isovolume position and the overall γ-ray detection efficiency $\epsilon\left(E_\gamma, V\right)$.

In principle the distribution of the neutron flux Φ can be determined quite precisely by measuring the flux quantity at isovolume position, e.g. via gold activation measurements, and applying the known neutron flux distributions $\Phi(E_\mathrm{n})$ for the appropriate neutron production process [Mol04]. If we assume that the neutron flux does not fluctuate too much over time one then has a value for $\Phi(E_\mathrm{n}, V_\mathrm{iso.})$ *without* sample in the neutron beam. Unfortunately the sample material itself will disturb the neutron flux distribution (neutron self-shielding). This disturbance is dependent on the spatial distribution of the elements inside the sample and their concentrations, and thus exactly on the properties one wants to obtain.

Similar considerations are true for $\epsilon\left(E_\gamma, V_\mathrm{iso.}\right)$. For the determination of the overall efficiency one has to respect the amount of γ-rays that are absorbed on their way from the isovolume to the detector (γ-ray self-absorption). This figure is dependent on E_γ and again the elemental concentrations on the path from isovolume to sample surface and can have a not negligible effect. This effect has been investigated with 2D-PGAI measurements on the replica of an ancient fibula [Sze08b, Bel08c]. In figure 2.6 the uncorrected copper and iron intensities that were measured over a grid covering the whole object are shown. One clearly sees that the intensities on the side far away from the detector are significantly smaller, than on the closer side, although, due to the known manufacturing process, they are expected to be of the same magnitude.

The mentioned factors hamper the quantitative analysis of PGAI data significantly. In chapter 4.2 an idea will be presented how to correct for the neutron self-shielding effect with the help of a NT reconstruction. For γ-ray self-absorption correction it has been suggested to apply some Monte-Carlo simulations recursively to the measured PGAI data to reconstruct the elemental concentrations in multiple iterations [Sze08b]. For elements which emit γ-rays over a wide energy range one may make use of the energy dependency of the absorption process to create a calibration function for self-attenuation correction [Pau95].

To sum up it has to be said that the problems for a true quantitative PGAI analysis are still unsolved, although some promising progress has been made (chapter 4.2).

2.5. Combined PGAI and NT

As indicated above, the high collimation of the neutron beam and, in case of isovolume measurements, the collimation of the γ-detector cause a much lower event-rate for PGAI measurements compared to standard PGAA and thus much longer measurement times. For a full mapping of the object the needed measurement time per position has to be multiplied by the number of positions necessary for a full scan, hence significantly increasing the needed experiment time. E.g. to perform a full scan of a small cube of $(10 \times 10 \times 10)$ mm^3 with an ideal isovolume size of $(2 \times 2 \times 2)$ mm^3 one has to measure $(5 \times 5 \times 5 = 125)$ positions. If we assume a necessary acquisition time of about 45 min per position the overall measurement time would be almost 4 days for this small object. For larger objects the required measurement time may become unrealistically long, e.g. for a cube of 20 mm edge lengths one would have to measure about one month for a full map with the above mentioned properties. Such a long measurement time is in most cases infeasible for several reasons:

- Experiment time at a PGAA/PGAI setup is often rare and valuable.
- The sample may not be available for very long measurements, e.g. objects of cultural heritage interest may be part of a permanent exhibition, where they can only be removed for relatively short times.
- Long irradiation times may cause activation of the sample. Depending on the activated isotopes the sample then has to stay at the measurement facility for a, possibly very long, decay period.

Although high, long-lasting activation of the sample is not so likely for PGAI measurements as it is for bulk PGAA, because always only a relatively small part of the sample is irradiated by neutrons, it still is the most severe argument for keeping the measurement times as short as necessary.

For many objects of interest it may be sufficient to measure just a few positions of interest instead of performing a full PGAI scan, e.g. objects of cultural heritage interest are often manufactured from many different parts, but each part for itself can often be assumed to be of nearly homogeneous composition. For the selection of these

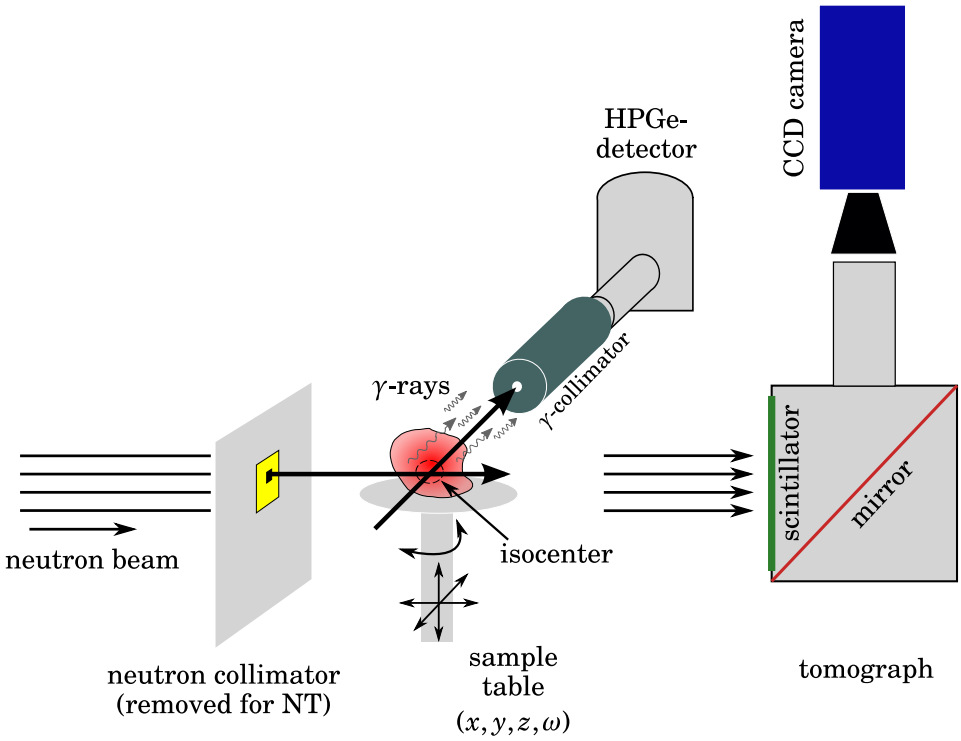

Figure 2.7.: Combined PGAI/NT setup

interesting positions the NT method may be utilized [Kas06b]. Because PGAI and NT both use a beam with low energetic neutrons these two methods may be operated at the same neutron beam guide in combination: NT for the initial acquisition of a 3D morphological model of the sample and the selection of interesting measurement positions, and PGAI for the determination of the elemental composition at this positions. NT can even assist in the final positioning of the sample for PGAI. This combined utilization of these two methods is called PGAI/NT [Bel08a, Bel08b, Sze08b].

In [Ebe09] a method is shown that utilizes NT to extend the elemental distribution, measured through a 2D-chord-PGAI for few distinct positions, to the complete object. The idea is that adjacent regions that show the same neutron absorption properties in the NT reconstruction are probably made from the same material. E.g. it is likely that a filling material that can be located in the NT reconstruction is quite homogeneous all over the filled cavity, when it shows homogeneous neutron absorption properties. Of course this method is not completely accurate. Inhomogeneities that are not visible via NT will falsify the elemental distribution. Another reason for possible mistakes in the elemental 3D assignment may be the use of the chord geometry. Because one always measures along a full line through the object, some parts of the objects, e.g. a back-plate, may always be visible in the γ-ray spectra and thus lead to wrong assumptions. This effect may be minimized by a cleverly chosen set of measurement positions and illumination angles of the sample in some cases, but not

in general.

The design of a combined PGAI/NT setup is shown in figure 2.7. The sample is placed on a table that is movable in (x, y, z, ω)-directions. For PGAI measurements a HPGe[6]-γ-detector is placed at an angle of 90° relative to the neutron beam. A γ-collimator, normally made out of lead, is narrowing the detector's field-of-view and defining the location of the isovolume in depth. Under the chosen angular orientation the number of scattered neutrons that hit and damage the detector is minimized. Another reason for this detector position is that in this way a regular, non-distorted isovolume can be defined together with the collimated neutron beam. A neutron collimator, e.g. fabricated out of ^{6}Li-enriched polymer, confines the neutron beam to a few millimeter diameter. For NT measurements the neutron collimator is removed to get a wide, open beam. The tomograph is located behind the sample table and should be positioned as close as possible to the sample, to minimize blurring effects.

[6] **H**igh-**P**urity-**Ge**rmanium

3. Instrumentation

3.1. PGAA setup at FRM 2

The experiments were performed at the new PGAA setup at the *Forschungsneutronenquelle Heinz Maier-Leibnitz* (FRM 2) in Garching near Munich [Kud08a, Kud05b, Kud05a]. The setup is located at the end of a 51 m long cold neutron guide that is aiming at the cold source of the FRM 2 reactor core. A remarkable feature of the PGAA neutron guide is that its last 5.8 m are elliptically tapered, to focus the neutron beam and increase the available cold neutron flux. The guide can be extended by an elliptically tapered removable "nose" of 1.1 m length, which focuses the beam even more and thus gives an even higher neutron flux, for the price of a smaller useable area and increased beam divergency. The available parameters of the neutron beam configurations are listed in table 3.1. The listed neutron fluxes are adjustable by the use of three beam attenuators that may reduce the maximal flux for e.g. better background conditions or radiation protection reasons, if necessary.

Two Compton-suppressed HPGe-detectors are positioned under angles of 90° relative to the beam (fig. 3.1): Detector 1 with a relative efficiency of 36 % in perpendicular geometry and detector 2 with a relative efficiency of 60 % in coaxial geometry. For PGAA or 2D-PGAI measurements their *field-of-view* is limited by γ-collimators of 10 mm diameter for detector 1 and a conical collimator which increases from 20 mm diameter at the sample side to 43 mm at the detector side for detector 2 to reduce the background in the γ-ray spectra. A stepper-motor driven "target ladder" is located inside an evacuated sample chamber, which allows the measurement of six different samples without the need to open the evacuated chamber.

For the acquisition of the γ-ray spectra a new automatic data-acquisition system has been developed during this work, which allows the consecutive measurement of all samples positioned in the vacuum chamber, with separately configurable beam properties and acquisition times, without the need for manual intervention. This system is described in chapter 3.4.3.

3.2. PGAI/NT setup at FRM 2

3.2.1. Modifications to the PGAA setup

For PGAI/NT measurements the configuration of the PGAA setup was changed:

- The γ-collimator of detector 2 was exchanged by a lead collimator with significantly smaller aperture (ch. 3.2.3).

Table 3.1.: Beam parameters of the PGAA setup at FRM 2 [Kud08a, Can09, Can10]

Beam parameter	
mean neutron spectrum energy	1.83 meV
mean neutron wavelength	6.7 Å
thermal equivalent neutron flux	$2.42 \cdot 10^{10}$ n/cm^2 (no nose) $\sim 5.5 \cdot 10^{10}$ n/cm^{2*} (with nose)
usable beam size ($w \times h$)	(14×38) mm (no nose) (4×10) mm (with nose)

* Expected. Actual value currently under analysis (see [Can10]).

- The PGAA "sample ladder" and the vacuum chamber were removed to make space for the (x, y, z, ω)-positioning table.
- A newly constructed CCD tomograph was placed behind the sample position for NT.
- For NT measurements the neutron flight path was prolonged by a 160 cm long, boron-shielded flight tube, to obtain a more parallel neutron beam at sample position. To improve the beam quality even further it proved to be effective to insert two boron collimator windows of about 3×5 cm^2 into this flight tube to "cut" away the most divergent neutrons.
- For PGAI measurements an adjustable neutron collimator was placed into the neutron beam (ch. 3.2.4).

During the measurement presented in this work the elliptical "nose" at the exit of the beam guide was not used despite the higher neutron fluxes it should deliver. The resulting beam with "nose" proved to be very divergent, which extremely influences the isovolume shape. Hence, these first measurements at the new PGAI/NT setup were performed with lower flux but a better defined isovolume.

The setup in PGAI/NT configuration and the layout of the measurement chamber are shown in figure 3.2. The features of the NT part of the configuration are extensively described in [Ebe09]. The properties of the PGAI part are investigated here.

3.2.2. Alignment of the PGAI/NT setup

Necessity of a proper alignment

For an accurate position-sensitive imaging measurement a thorough alignment of the measurement setup is indispensable. For PGAI measurements the alignment of the neutron and γ-collimator is the most crucial part. If the γ-collimator's field-of-view does not cross the collimated neutron pencil beam, one will not be able to measure anything or, if the alignment is not optimal, only with limited count-rates. That

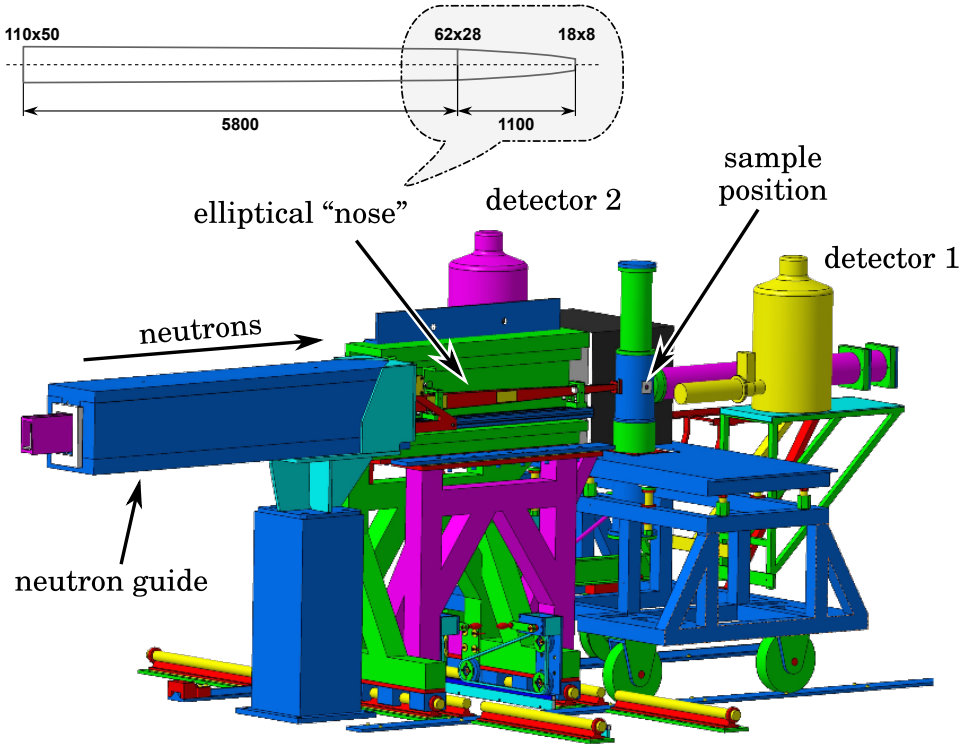

Figure 3.1.: Cut through the PGAA setup at FRM 2

means one has to align two about 2–3 mm wide lines in a three-dimensional space of about $(30 \times 30 \times 30)$ cm^3 to create an isovolume. In addition one has to determine the coordinates of this isovolume in units of motor steps of the (x, y, z, ω)-moving table for correct sample positioning.

The following procedure for the alignment of a PGAI/NT setup has been produced from experiences and procedures developed at the Institutes of Isotopes of the Hungarian Academy of Sciences in Budapest, where first tests of the new PGAI method were carried out [Bel08a, Bel08b, Sze08b], and extended by the experiences gained at the PGAI/NT setup at FRM 2.

Alignment procedure

The fixed axis for the alignment of the other equipment is the prolongation of the neutron beam guide, which defines the flight path of the incoming neutrons. All other equipment must be aligned to this line. The PGAI detector with the small γ-collimator is placed under a 90° angle with respect to the neutron beam. Because the detector should be heavily shielded by lead bricks, its position can be seen as “quasi”-fixed. A fine adjustment of the γ-collimator may not be possible, at least for the PGAI setup at FRM 2, when the massive lead shielding is once in place. Thus, one has to align the collimated neutron beam to hit the prolongation of the γ-collimator, during the

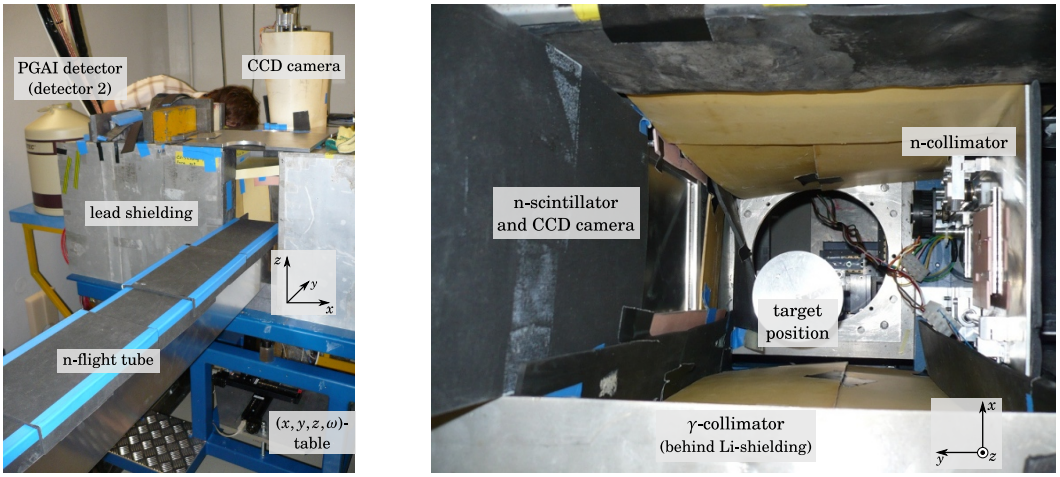

(a) Setup in NT configuration

(b) PGAI/NT measurement chamber

Figure 3.2.: Setup in PGAI/NT configuration

alignment procedure. Taking these two lines as fixed the further alignment of the setup can be approached as follows:

Positioning of the neutron tomograph The neutron tomograph is an invaluable tool for the further procedure, thus one should position it in the beginning. Its exact positioning is not so important, but one should take care that it is positioned quite perpendicular to the beam to avoid distortions in the radiographies, that it is close to the expected sample positions to avoid blurring in the radiographies, and that it covers the full expected sample area. It is helpful if the tomograph is fixed with respect to the setup, because one may then compare absolute pixel-positions in the radiographies for different sample positioning processes.

Alignment of the moving table The (x, y, z)-axes of the moving table are normally designed to be perpendicular to each other, thus the accuracy of their orientation towards each other is defined by the quality of the moving table and cannot be influenced. Normally this accuracy should be sufficiently high. One axis of the table, in our case called y-axis, has now to be aligned to follow the neutron beam line. In lucky cases this line may be marked on the setup, which eases the process. Without such help one has to find other means to roughly align the table to this line.

For the fine alignment of the table orientation one may then use the open neutron beam and the tomography system, by placing a thin calibration object on the table. When this object is moved along the beam line, its position on the tomograph's scintillator should not change (or only very little). If the radiography image of the object moves during this process, the table's y-axis has to

be adjusted. This steps should be repeated until the orientation of the table is satisfying.

Adjustment of the table's rotation (ω)-axis The rotational orientation of the moving table should be aligned in such a way that the sample support is orientated perpendicular to the beam for an angle of 0°, giving a defined sample orientation. Good moving tables may have reference switches, defining fixed position for the stepper motors. If this reference position for the rotational axis is in a known orientation to the (x, y)-axes probably no further alignment is necessary. If this is not the case one may use again the neutron tomograph for alignment. By placing a long, flat calibration object in a defined orientation on the moving table, the angle 0°, i.e. parallel orientation of the object with respect to the beam, is reached when the thickness of the object's projection on the neutron tomograph's scintillator is minimal. This defines the fixed reference position of the ω-axis.

Determination of the γ-collimator's (y,z)-position A time consuming and tricky task is the exact localization of the γ-collimator's position in terms of motor steps. This process should be done in two steps: A coarse and a fine positioning of the moving table. As first step an intense γ-source of minimal, point-like size is positioned in the center of rotation of the moving table. For a safer support it is advisable to fix the source on a larger object of known dimensions. Finally the γ-collimator position then has to be corrected for the height of this supporting object.

For the coarse positioning the most effective and fastest method showed also to be the easiest: The γ-collimator is extended by sticking e.g. a long, straight wire into it, thus prolonging its *line-of-view*. The wire should be long enough to reach the middle of the measurement chamber. Afterwards the γ-source is moved with the moving table in y- and z-directions to the position of the wire. As result the source should now be quite near to the desired position in front of the γ-collimator. Other methods, utilizing a precise alignment of a laser that is placed at the detector position and aims through the γ-collimator into the measurement chamber, proved to be not as effective, because the laser beam gets reflected at the lead walls of the collimator. This produces reflection patterns inside the measurement chamber, which are hard to distinguish from an unreflected laser spot.

For the fine positioning one now performs a scan around the coarsely determined isovolume position and measures the count-rates produced by the γ-source. The position with the highest intensity rates identifies the motor positions of the isovolume in y- and z-direction.

Positioning of the neutron collimator As a final step the neutron collimator has to be positioned in that way, that the collimated neutron beam hits the previously determined y- and z-position of the isovolume. The x-coordinate can be

freely chosen with respect to other constrains like available space or practical positioning considerations. Anyhow, it is advisable to locate it quite close to the γ-detector, to gain higher count-rates and a better spatial resolution for the measurements. On the other hand an isovolume very close to the γ-detector may hinder the sample positioning, due to geometrical reasons. Another important aspect is the inhomogeneity of the neutron beam intensity. It is advisable to select a neutron collimator position with a high neutron flux, which can be determined with the help of the neutron tomograph. For an easier positing of the neutron collimator in the (important) z-direction a movable collimator, as introduced in chapter 3.2.4, proved to be useful.

Again the neutron tomography system is used for n-collimator positioning. One now puts a sharp, well defined calibration object, e.g. a small gadolinium dot on the tip of a metal cone, on the moving table and moves it into the previously measured γ-collimator position $(y_{\text{iso}}, z_{\text{iso}})$. With the help of the neutron tomograph the neutron collimator is now adjusted in height, until the small calibration object is visible in its center. Now γ- and neutron collimator form the desired isovolume.

General advice

The alignment process can be quite time consuming, but fortunately it only has to be done once, as long as the moving table does not "forget" its current positions, e.g. due to a power failure or due to lost motor steps. Precautions for such a case should be taken to avoid unnecessary work. As mentioned above good moving tables may provide reference switches for a recalibration of the position values. Even better tables may have internal batteries that keep track of the current motor positions during a power failure. Encoders that count the actual motor steps eliminate the risk of lost steps. If these handy features are not available, one has to improvise, by defining special, easy reproducible positions on each table axis, and use these positions as origin for the alignment.

3.2.3. Design and properties of the γ-collimator

Design

The first γ-collimator was fabricated after a design suggested in [PC07], where Monte-Carlo-simulations about the expected spatial resolutions with a 15 cm long lead collimator were made. That collimator featured a circular entry window of 2 mm diameter, which was enlarged to 3 mm diameter for the last 5 cm. The result of the simulations was an expected spatial resolution of about 3.8 mm for photons in the range of 1000 keV–5000 keV. The spatial resolution is depending on the energy of the photons, because higher energetic γ-rays can penetrate deeper into the shielding material and thus have a bigger likelihood of reaching the detector. Measurements at the PGAA setup at the Budapest Research Reactor showed a spatial resolution of about 4 mm – 6 mm for a square γ-collimator of (2×2) mm^2 [Bel07].

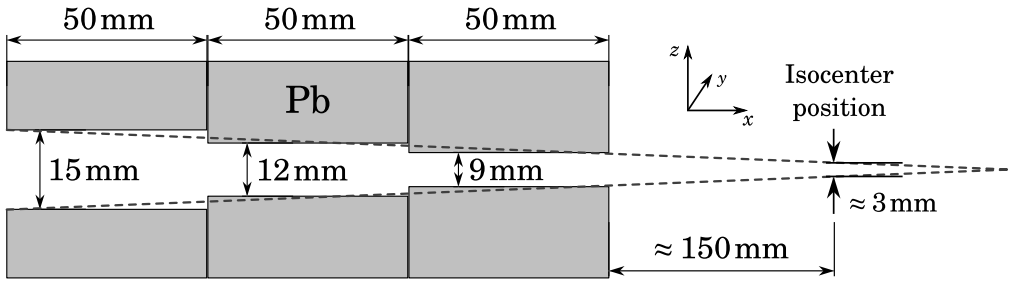

(a) Cut through side

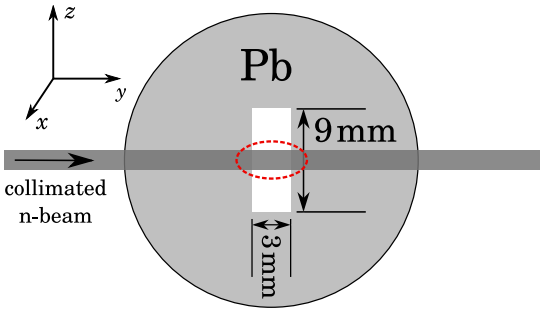

(b) Front view with marked position of the isovolume.

Figure 3.3.: Sketch of the γ-collimator (not in scale), fabricated from three distinct lead pieces.

During the first test measurements at the PGAI/NT setup at FRM 2 it turned out that the γ-count-rates with an collimator-aperture of only 2 mm diameter were too low for really effective measurements. Thus, the aperture was enlarged over the full length to 3 mm. To increase the count-rates even further, the height of the collimator window was enlarged in 3 steps, to 9 mm for the first 5 cm, 12 mm in the next 5 cm, and 15 mm for the last 5 cm interval. These increasing sections should mimic a triangular shape, which was not realized due to practical manufacturing reasons. The dimensions were chosen to maximize the number of passing γ-rays, which are emitted radially from the isovolume, for an isovolume height of up to ≈ 3 mm (fig. 3.3(a)), while still blocking as much as possible from the γ-ray background. Viewed from the front side the γ-collimator has a rectangular shape, if we neglect minor deviations in the corners due to the drilling process used to produce the collimator.

As a reminder: The extended height should not decrease the measurement resolution in the z-axis direction, because only the volume irradiated by the confined neutron beam is emitting γ-rays (if we neglect neutron scattering effects inside the sample; see chapter 3.2.4). The relevant parameter for the space resolution in z- (and x)-direction is the size of the collimated neutron beam at isovolume position. The γ-collimator just confines the depth of the isovolume, i.e. the y-direction (fig. 3.3(b)).

Measurement of the γ-collimator-resolution

To measure the spatial resolution and the intensity profile of the γ-collimator, a ^{152}Eu calibration source was moved along the y- and z- axis in front of the collimator at a distance of about 10 cm. A rectangular area of $(\Delta y \times \Delta z) = (8 \times 18)$ mm^2, covering the upper half of the collimator's slit, was scanned in 9 measurement steps in intervals of 1 mm in y-direction and 10 steps of 2 mm in z-direction. The peaks of five strong lines of ^{152}Eu, covering the energy region from 121.78 keV to 1408.01 keV have been analyzed at each position. The resulting peak areas have been normalized for each energy and plotted in a 9×20 grid in figure 3.5. One can clearly see from the plots that the effective area of the γ-collimator is increasing for higher γ-ray energies.

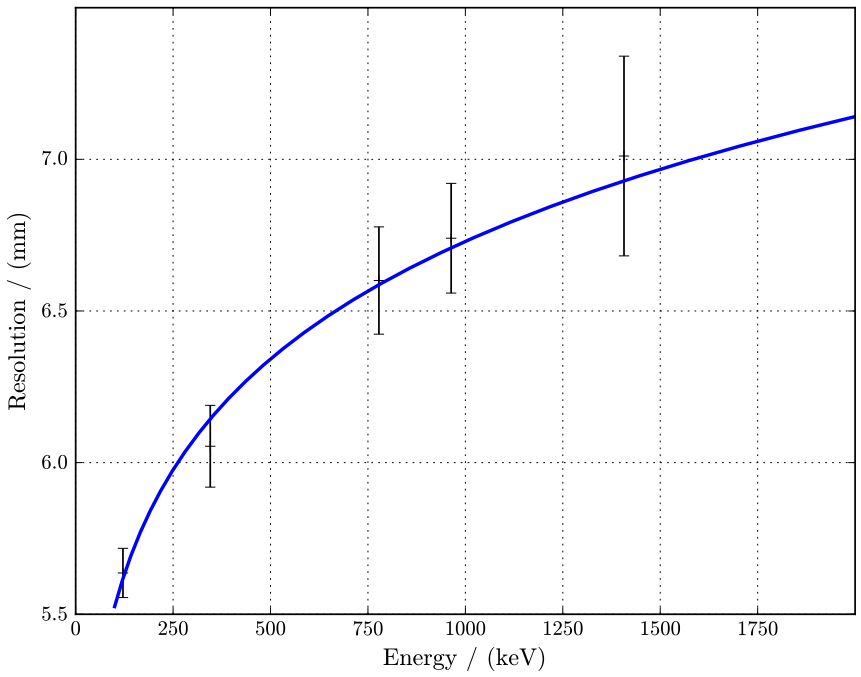

Figure 3.4.: Resolution of the γ-collimator in dependence of the γ-ray energy, measured with a ^{152}Eu calibration source

The lowest line of the scanned grid was positioned to be at the height of the isocenter for the measurement, so the intensities at this line have been taken for the resolution fit. For the measured intensities along this line we expect the following behavior:

- Far away from the collimator the intensity should be vanishing.
- Approaching the collimator aperture the intensities should start to increase. Ideally one would like to have a sudden intensity jump from "0" to "1", when the sample crosses the border of the collimator's slit.

- When the sample is directly in front of the slit the intensity should be maximal at a relatively constant value, forming a plateau, until it vanishes again.

These properties showed to be quite well fulfilled by the empirical function[1]:

$$I(x) = \frac{a}{1+\exp\left(-2k_1 \cdot \left(x - x_0 + \frac{\sigma}{2}\right)\right)} - \frac{a}{1+\exp\left(-2k_2 \cdot \left(x - x_0 - \frac{\sigma}{2}\right)\right)}, \tag{3.1}$$

with the center position x_0, amplitude a and the slope parameters $k_{1,2}$ ($k_1 = k_2$ for a symmetric shape around x_0; see chapter A.3 for details). As a sensible measure for the spatial resolution usually the *full width at half maximum* (FWHM) of the response function is taken. For function 3.1 the FWHM is difficult to determine exactly by analytical means, but we can see from the considerations explicitly shown in chapter A.3 that for a value of $k \cdot \sigma \gtrsim 3$ the parameter σ is a very good approximation for the FWHM.

The resulting fits of eq. (3.1) to the measured intensities are shown in figure 3.5. It can be seen that the resolution grows from ≈ 5.6 mm to ≈ 7 mm in the investigated energy range (fig. 3.4). Compared with the above-mentioned values from [Bel07], which show a resolution of $\approx 4\,\text{mm} - 6\,\text{mm}$ for a (2×2) mm^2 collimator the resolution is quite good, if one remembers that our collimator is 50 % wider. However, as we will see, this is much worse than the spatial resolution in the x- and z-directions, which are defined by the properties of the neutron collimator.

3.2.4. Design and properties of the neutron collimator

Design

The design of the neutron collimator can be seen in figure 3.6. The collimator itself consists of three layers of 2.3 mm thick ^{6}Li enriched rubber sheets, resulting in a total collimator thickness of nearly 7 mm. A circular hole with a diameter of 2 mm was drilled into the ^{6}Li rubber as beam aperture. The collimator is placed on a stepper motor driven slide to be adjustable in height. This strongly eases the alignment of the setup (ch. 3.2.2). Another advantage of this movable collimator is that it can be easily removed from the beam to collect small radiographies of the sample. This proved to be useful for radiography driven PGAI.

After the neutron collimator is aligned and the sample positioning has been done, it is advisable to cover the ^{6}Li-sheets with a window of boron carbide, which proved to reduce the γ-ray background significantly. This background partly originated from the interaction of fast neutrons, that are created in the ^{6}Li-sheets of the collimator, with the surrounding materials. The boron carbide instead creates low energy γ-ray background, that can be shielded with lead.

Examination of neutron scattering effects and neutron collimator response

The dimensions of the collimated neutron beam at isocenter position predetermine the maximal reachable spatial measurement resolution in x- and y-directions. One ef-

[1] Basically this function is the linear combination of a common approximation of the Heaviside function.

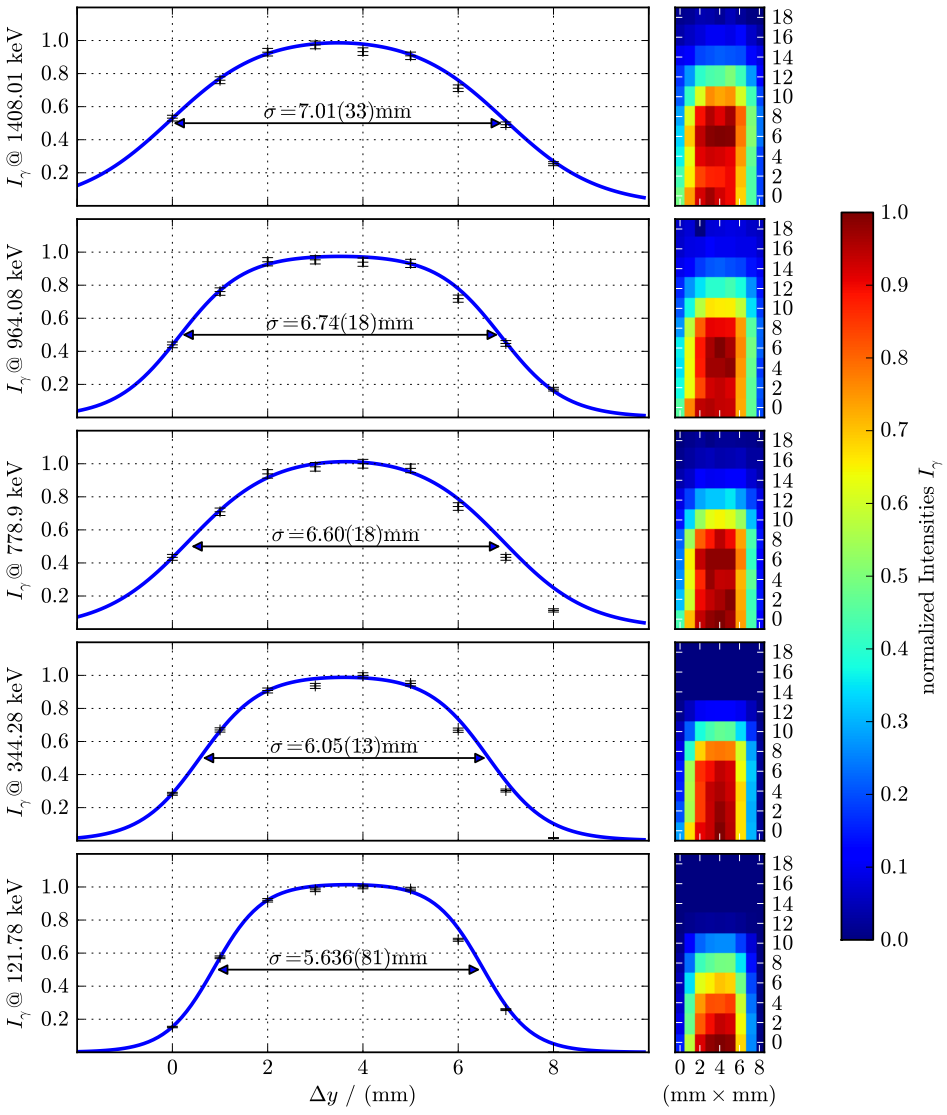

Figure 3.5.: Resolution (left) and intensity profile (right) of the γ-collimator. The intensities for the resolution fits have been taken from the bottom line of the profile grids (i.e. the height of the isovolume).

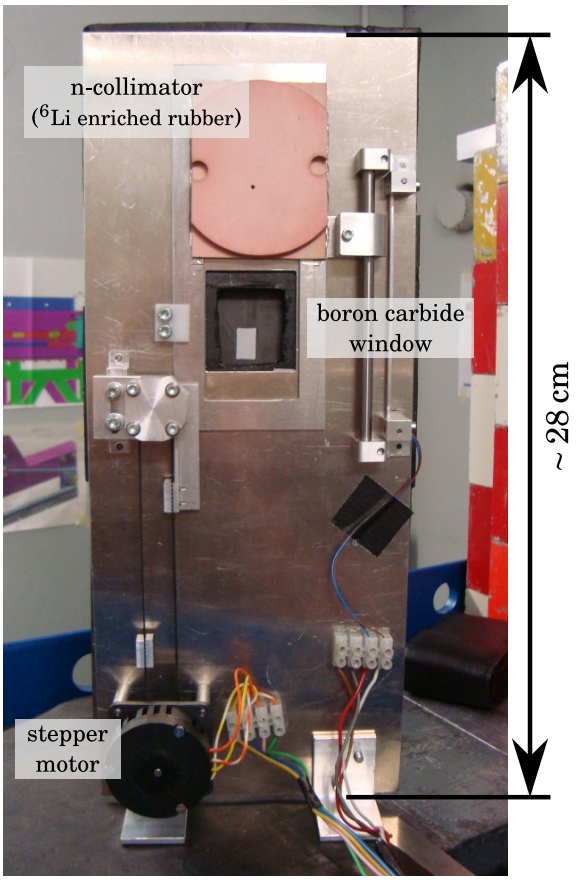

Figure 3.6.: Movable neutron collimator

fect that is lowering the achievable resolution above the size of the neutron collimator is beam broadening. Due to the inevitable divergency of the beam, the small neutron beam spot at the collimator position is broadened on its way to the isocenter. The order of this effect can be estimated by measuring the size of the n-collimator spot on the scintillator of the neutron tomograph. Another option is to calculate the broadening effect from the so-called $\frac{L}{D}$-ratio, which is a measure for the beam divergency, where L denotes the length of the neutron flight path and D is the dimension of a projection of a "zero"-sized dot over the flight length. The $\frac{L}{D}$-ratio has been measured in [Ebe09] to 168 ± 10 for the PGAA neutron beam. Both approaches gave a beam broadening of less than 10 % at isocenter position.

As already indicated in chapter 3.2.3 another effect that influences the spatial resolution are neutron scattering effects inside the investigated sample. By the interaction with the sample material neutrons are scattered outside of the initially illuminated chord-volume and create γ-rays in the surrounding sample regions, thus enlarging the active measurement volume.

To check if this effect will have a problematic magnitude and to get an impression

Table 3.2.: Dimensions of the three test plates (measured with a sliding rule)

Material	Thickness
Cu	(3.00 ± 0.05) mm
Fe	(3.00 ± 0.05) mm
PVC (C_2H_3Cl)	(2.95 ± 0.05) mm

of the response function of the collimated neutron beam, the following experiment has been performed in 3D isovolume configuration: Three plates, one made from copper, one from iron, and one from PVC[2] (fig. 3.7(a)), have been sticked together and moved along the beam in vertical (fig. 3.7(c)) and horizontal alignment (fig. 3.7(d)), crossing the beam along the x-axis, from right to left, and along the z-axis, from bottom to top, respectively. For the movement along the x-axis seven positions in intervals of about1.7 mm and along the z-axis eight positions in intervals of about 1.3 mm have been measured.

When the beam hits an intersection of two plates we expect to see both plate materials in the γ-ray spectra with similar intensity. For positions directly after the intersections, when the beam only hits one single plate, ideally only this single material should be visible in the spectra, but due to the scattering effects the adjacent plate will influence the measurement.

The thicknesses of the three plates are listed in table 3.2. For the analysis selected peaks of copper, iron, and chlorine, that interfere as little as possible with neighboring peaks or the background, have been fitted ($E_{\gamma,\mathrm{Cu}} = 278\,\mathrm{keV}$, $E_{\gamma,\mathrm{Fe}} = 352\,\mathrm{keV}$, $E_{\gamma,\mathrm{Cl}} = 1164\,\mathrm{keV}$). The areas $\mathcal{N}_\gamma$ of the resulting fits have then been normalized to the largest area $\mathcal{N}_{\gamma,\mathrm{max.}}$ for each element.

Under ideal circumstances, i.e. neglecting scattering and attenuation effects, and assuming an ideal collimator as well as ideal sample shapes and orientations, the following peak areas are expected in dependency of the plate position.

$$\mathcal{N}_\gamma(x) \begin{cases} = 0, & \text{n-beam misses the plate} \\ \propto A_{\mathrm{irr.}}(x), & \text{n-beam hits the plate partly (fig. 3.7(b))} \\ = \mathcal{N}_{\gamma,\mathrm{max.}} \stackrel{!}{=} 1, & \text{n- beam hits the plate with full area} \end{cases} \tag{3.2}$$

The irradiated area $A_{\mathrm{irr.}}$ is the circle segment of the neutron collimator that covers the edge of the plate. The formula for this area is given in standard literature:

$$A_{\mathrm{irr.}}\left(x - x_{\mathrm{edge}}\right) = A_{\mathrm{segment}}(h) = r^2 \arccos\left(1 - \frac{2h}{d}\right) - \left(\frac{d}{2} - h\right) \cdot \sqrt{dh - h^2}. \tag{3.3}$$

A function has been modeled after eqs. (3.2) and (3.3) and fitted to the measured peak areas along the scanning line (fig. 3.8) for vertical and horizontal orientations of the plates. The FWHMs should give the thicknesses of the plates, because (ideally) the

[2] **P**oly**v**inyl **c**hloride

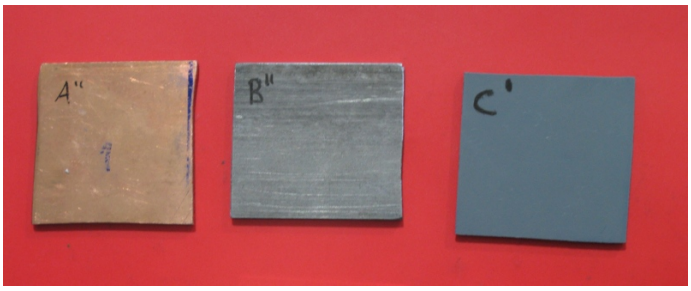

(a) copper- (A), iron- (B) and PVC-plate (C)

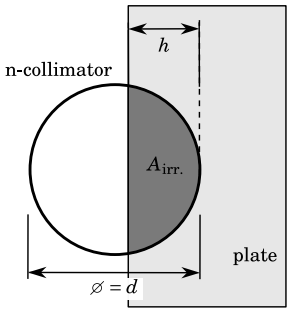

(b) Calculation of the irradiated area during the scan of the edge of one plate

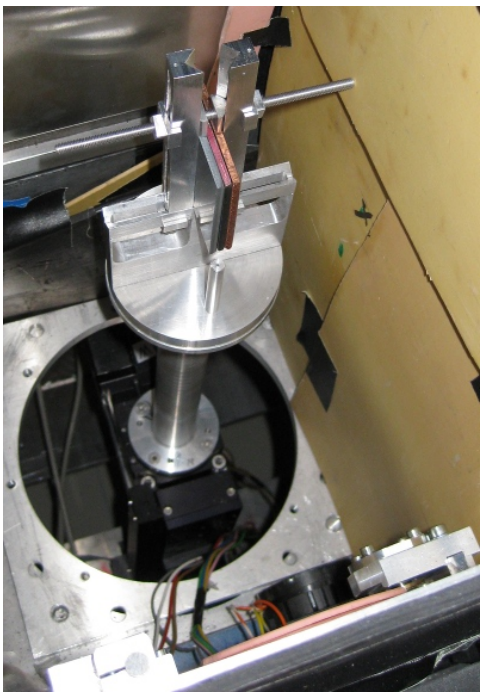

(c) Plates in vertical configuration

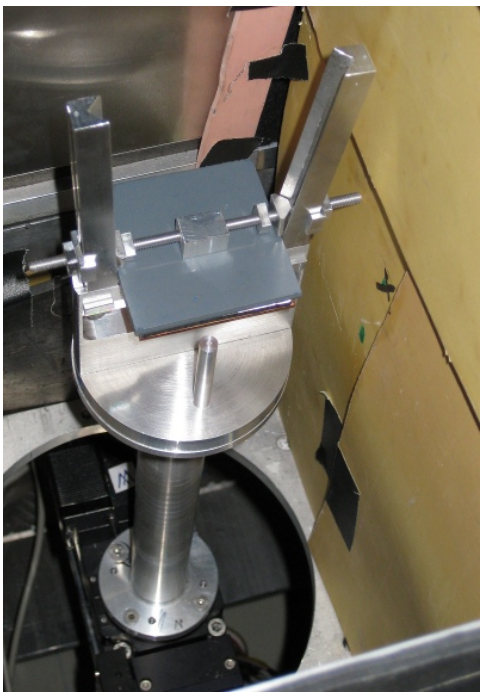

(d) Plates in horizontal configuration

Figure 3.7.: Test plates for the scan of the neutron collimator

collimated neutron beam irradiates the plate with exactly half its full area, when aiming directly at the edge of the plate, thus resulting in exactly half the maximum intensity. The thicknesses determined by this way represent the real thicknesses quite well, with a small tendency of being a bit larger than the thicknesses given in table 3.2. This can be explained by the scattering of neutrons inside the plates.

One can estimate the effect of neutron scattering from figure 3.8 by looking at the peak intensities that lie outside of the idealized curve. Function (3.1) should be a good approximation for the real peak intensities. With exception of the chlorine distribution for the horizontal measurement, the peak intensities due to neutron scattering shrink to less than 5 % within 0.5 mm. Even for the differing measurement the intensities shrink to less than 5 % within 1 mm.

A detailed analysis of the influence of neutron scattering effects in different material has been done in [Bel06], showing that neutron scattering can be especially a problem for light *low-Z* elements. This explains the higher scattering observed in the PVC plate, which contains a significant amount of hydrogen ($Z = 1$).

3.3. Sample supports

One task during the ANCIENT CHARM project was the design of universal sample supports [Kud08b], which should

- be suitable for smaller objects of different geometries,
- provide firm support without damaging the valuable objects,
- keep the objects in an unique position during the measurements and the transportation to different measurement facilities,
- provide some reference markers, which should be detectable by the used neutron methods for the sample positioning and the later alignment of different data-sets, and
- influence the conducted measurements as little as possible.

The final design of these sample supports can be seen in figure 3.9. These supports were designed and manufactured at fine mechanics workshop of the Institute for Nuclear Physics of the University of Cologne [Kud08b], from aluminum, with a low manganese fraction (≤ 0.1 %). Manganese is a common admixture to aluminum, but has the disadvantage of relatively high activation when being irradiated by neutrons, thus its fraction should be as minimal as possible. The supports are able to hold objects of up to about 5 cm × 8 cm (fig. 3.9(a)). For many geometries they can be adjusted in height and width to firmly hold the analyzed samples without damaging them. For very fragile samples or special geometries they can be adapted with specially

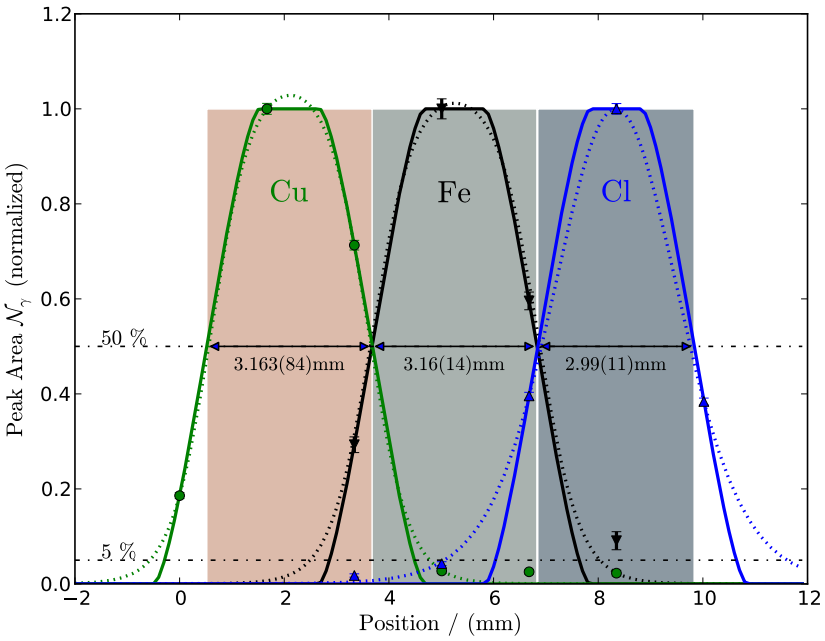

(a) Vertical orientation of plates

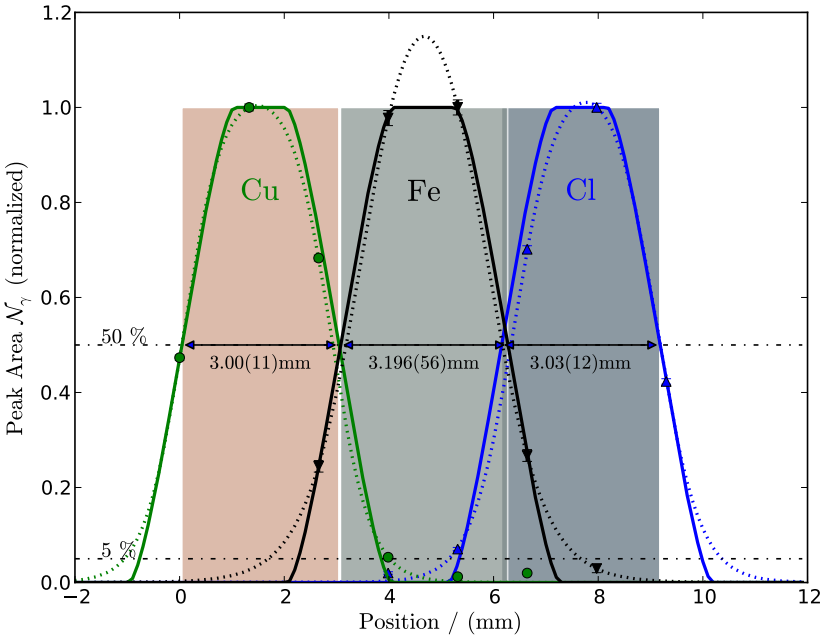

(b) Horizontal orientation of plates

Figure 3.8.: Normalized peak areas for the scanning of the three test plates along the neutron collimator. (continuous lines: ideal function (3.2), dashed lines: "bump" function (3.1))

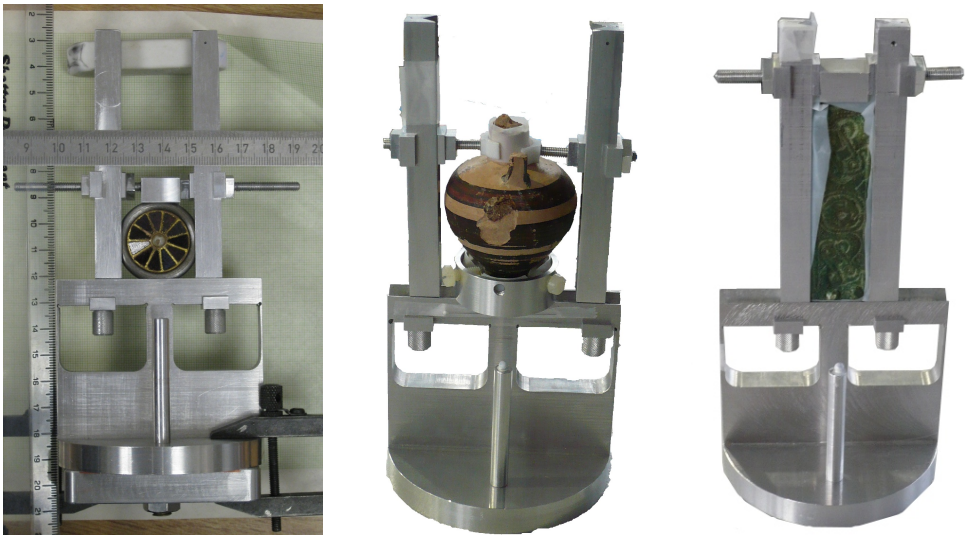

(a) Size of the sample supports. The replica of an ancient fibula is placed into the support.

(b) Adapted sample support for a ceramic vase from 700–800 B.C. (see chapter 4.4)

(c) Ancient bronze belt point in sample support protected by thin Teflon inlays (see chapter 4.5)

Figure 3.9.: Universal sample supports developed for the neutron imaging measurements

designed clamps or base supports (see e.g. figure 3.9(b)). Although aluminum is a relatively soft material the samples can be further protected by thin Teflon[3] inlays (see e.g. figure 3.9(c)).

Positions for reference markers are provided, e.g. on an about 4.5 cm long pole in the front. For an unique alignment of the sample at least four reference markers, not lying in one plane, have to be attached to the support (see chapter 4.1).

The orientation of the support's baseplate is uniquely aligned to the moving table's surface by two small aluminum pins, thus allowing an accurate, reproducible positioning of the sample support on the moving table.

These sample supports have been in regular use during the measurements on different facilities and proved to meet the formulated requirements well for the different measurement methods. For the measurements that are described in this work, these supports, together with some specialized similar supports of earlier design, have been used for most of the measurements. Exceptions are the cases where the analyzed objects were to large to fit into these supports.

[3]Teflon™ is a trademark of DuPont. Its correct chemical name is *Polytetrafluoroethylene*, but due to the wide-spread use and better recognition the shorter trademark name is used here.

3.4. Data acquisition system

3.4.1. Overview and requirements

For PGAA/PGAI/NT measurements at the PGAA setup at FRM 2 several hardware devices had to be controlled and synchronized:

- An analog Multi-Channel-Analyzer (MCA), developed at the Institute for Nuclear Physics in Cologne, for the acquisition of the PGAA γ-ray spectra,
- for the collection of PGAI spectra a digital acquisition system from the company XIA[4] was used during the initial development phase,
- a motor controller for sample positioning,
- a digital CCD camera from the company PCO[5] for the acquisition of the neutron radiographies, and
- a programmable "modular safety system" by the company PILZ[6], which controls the parameters of the neutron beam, like neutron shutter and attenuator positions, and takes care of the safe operation of the setup.

It is highly desirable to have a control and measurement system which can be run in an unattended "batch" mode, to allow the acquisition of multiple samples for PGAA, or multiple sample positions for PGAI, without the need for an experimenter to be "on-site" all the time. Especially for PGAI measurements, where there may be 100 measurement positions or more, a manual intervention for each position change is nearly infeasible. The same is true for NT measurements, where a large number of radiographies has to be taken. The automation of the measurement process increases the exploitable, valuable measurement time, especially for e.g. measurements over night or the weekend.

For an automated operation the acquisition system has to follow the following steps:

1. The sample must be moved (for PGAA/I) or turned (for NT) to the specified position.
2. When the sample has reached the final position/angle, the beam has to be prepared, i.e. the shutter has to be opened and the desired beam attenuators have to be positioned into the beam.
3. After the correct preparation of sample position and beam the data acquisition can be started, i.e. the MCA is set to acquisition mode for the previously defined time span or the CCD camera's acquisition is triggered.

[4] http://www.xia.com
[5] http://www.pco.de
[6] http://www.pilz.com

4. Afterwards the acquired γ-ray spectra or radiographies and other relevant measurement parameters have to be saved.

5. For the remaining positions the steps above have to be repeated until all positions/angles have been measured.

6. Finally, after the last measurement is finished, the beam shutter should be closed to avoid unnecessary activation of the sample.

3.4.2. Initial acquisition system

During the setup and development phase of the PGAI/NT setup a software developed at the Institute of Isotopes[7] in Budapest and based on the program IGOR PRO from WAVEMETRICS[8] was used for the control of the positioning table and the digital acquisition system. For Neutron Tomography the camera was controlled through the CAMWARE program from PCO. The synchronization between CAMWARE and the IGOR PRO based software was achieved via a small, self-programmed micro-controller board[9] which allowed to trigger the CCD camera via a simple `ASCII` based network protocol.

PGAA measurements were performed under the LINUX operation system with some self-written C-programs in combination with a software that was originally developed for the practical course for teachers at the Institute for Nuclear Physics in Cologne.

This acquisition system had several shortcomings:

- PGAA and PGAI/NT measurements used completely disjunct programs which even required different operating systems.
- The analog Cologne MCA could not easily be synchronized with the PGAI acquisition system. Because the digital system only allowed one gate signal for all inputs it was not possible to acquire Compton suppressed γ-ray spectra with both present detectors at the same time during PGAI measurements.
- The user interface of the acquisition system was not separated from the main control code. Thus, a crash or unintended reboot of the client PC aborted the running measurements and in many cases even required the new alignment of the positioning table.
- For PGAA batch measurements only some basic shell scripts existed, which were separate from the user interface used for single PGAA measurements.

To unify the whole acquisition system and to make it more user-friendly, less error-prone, and more flexible, a complete new acquisition infrastructure was developed during this work.

[7] Institute of Isotopes, Hungarian Academy of Sciences, Budapest, Hungary: http://www.iki.kfki.hu
[8] http://www.wavemetrics.com
[9] http://www.ethernut.de

3.4.3. PGA-Acquisition-System (PAcSy)

For the design of the new acquisition system PAcSy (**P**GA-**Ac**quisition-**Sy**stem) the focus was put on:

Modularity It should be easy to add new devices or exchange one device.

TCP/IP based Client-Server-Architecture Remote control and operation should be easy and reliable. It may be necessary to connect different devices to separate computers (e.g. due to electrical grounding reasons), thus device control should not be bound to a single computer.

Use of open and common standards The use of common open standards ensures that the system may be ported to other systems easily if desired and increases the chance that the libraries and programs on which the system relies will still be supported in the future. Furthermore it eases the communication with external peripherals, if this is desired in the future.

A schematic overview of the PAcSy infrastructure is shown in figure 3.10. The basic hardware communication is handled through new self-written C-libraries (libcomca, libtmcl,...) which provide a Python interface via auto-generated SWIG[10] wrapper code. Built on these libraries, a server was written for each device, which exports the devices functionality to the TCP/IP-network via XML-Remote-Procedure-Calls (XML-RPC) [US03] utilizing the Python standard module `xmlrpclib` [Pyt10]. These servers can be accessed from other computers on the Network via several user-friendly client programs developed with the Python-GUI-framework PyQT [RC10]. A central server takes care of the synchronization of the different devices, and manages the measurement queue. The central 'MeasurementClient' can be used to read the device configuration set by the single device clients and to start or queue an acquisition. Details about the used hardware devices and the device libraries together with some small programming examples are given in chapter A.2.

The new acquisition system is now in regular use for PGAA measurements and has already been successfully used for some PGAI measurements.

[10] http://www.swig.org/

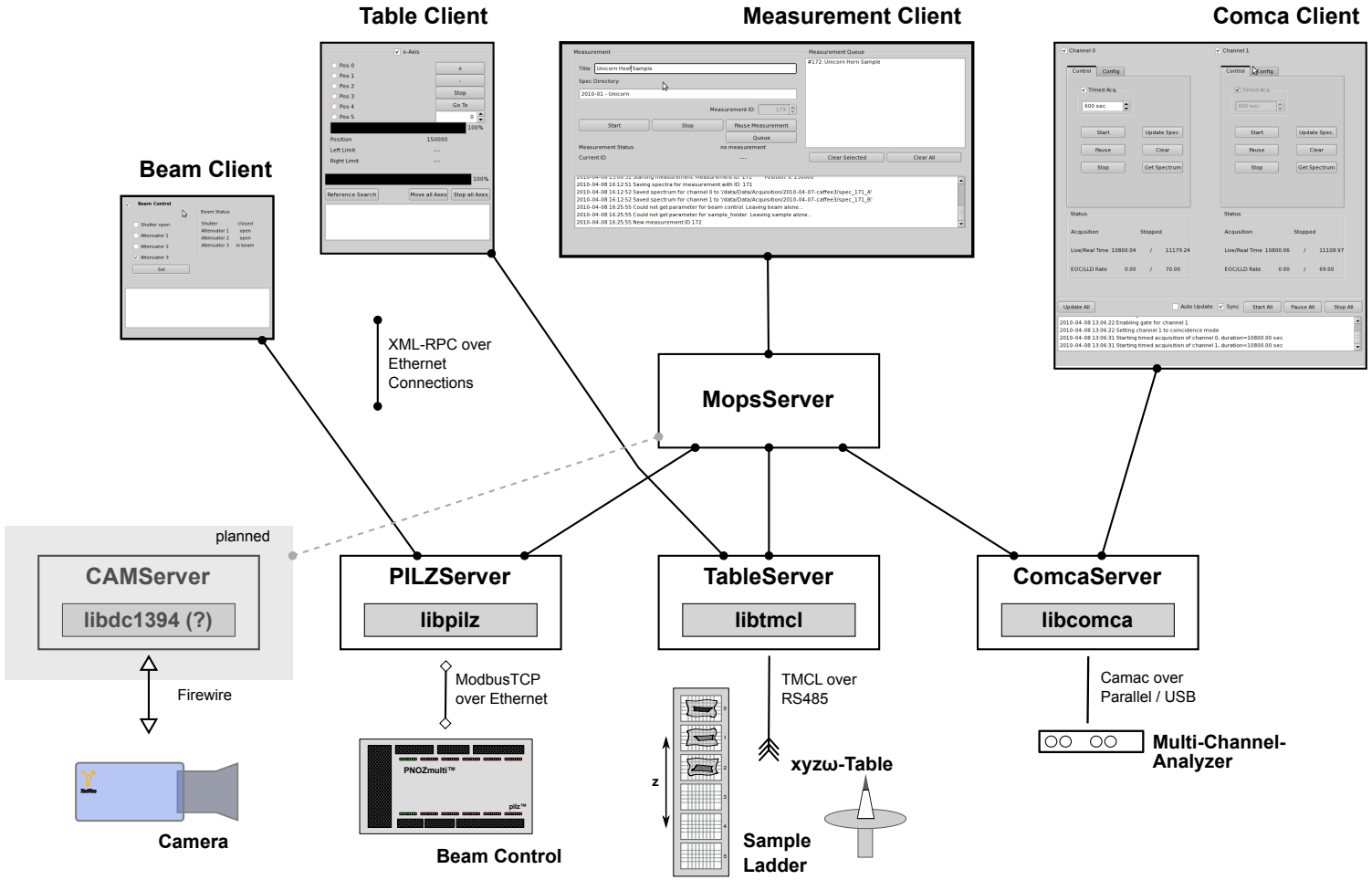

Figure 3.10.: Overview of the PAcSy data acquisition system

4. Measurements and analyses

4.1. Sample positioning and registration

4.1.1. Introduction

A critical task for the extensive analysis of the given samples is the correct positioning during the measurements and the correct registration, i.e. alignment, of the different data-sets from NT, PGAI, NRT, etc., afterwards. For the correct positioning of a sample during PGAI measurements one may perform, in simple cases, a so-called *radiography-driven* PGAI, which means the positioning of the selected sample locations in the collimated neutron beam, with the help of online radiographies. This is most suited for 2D-PGAI measurements in chord configuration, because the correct positioning in front of the γ-collimator cannot be done solely with this method. The other disadvantage is the urgent need for a radiograph at the setup, which may not be given for all setups.

Additionally this approach does not solve the registration problem: The facilities where different data-sets are acquired have different geometries, i.e. different sample moving tables, other detector positions, etc., hence they do not share a common (x, y, z, ω)-coordinate system. To address these problems, it was decided to provide a

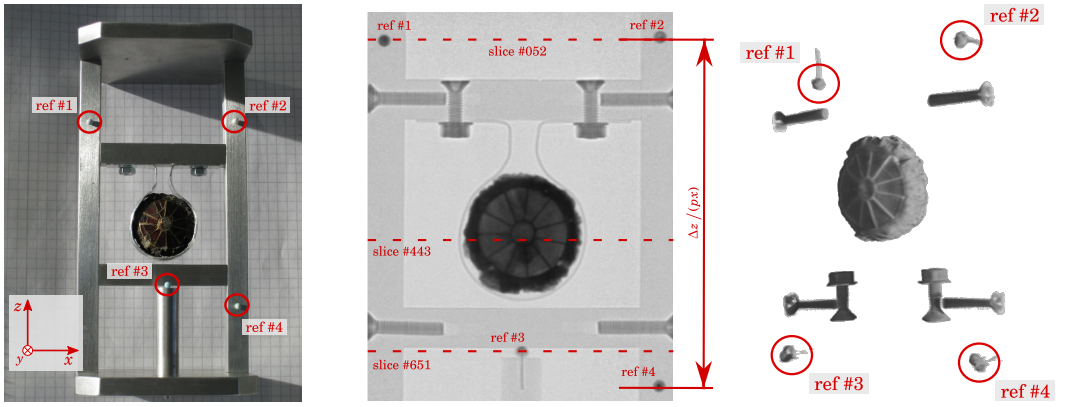

(a) Reference markers at four distinct positions on the sample holder for a fibula object (see. chapter 4.7)

(b) Normalized radiography of the fibula. The reference markers are clearly visible and can be used for (pixel ↔ mm)-conversion

(c) Reference marker positions in the final NT reconstruction

Figure 4.1.: Reference markers from needle heads painted with Gd blended nail polish used for positioning and data-set registration

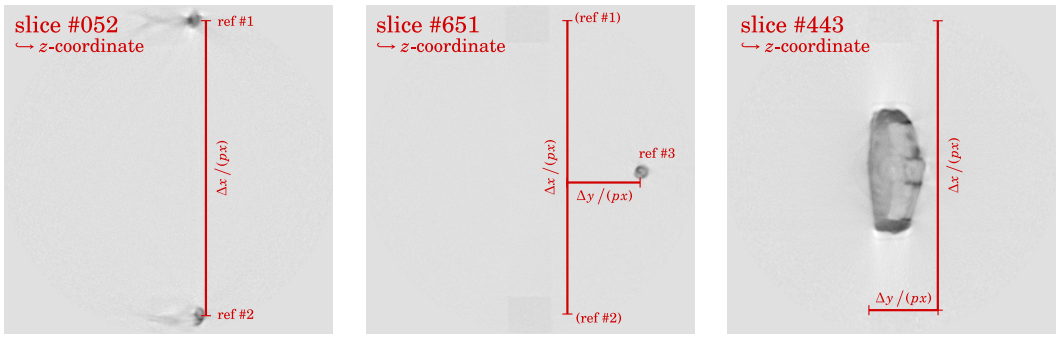

(a) x-coordinate pixel ↔ mm conversion

(b) y-coordinate pixel ↔ mm conversion

(c) Determination of a measurement position inside the object

Figure 4.2.: Determination of measurement positions with the help of the reference markers

common reference coordinate system for each object, by attaching reference markers to the sample supports [Sch09]. These reference markers should be small enough to define their location with the desired precision (≈ 1 mm accuracy was seen as adequate, with respect to the expected measurement resolutions), while still being large enough to be easily detectable by the different neutron methods. As mentioned in chapter 3.3 at least four reference markers, that must not lie in one plane, are needed for the unique alignment of a sample in three-dimensional space. Another important request is that the markers must never cover the analyzed sample during a rotation, because this will, due to the high absorption properties of the markers, disturb the NT reconstruction process. For PGAI/NT needle heads of about 3 mm diameter that were painted with gadolinium blended nail-polish, proved to be suitable (see figure 4.1). They are clearly visible in the radiographies and the final reconstructions (fig. 4.1(b) and (c)) and are clearly recognizable in the PGAI spectra. For a determination of their position with an accuracy of the desired 1 mm one should refer all coordinates to the center of the markers, which can be determined quite accurately.

As it turned out later during the project the visibility of these markers for the methods utilizing higher energetic neutrons, as NRCI/NRT, was not as good as desired. For these methods small silver pieces were used as reference markers. This does not impose a problem for later registration, because one can easily transform the known reference system of the gadolinium markers to the known system of the silver pieces. Anyway it may be a better solution for future measurements to have reference markers of combined silver and gadolinium components, e.g. by painting the small silver pieces with the gadolinium blended nail polish.

4.1.2. Positioning

The reconstructions of a NT measurement deliver an ideal tool to identify interesting positions for e.g. 3D-PGAI measurements. They deliver the locations of interest in

units of reconstruction pixels and slices, which have to be converted to the coordinate system of the measurement setup. In praxis this is normally given through (x, y, z, ω)-steps of the stepper motor driven sample table. This conversion can easily be done with the help of the reference markers. Their positions in reference to a known position of the sample table, i.e. the center of the supporting base plate, can easily be measured with e.g. a sliding rule. This, together with their pixel-positions in the NT gives the desired (pixel $\leftrightarrow$ mm)-conversion (figure 4.2). Together with the known isocenter position (chapter 3.2.2) the final measurement positions in motor steps are now available.

It may be advisable to rotate the sample during the measurements, e.g. to minimize self-absorption and -shielding effects (chapter 2.4.3 and 4.2). Because the calculations so far were done for a sample under 0° the motor positions for such measurements have to be transformed with a rotation matrix

$$\begin{pmatrix} \Delta x_{\text{rot}} \\ \Delta y_{\text{rot}} \end{pmatrix} = \begin{pmatrix} \cos\varphi & -\sin\varphi \\ \sin\varphi & \cos\varphi \end{pmatrix} \cdot \begin{pmatrix} \Delta x \\ \Delta y \end{pmatrix}, \tag{4.1}$$

with the (x, y)-coordinates given relative to the center-of-rotation of the sample table.

4.1.3. Registration

Because all measurement data-sets are finally available with positions relative to the reference markers they can now easily be aligned for detailed combined analysis and interpretation or mutual correction (chapter 4.2). In figure 4.3 the combination of a NT reconstruction and a single full 3D-PGAI data-set is shown. Both 3D data-sets have been imported into a standard visualization software. For the purposes of presentation and interpretation an alignment "by eye" utilizing the reference marker positions is sufficient. For correctional calculations the real relative coordinates of measurement positions and reference markers have to be used. Due to the number of measurement points it is strongly advisable to use dedicated computer programs for that [Sch10].

4.2. Calculation of the cold neutron flux inside samples

As mentioned in chapter 2.4.3 the self-attenuation and -shielding effects of γ-rays and neutrons hamper the quantitative analysis of PGAI measurements. Here a method is presented which enables the estimation of the cold neutron flux at each position inside the sample using the data acquired with cold Neutron Tomography. Because the imaging process of cold NT relies on the attenuation of cold neutrons inside the sample, it delivers a map of these attenuation properties, in terms of gray-values, in the reconstruction. For the calculation of the cold neutron attenuation factors μ from these gray-values g a proper conversion $g \rightarrow \mu(g)$ is needed. To obtain this assignment one may utilize radiographies of the analyzed object (fig. 4.4(a)) and compare their gray-value map with the gray-values of an open beam image (fig. 4.4(b)), which correspond to an attenuation of $\mu = 0$.

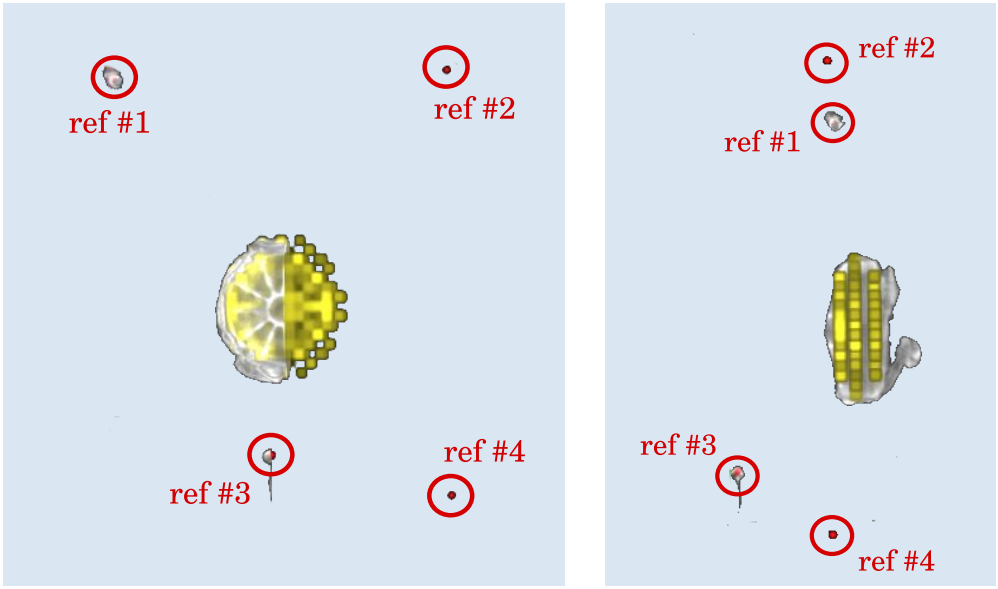

(a) Front view: The NT visualization has been cutted in the middle of the fibula.

(b) Side view showing the three measurement layers

Figure 4.3.: Combined data-sets of a NT reconstruction (gray) and the 3D-PGAI map of gold (yellow) in the fibula sample (see. chapter 4.7)

In the following discussion G denotes gray-values in the radiographies (e.g. fig. 4.4(a) and (b)) while g denotes gray-values in the reconstruction slices (fig. 4.4(c)).

The gray-value $G(x,z)$ at position (x,z) in the radiography is, neglecting noise effects in the imaging process, proportional to the light intensity created at the corresponding scintillator position and thus proportional to the number of neutrons hitting the scintillator at this position:

$$G(x,z) = C \cdot I_{\mathrm{n,scint.}}(x,z) + G_0. \tag{4.2}$$

The offset G_0 takes care for the proper consideration of the minimal neutron intensity that can be detected by the tomograph. For an absolute determination of the cold neutron flux one may perform an activation measurement of e.g. gold at several defined scintillator position and determine C and G_0 in eq. (4.2) by fitting these measured neutron intensities to an open beam radiography (fig. 4.4(b)) which was taken under the same beam conditions. Assuming a parallel beam and a negligible neutron intensity loss for the short flight path through the sample chamber eq. (4.2) then gives the initial neutron intensity distribution of the inhomogeneous neutron beam $I_{\mathrm{n},0}$.

The attenuation of single energetic cold neutrons through material can be described by the general attenuation law:

$$I_{\mathrm{n}}(y) = I_{\mathrm{n}}(y_0) \cdot \exp\left(-\int_{y_0}^{y} \mu(l)\,\mathrm{d}l\right). \tag{4.3}$$

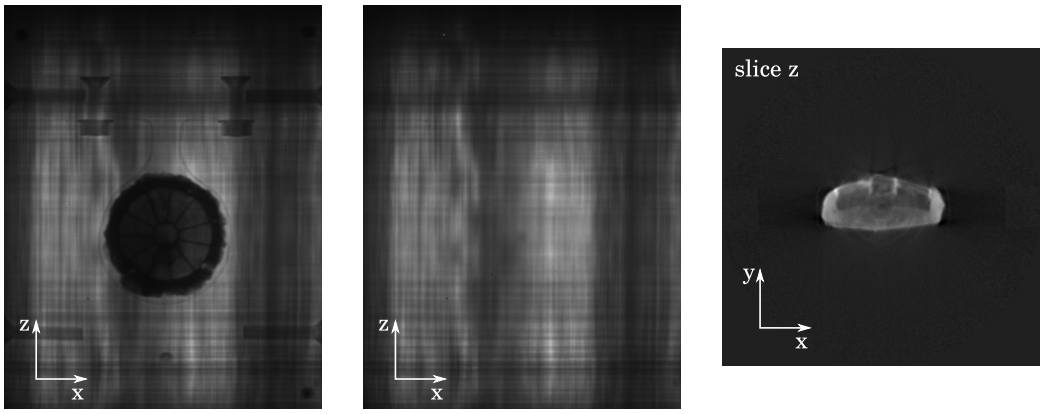

(a) Radiography of an ancient fibula. (Not corrected with open beam image)

(b) Open beam radiography

(c) Slice in the reconstructed tomography

Figure 4.4.: Calculation of neutron absorption factors from gray-values in reconstruction slices

If we now place the sample in the beam the overall attenuation map of the sample at scintillator position results to:

$$\mu_\Sigma(x, y_{\text{scint.}}, z) := \int_0^{y_{\text{scint.}}} \mu(x,l,z)\,\mathrm{d}l = -\ln\frac{I_\text{n}(x, y_{\text{scint.}}, z)}{I_0(x,z)} \tag{4.4}$$

$$= -\ln\frac{G(x,z) - G_0}{C \cdot I_0(x,z)}, \tag{4.5}$$

with $y_0 := 0$ and $I_0(x,z) := I_\text{n}(x, y_0, z)$. Assuming again that the neutron attenuation outside the sample, and thus outside the volume covered by the reconstruction, can be neglected, the overall attenuation $\mu_\Sigma(x,d,z)$ should be expressible in gray-value sums along the neutron flight path in the reconstruction. Of course the orientation of the reconstructed sample has to be adjusted to represent the orientation during the radiography exactly.

$$\mu_\Sigma(x,y,z) = \mu_\Sigma \circ \left(\sum_{l=0}^{y} g(x,l,z)\right) =: \mu_\Sigma\big(g_\Sigma(x,y,z)\big). \tag{4.6}$$

In figure 4.5 all μ_Σ values calculated with eq. (4.5) from the radiographies have been plotted against their corresponding gray-value sums (eq. (4.6)). With the radiography sizes of 800 px × 600 px this results in 480000 distinct points. The distribution in figure 4.5 has been fitted with a linear relation:

$$\mu_\Sigma(x,y,z) = c \cdot g_\Sigma(x,y,z) + g_0. \tag{4.7}$$

At the lower part of the distribution in figure 4.5 one can see a dense, quite flat region of points, which is originating from noise in the radiographies (vertical extent), and

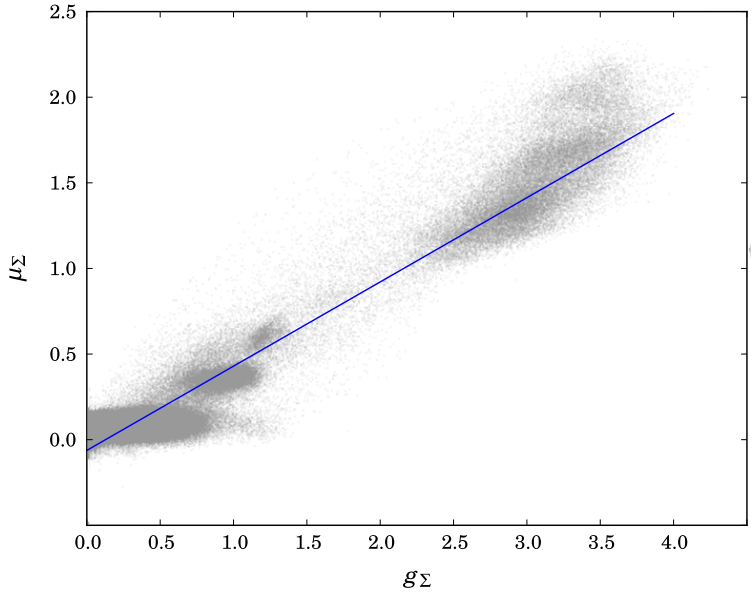

Figure 4.5.: Sum of gray-values in reconstruction g_Σ vs. calculated total neutron attenuation factors μ_Σ at scintillator position

noise and artifacts in the reconstruction (horizontal extent). This has to be taken into account for the quantitative flux calculations later.

Combining the above equations one yields now with eq. (4.3):

$$I_n(x,y,z) = I_0 \cdot \exp(-c \cdot g_\Sigma(x,y,z) - g_0). \tag{4.8}$$

With eq. (4.8) it is now possible to estimate the cold neutron flux at each single position inside the analyzed sample by summing up the gray-values up to the point of interest.

The specialized program NESSAS NT[1] has been written to perform these calibrations and calculations. It delivers the estimated cold neutron flux at each point inside the analyzed samples for arbitrary orientations with respect to the neutron beam (see chapter A.1 for details). Some example results from the cold neutron flux calculations are shown in figure 4.6 for the measurements on an ancient fibula (see chapter 4.7). As mentioned above one has to regard the noise induced by the imaging process and by the reconstruction algorithm. With NESSAS NT this can be done by setting a threshold, which cuts away very low gray-values, that are probably due to noise. Of course this threshold throws away real neutron intensities below the given magnitude, too, thus one has to take some care while adjusting this parameter. To check the quality of these calculations, the neutron intensities that were measured with the radiographies during the NT have been compared with the neutron intensities calculated via eq. (4.8) for different sample orientations. From the images in figure 4.7 it

[1] **N**eutron **S**elf **S**hielding correction in **A**rchaeological **S**amples via **N**eutron **T**omography

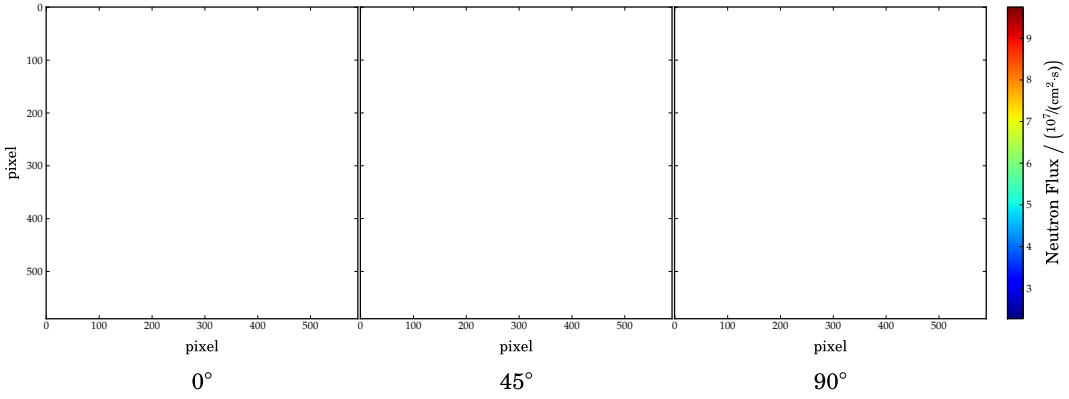

Figure 4.6.: Calculated neutron flux in one reconstruction slice for the fibula sample under different orientations respective to the beam

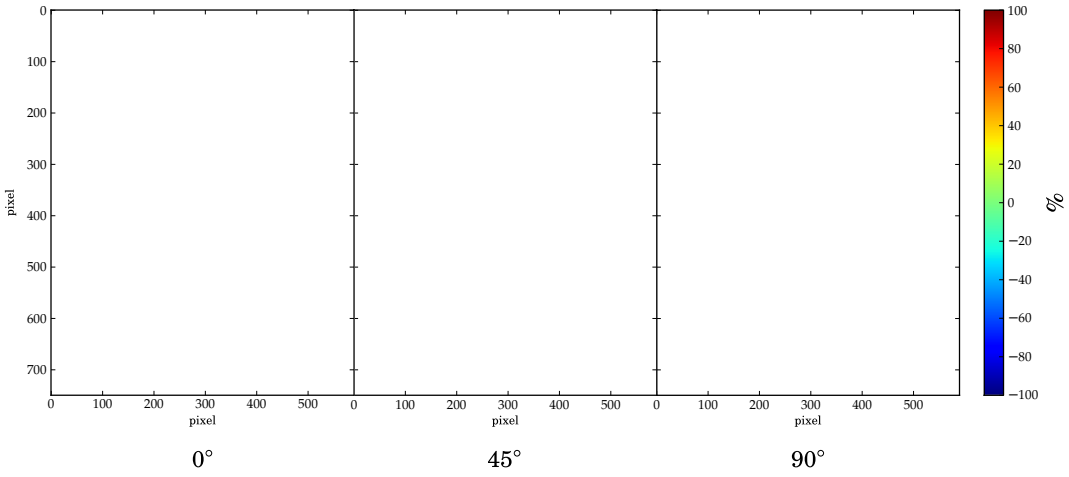

Figure 4.7.: Deviations of the calculated neutron intensity at scintillator position from the neutron intensity determined with the respective radiographies ($I_{\mathrm{calc}}/I_{\mathrm{radio}} - 1$)

gets clear that the proposed method seems to work quite well for low and medium overall neutron attenuation. For high neutron attenuation, that can be observed at the outer ring of the fibula or at the 90° orientation, the differences become quite high. This can be due to several reasons:

Imperfect modeling of the $g_\Sigma \leftrightarrow \mu_\Sigma$ relation

As one can see in figure 4.5 our modeled linear function (4.7) deviates from the $g_\Sigma \leftrightarrow \mu_\Sigma$ pairs especially for high values. The higher values tend to lie above the modeled line, thus the estimated neutron attenuation will be *lower* than the real attenuation in this region. This explains why the *calculated* neutron intensities in figure 4.7 tend to be *higher* than the measured intensities for the high attenuation regions.

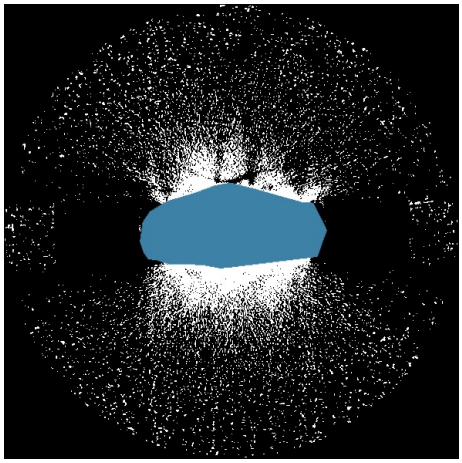

Figure 4.8.: Visualization of the noise in a reconstruction slice of the fibula sample by greatly increasing contrast and brightness parameters. The real position of the fibula is marked in blue.

Non-parallel neutron beam

The PGAA setup at FRM 2 is not primary dedicated to Neutron Tomography, thus its beam has not been optimized to be very parallel. In fact even the opposite is true: The beam is being slightly focused to gain higher neutron fluxes for PGAA/PGAI measurements (see chapter 3.1). It has been tried to compensate for this fact by extending the neutron flight path with a non-reflecting flight tube and cutting away the most divergent neutrons (chapter 3.2), but the measured divergency of $L/D = 168 \pm 10$ (see ch. 3.2) is significantly lower than what can be reached by dedicated neutron tomography setups; e.g. the ANTARES neutron imaging facility at FRM 2 has a ratio of $L/D \geq 400$.

Noise in the reconstruction

For the image at 90° in figure 4.7 one clearly sees regions near to the fibula where the calculated intensities are lower than the real intensities. In figure 4.8 the noise induced by the reconstruction is visualized by greatly increasing contrast and brightness on a reconstruction slice. It is clearly recognizable that in the front and back of the fibula the noise is extraordinary high. This is due to the specialties of the reconstruction algorithm (see chapter 2.2) and the asymmetry in fibula dimensions (thickness vs. width). For visualization purposes this noise can easily be removed by setting a threshold, but for quantitative analysis the increase of this threshold also falsifies real values.

Errors induced from the digital gray-value binning

The digitizing process of the radiography images maps small neutron intensity regions to fixed bins in the gray-scale images, thus inducing a small error. Because the attenuation has an exponential influence on the neutron intensity and the gray-value itself is linearly dependent of the intensity this error is changing over the full gray-

scale range. In [Hib97] the effect of the digital binning process on the error made in quantitative radiography imaging has been investigated for thin samples and low gray-scales. From the results in [Hib97] we can conclude that for our samples and the used gray-scale of 16 k bins this effect can probably be neglected.

Beam hardening

Due to the change of the neutron's energy distribution, caused by the larger absorption cross-sections for lower energetic neutrons, the effective attenuation is changed on the way through the sample. Lower energetic neutrons are absorbed more often, thus earlier, on their way through the sample, hence the neutron flux distribution is shifted to higher neutron energies, which have lower absorption probabilities. As a result the measured attenuation factors will seem smaller for thick samples than the real neutron attenuation.

The effect of beam hardening can be lowered by performing a full rotation of 360° of the sample and averaging the, under ideal circumstances equivalent (see chapter 2.2), projections at φ and $\varphi + 180°$.

Neutron scattering

The scattering of neutrons inside the sample influences their flight path and the position where they hit the neutron scintillator, thus introducing a deviation from the parallel beam approximation above.

The effects of neutron scattering and beam hardening on quantitative NT measurements have been investigated in [Has06], where a method is proposed to correct for them by iterative Monte-Carlo-Simulations. Quantitative values for half-thicknesses of neutron scattering, describing the likelihood of neutron scattering to appear in different materials, are given in e.g. [Bel06].

The biggest influence on the deviations observable in fig. 4.7, is probably due to the imperfect modeling of the $g_\Sigma \leftrightarrow \mu_\Sigma$ relation and the noise in the reconstructions. For a proper modeling of $\mu_\Sigma(g_\Sigma)$ it is advisable to use some easy, well-known calibration objects, e.g. homogeneous cylinders from different materials and thicknesses, where the real attenuation factors can be calculated precisely. From these calibration measurements the exact scintillator and CCD camera responses can be modeled and a more exact description of the neutron attenuation in terms of gray-value sums (eq. (4.6)) should be possible. Due to the homogeneity and known compositions of these calibration objects the neutron attenuation inside these objects can be calculated by eq. (4.3) and compared with the values returned from eq. (4.8). Unfortunately, due to the limited measurement time, these measurements could not be performed for this work.

As one sees from figures 4.8 the influence of noise is large at areas near to the sample. One may get rid of these noise influences by limiting the neutron flux calculations to the volume inside the sample. For the selection of this volume one has to determine its borders at each reconstruction slice. Due to the relatively high number of reconstruction slices (800 slices for the whole NT, ~ 250 slices covering the height of the analyzed fibula) it is highly desirable to automatize this process. Shape recognition procedures present in modern image processing software may be used as a basis

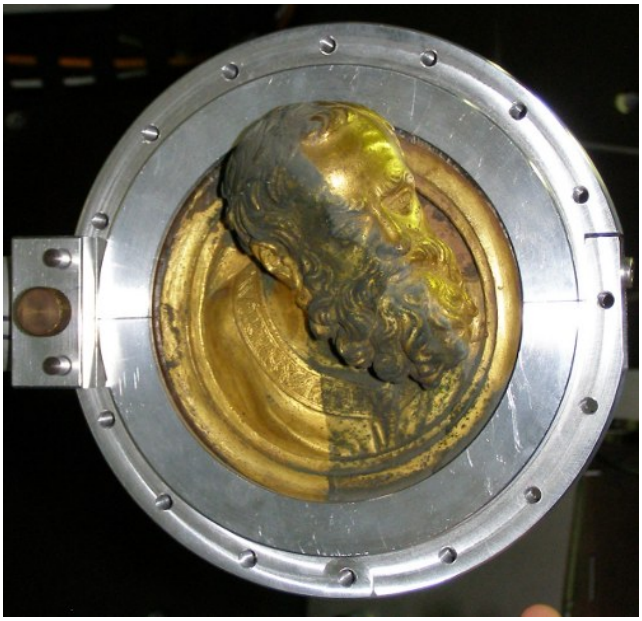

Figure 4.9.: Bronze head from the *Gates of Paradise* of the baptistery of Florence. The left part in the picture has been cleaned with a pulsed Nd:YAG laser, the right part with a bath in Rochelle salt solution. The middle part has been left uncleaned for comparison.

for this task. Unfortunately this does not tell us anything about the induced noise inside the sample volume, which is more critical for our estimations. For good corrections of this noise again a comparison of calculations for the neutron flux inside known calibration objects is advisable.

Taking the above-mentioned factors into account the results from figure 4.7 look quite promising for the correction of neutron-self-shielding effects, thus reducing the problems for quantitative PGAI.

4.3. PGAI surface measurements on a bronze head from Lorenzo Ghiberti

4.3.1. Object and motivation

During the ANCIENT CHARM project a gilded bronze head (fig. 4.9), created by the Italian artist Lorenzo Ghiberti[2] and normally located on the *Gates of Paradise* of the *Battistero di San Giovanni* in Florence, was analyzed with different neutron based methods [Fes09a]. The head was removed from the *Gates of Paradise* for restoration and to investigate the fabrication procedures used by the artist. Because this object is very bulky, it is very difficult to obtain information about the elemental composition

[2] * 1378, † 1455

from deep inside the object with cold neutrons. Neutron and gamma attenuation effects have big influence on points inside such a massive sample and would distort the PGAI results significantly. Another aspect is that due to the high absorption effects inside the object the measurement times would have to be very long to gain significant statistics in the γ-ray spectra. As mentioned above long irradiation times can cause high, long-lasting activation of the sample, which requires long cooling down times to let the sample activation decrease. Because the sample was only available for analysis for a very short time, this was unacceptable.

Thus another approach was chosen. Instead of performing a 3D-PGAI measurement, the measurements were done in 2D-PGAI chord-configuration. This increases the count-rates in the detector and thus allows shorter measurement times.

One question that had to be investigated was the effectiveness of different cleaning methods used on the surface of the bronze head. Over the years it was contaminated by e.g. air pollution. These pollutions can be very aggressive and damage the thin gilding layers. Two different cleaning methods have been tried on the presented head: chemical cleaning by a bath in a Rochelle salt solution and cleaning with a pulsed Nd:YAG[3] laser [Mat03, Sia03, Fes09b].

To address this question, 2D-PGAI was used as surface method. Four positions in each of the three different regions on the head had been analyzed. The results of these measurements concerning the effectiveness of the different cleaning methods are presented in [Fes09a] and [Fes09b]. The measurement and calibration procedures are explained here.

4.3.2. Alignment of the setup and sample positioning

The most crucial part of Surface PGAI is the correct positioning of the sample, which must be accurate in the direction orthogonal to the sample surface to about 100 µm. This demanded accuracy is much higher than what can be achieved by the positioning with the reference markers that are used for standard 3D PGAI. To achieve this accuracy the positioning process is done in two steps: one coarse positioning utilizing a laser and one fine position with the neutron radiograph of the PGAI/NT setup.

The aim of the coarse positioning with the laser is to determine suitable positions for the measurements and to fix the positions in the directions that are parallel to the surface. For this task the laser has to be aligned properly to follow exactly the line of the collimated neutron beam (fig. 4.10(a)). At first a calibration object, in this case the tip of a small copper-cone which is painted with gadolinium flavored nail-polish, is positioned into the known isocenter of the PGAI setup. Now the straight line from neutron collimator to the tip of the copper-cone gives the path of the collimated neutron beam. The laser beam now has to be aligned in that way that it first passes the neutron collimator and then hits the tip of the copper-cone. An auto-leveling laser, which ensures that the laser beam is always horizontally aligned, eases this process.

When the laser is properly aligned the sample can be brought into the measure-

[3] **N**eo**d**ymium-doped **Y**ttrium **a**luminum **G**arnet

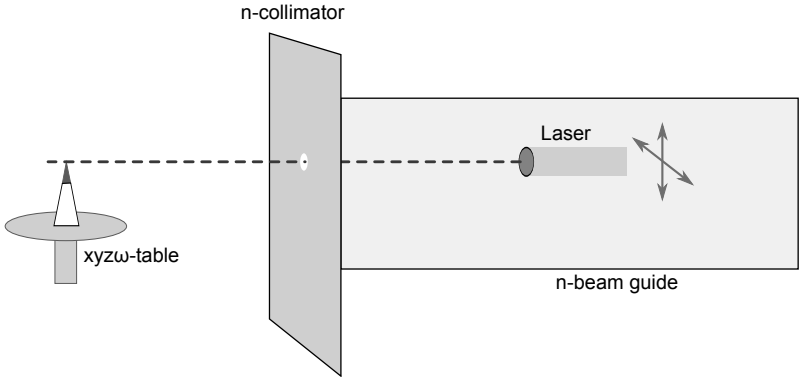

(a) Alignment of the laser for Surface PGAI sample positioning.

(b) Setup of the measurement positions utilizing an auto-leveling laser.

Figure 4.10.: Coarse alignment of the sample for Surface PGAI measurements

ment chamber. It now has to be positioned in such a way that the laser just grazes the surface of the sample at the desired measurement positions and does not hit the sample on another spot (fig. 4.10(b)). This delivers the coordinates of the measurement positions in directions parallel to the surface, but for the orthogonal direction, i.e. depth, this positioning is to coarse.

For the fine positioning in the orthogonal direction the neutron tomograph can be utilized At first a radiography with no sample in the beam is acquired to determine the exact position and dimensions of the neutron collimator. Afterwards the sample is moved to the previously defined measurement positions. It should now start to appear in the neutron collimator window on the radiography (fig. 4.11). From this image it can be estimated how deep the neutron beam reaches into the sample and how large the illuminated sample area is. The relation of pixels in the radiography to millimeter on the scintillator can easily be determined [Ebe09], but one has to take magnifica-

tion effects into account, which add an error to the determined values. Beginning from this start depth the sample is moved orthogonal to its surface in steps of the desired scanning resolution. The used (x, y, z, ω)-motor has a claimed accuracy of up to 2.5 µm [Fes09a] thus introduces a negligible error compared to the chosen step size of 250 µm. The neutron collimator for this measurement was sticked together from small residual lithium rubber pieces, due to the lack of larger pieces at this time. It was designed as a square of $2 \times 2\,\mathrm{mm}^2$. As can be seen in figure 4.11 its shape is quite irregular due to the imperfect manufacturing material. For later measurement it had been replaced by a round, more regular collimator of 2 mm diameter (chapter 3.2.4).

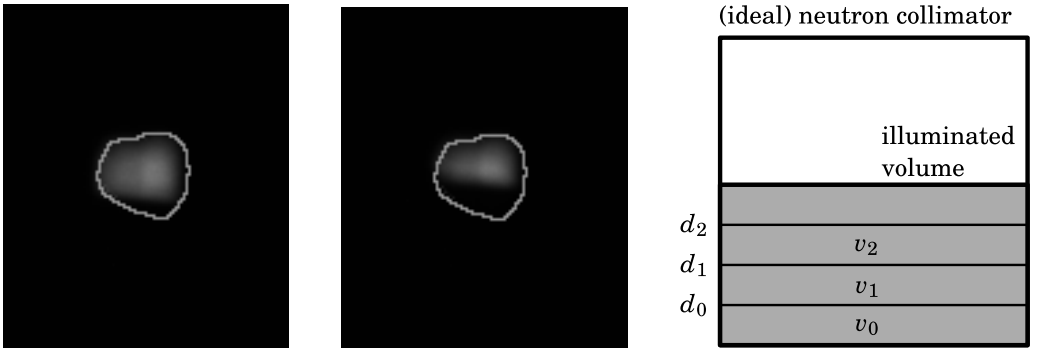

(a) Depth 01 (b) Depth 04 (c) Illuminated volume intervals for different depths

Figure 4.11.: Fine positioning of the object with the help of neutron radiographies. The neutron collimator is marked. At the lower part of the neutron collimator the irradiated material is visible.

4.3.3. Analysis and results

As mentioned above, the available measurement time was strongly limited, thus the acquisition time for each position and depth were chosen relatively short, from 10 min to maximal 45 min per depth. As a result the gained statistical resolution is not optimal. Anyway some good results could be acquired. For the determination of the elements present at each position the single depth spectra from one position were summed up to enhance the statistical resolution. From the analysis of this sum spectra it got clear that there are still chlorine residuals from the pollutions present at the laser cleaned area (fig. 4.12). This residuals could only be identified in the laser cleaned and the uncleaned areas, but not in the area cleaned with the Rochelle salts [Fes09b]. The elements copper, gold and mercury could also be measured; at the uncleaned part additionally potassium was found [Fes09b].

Due to a difficult geometry at the positions cleaned with the Rochelle salt and the uncleaned position the statistical resolution at this positions was worse than at the laser cleaned position. Unfortunately due to this limitation it was not possible to create a depth profile for this positions. For the measurements at the laser cleaned

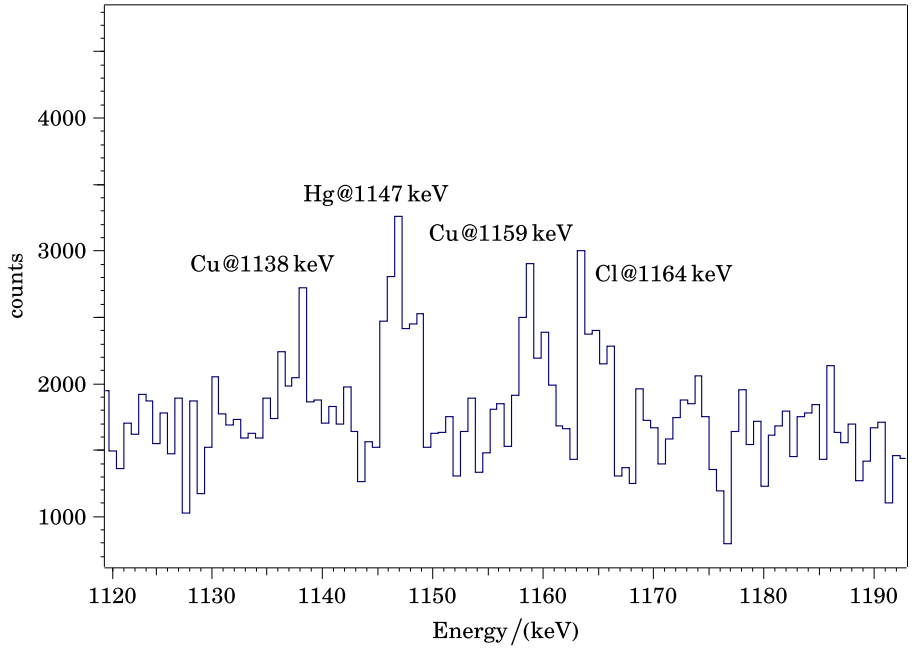

Figure 4.12.: Sum spectrum of the measurements at the laser cleaned position. (The spectrum has been re-normalized to a measurement time of 4000 s for analysis reasons.)

position a depth profile of the copper, gold and mercury intensities is shown in figure 4.13.

Neglecting self-shielding effects, which is acceptable because only a thin layer was measured, the following equation can be derived from eq. (2.24) for the density of a single element χ in the irradiated volume V_n, ranging from the surface to depth d_n:

$$\rho_\chi \propto \frac{\mathcal{N}_{\gamma,\chi}\left(d_n, E_\gamma\right)}{V_n}, \tag{4.9}$$

with the peak area $\mathcal{N}_{\gamma,\chi}\left(d_n, E_\gamma\right)$ of a selected peak of the element.

If we only want to have a measure for the elemental deposit at one depth interval, we have to subtract the peak contributions of the previous depth intervals):

$$\Delta\mathcal{N}_{\gamma,\chi}(d_n) = \mathcal{N}_{\gamma,\chi}(d_n) - \sum_{i=0}^{n-1} \Delta\mathcal{N}_{\gamma,\chi}(d_i) \tag{4.10}$$

$$= \mathcal{N}_{\gamma,\chi}(d_n) - \mathcal{N}_{\gamma,\chi}(d_{n-1}). \tag{4.11}$$

The corresponding volume of this depth interval v_n can be determined by subtracting the irradiated volumes of the previous depth intervals (see figure 4.11(c)):

$$v_n = V_n - \sum_{i=0}^{n-1} v_i = V_n - V_{n-1}. \tag{4.12}$$

For the amount of element χ in the depth interval $d_i \ldots d_{i-1}$ we get

$$\Delta\rho_\chi \propto \frac{\Delta\mathcal{N}_{\gamma,\chi}(d_n)}{v_n}. \tag{4.13}$$

Assuming a cubic shape of the irradiated volume, which should be an adequate approximation because the curavature of investigated surface was little, the volume is proportional to the irradiated front area of the sample, which can be determined by counting pixels in the radiography for the selected depth.

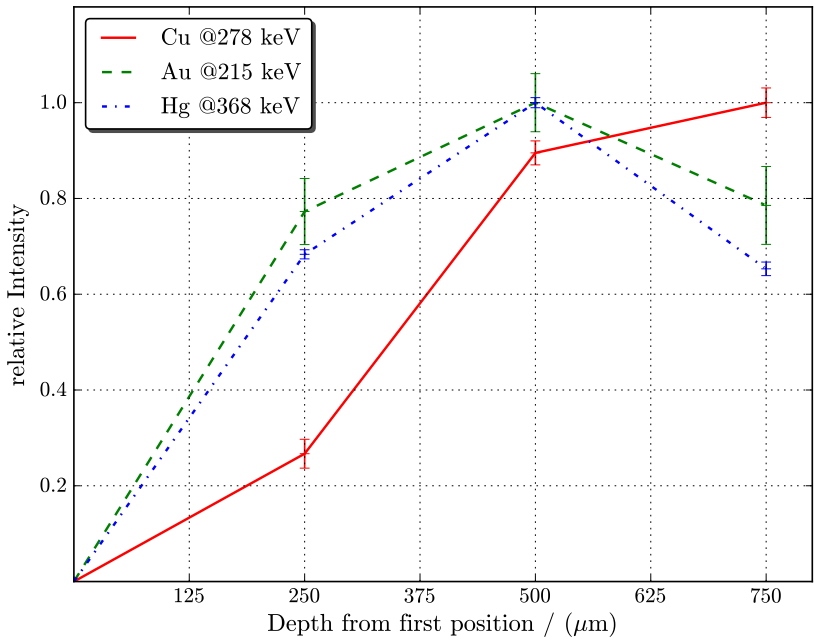

Figure 4.13.: Depth profile of elemental intensities for copper, gold and mercury for the position in the laser cleaned part of the bronze head.

In figure 4.13 the elemental intensities of copper, gold and mercury for each depth interval d_i have been plotted. Each curve for itself has been normalized to "1". The number of pixels for the estimation of the irradiated volumes have been taken from [Fes09b] (472 px for d_0, 528 px for d_1, 593 px for d_2, and 650 px for d_3). As mentioned above the first depth d_0 can not be determined as accurately as the other depths. During the measurements the positioning was done in such a way that the first depth was as close to the surface as possible, thus it seems acceptable to take it as reference "zero" depth. For each element a clearly visible peak was selected and its volume $\mathcal{N}_{\gamma,\chi}(d_n)$ was fitted for each measurement depth d_n. Normalizing the resulting values from eq. (4.13) then gives the plotted depth profiles.

One can nicely see in figure 4.13 that up to 500 µm the intensity of gold and mercury is strongly increasing and decreasing afterwards, which reproduces a thin gild-

Figure 4.14.: Proto-Corinthian ceramic vase dated to about 700–600 B.C. [Anc08]

ing layer. Mercury is a common compound of gildings from former times [Por, Sia03], so it is not surprising that the mercury intensity is following the intensity of gold. For copper we see a strong intensity increase, too, but not as strong as for gold and mercury. From 500 µm to 750 µm the copper curve only increases by ≈ 10 %, which may indicate that this depth is below the gilding layer, where we expect a quite uniform copper density.

It is important to note that the mentioned depths can not be seen to represent the absolute depth and extension of e.g. the gilding layer, but more to show the general characteristics of the elemental abundances. The thickness of the gilding layer of the analyzed head should be in the order of about 10 µm [Sia03], which is obviously far off from the values one would assume from figure 4.13. The main reason for this discrepancy is the shape of the measured sample surface, which has a slight curvature, thus influencing the measured elemental intensities. Anyhow, the intensity distribution in figure 4.13 gives a good qualitative overview of the elemental abundances in the upper surface layers.

4.4. Analysis of a proto-Corinthian vase

4.4.1. Object

An ancient Greek vase of proto-Corinthian style (fig. 4.14), provided by the *Museo delle Civiche Raccolte Archeologiche e Numismatiche* in Milan and dated to about 700–600 B.C, was brought to the PGAI/NT setup at FRM 2 for analysis. The vase is sealed with its original cap and its content was unknown, thus it was desirable to determine the composition of its content, without opening the sealed cap or damaging the vase in any other way.

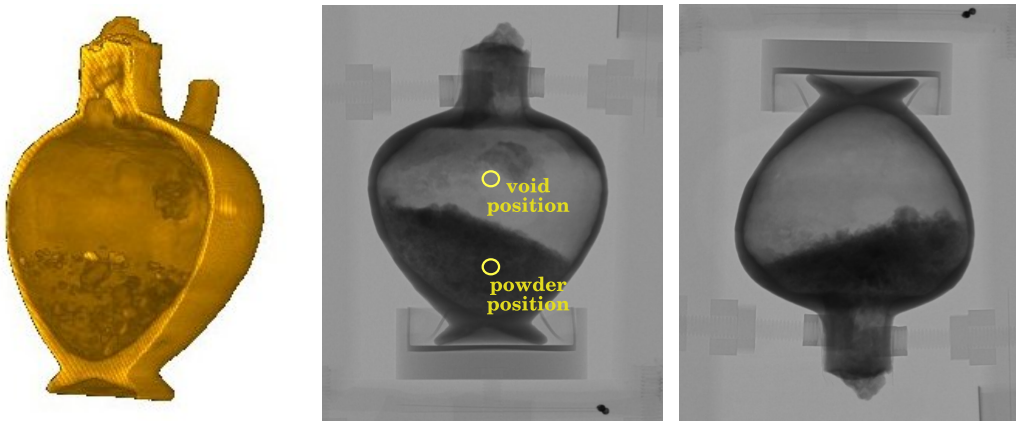

(a) Neutron Tomography reconstruction of the ceramic vase (PGAA@FRM 2)

(b) Radiography of the vase (ANTARES@FRM 2)

(c) Radiography of the vase orientated upside-down (ANTARES@FRM 2)

Figure 4.15.: NT analysis of the ceramic vase ((b) and (c) courtesy of the ANTARES neutron imaging facility at FRM 2)

4.4.2. Measurements

As first measure a neutron tomography of the vase was acquired and reconstructed at the PGAI/NT setup at FRM 2, to get a general idea about the vase's content. The reconstruction shows some grained deposit at the lower part, filling the vase to about its half (fig. 4.15(a)). Due to the grained structure of the deposit it was assumed that it consists of some kind of powder. This could be confirmed later at the neutron imaging facility ANTARES at FRM 2, where high resolution radiographies of the vase were taken (fig. 4.15(b) and (c)) and a high-resolution NT was done.

Several PGAI measurements in chord-configuration were done afterwards on the vase, at several positions on the surface, the sealing cap, and the powder but during the later analysis it turned out that unfortunately most of them were rendered useless by electrical problems of the Multi-Channel-Analyzer. The remaining good spectra originated from two distinct positions: One position lying directly inside the powder and another lying above the powder in the void space of the vase (see figure 4.15(b)). These two measurements were running for an acquisition time of 90 min, each.

4.4.3. Results and discussion

In table 4.1 the relative masses determined at the two remaining positions are listed. An exemplary section of the acquired spectra is shown in figure 4.16.

Because the background measurement, that is usually done to correct the γ-spectra for background contributions from the surrounding materials, was among the useless spectra a proper background correction could not be done. Due to some significant design changes after this measurement it was not possible to repeat this background

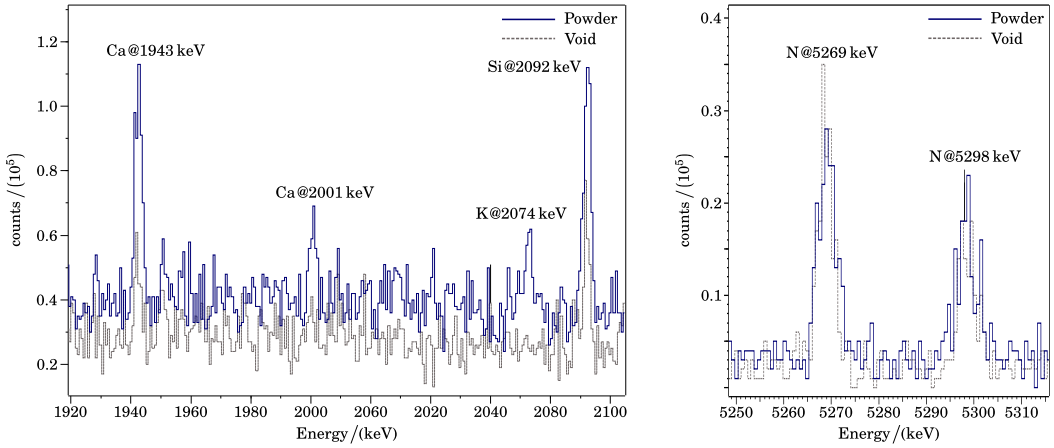

(a) Comparison of calcium, potassium and silicon peak intensities

(b) Background peaks used for normalization

Figure 4.16.: Comparison of spectra from powder and void position in vase

determination, hence it was only possible to do a rough correction by ignoring peaks that are known to be present in the background from other measurements and that have the same intensity in the spectra for both positions. Peaks that are normally present in the background, but that showed a different intensity in the spectra for the two positions are listed in table 4.1, because the different intensities are likely to originate from appearances of these elements in the sample. The values in table 4.1 are normalized to common nitrogen background peaks, that showed the same intensity at both position (fig. 4.16(b)). It has been assumed that neutron- and γ-self-shielding effects can be neglected for this sample.

The appearance of gadolinium in table 4.1 is surprising. Most probably it is caused by a contamination with small amounts of gadolinium that was used for the painting of the reference dots. Due to its very high cross-section (254000 b for the stable ^{157}Gd) for thermal neutron capture even very small amounts of gadolinium can be detected.

One sees that all (except the gadolinium contamination) elements are present at both measured positions. This may be due to three reasons:

1. The ceramic of the vase and the powder are of similar material,
2. there are some powder residual sticking a the inner surface all-over the vase, or
3. the powder is of a material that is hard to detect with PGAA, thus being “invisible”.

The last reason can be excluded, because the powder is clearly visible in the NT. Because NT also relies on capture of cold neutrons we can deduce that the neutron capture cross-section of the materials in the powder is high enough to be detectable by PGAA.

Table 4.1.: Comparison of relative masses found in void and powder position

	$m_{\text{rel.,Void}}$	$m_{\text{rel.,Powder}}$	$\frac{m_{\text{rel.,Powder}}}{m_{\text{rel.,Void}}}$
K	2.28 ± 0.60	7.6 ± 1.2	3.31 ± 0.99
Ca†	3.46 ± 0.82	12.2 ± 1.8	3.52 ± 0.94
B†	$(7.08 \pm 0.81) \cdot 10^{-3}$	$(1.23 \pm 0.14) \cdot 10^{-2}$	1.73 ± 0.29
Ti	1.32 ± 0.20	2.03 ± 0.28	1.56 ± 0.30
H†	1.96 ± 0.24	4.74 ± 0.59	2.42 ± 0.37
Mn	0.98 ± 0.38	3.32 ± 0.69	3.4 ± 1.5
Gd*	—	$(3.37 \pm 0.63) \cdot 10^{-3}$	—
Si†	75.7 ± 9.0	152 ± 19	2.02 ± 0.30
Fe†	3.90 ± 0.81	11.7 ± 1.7	3.02 ± 0.76

* Gd contribution probably from a contamination caused by the Gd used for the reference markers.

† Common elements seen in the background spectra for other measurements (see e.g. [Can10])

To get an idea which of the other two hypotheses is true, the ratios of the relative masses for the powder and void position were calculated. Elements that are part of the ceramics of the vase should have a similar abundance at both positions, while the elements that form the powder should have a higher abundance at the powder position, even if there are some powder residuals sticking at the vase surface. The calculated ratios are listed in table 4.1. One sees that especially the amounts of potassium, calcium, hydrogen, manganese and iron at the powder position are significantly higher, thus they are probably components of the powder. One assumption is that the powder is some ancient cosmetics, e.g. makeup. The found elements may be an affirmation for this theory, but this topic has to be discussed further by the archaeological researchers.

4.5. Analysis of a bronze belt point from the 7th century

The analysis of a bronze belt point (fig. 4.17(a)), provided by the *Museo delle Civiche Raccolte Archeologiche e Numismatiche* in Milan, was done with PGAI/NT at FRM 2. The point was known to be hollow and it was of archaeological interest if some kind of relic, i.e. a bone or cloth fragment, was put inside during fabrication. A high-resolution NT was done at the ANTARES neutron imaging facility at FRM 2 (see fig. 4.17(b)). The NT revealed two cavities inside the point, which seem to be empty, and some material at the base of the point. PGAI measurements were made on the material on the bottom, to confirm the composition of the material. A sensible assumption is that it is a rest of the belt's leather [Anc08]. Because the object is relatively flat the chord-geometry was chosen for the PGAI measurements.

Unfortunately, the question of the material's composition could not be solved with

(a) Bronze belt point from the 7th century [Anc08]

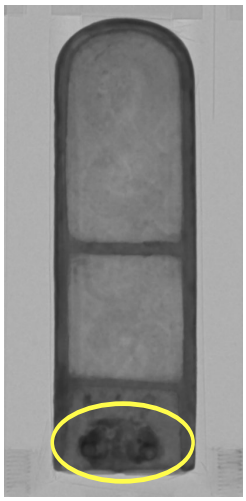

(b) Radiography of the belt point (ANTARES)

(c) Possible pollution at the back of the belt point

Figure 4.17.: Analysis of a bronze belt point ((b) courtesy of the ANTARES neutron imaging facility at FRM 2)

PGAI. Anyway, this sample is a nice example to show the limits of the PGAI method. If the material is composed of leather we would mainly expect the elements carbon, hydrogen, and oxygen. Hydrogen is a significant component in the background spectra, due to its fraction in the surrounding air. Oxygen, although of course present in the surrounding air, is rarely seen in the γ-spectra, due to its very low cross-section $\left(\sigma_0\left({}^{16}\mathrm{O}\right) = 0.00019\,\mathrm{b}\right)$, which makes its detection difficult. The cross-section of carbon is also quite low: $\sigma_0\left({}^{12}\mathrm{C}\right) = 0.0035\,\mathrm{b}$. To make thing even worse the material is surrounded by a significant amount of bronze, with its main component copper $\left(\sigma_0\left({}^{63}\mathrm{Cu}\right) = 4.5\,\mathrm{b}\right)$ showing many large peaks in the γ-spectra, thus making the recognition of other materials more difficult.

The hydrogen intensity was significantly increased at the position of the unknown material, but this does not give enough information for a reliable identification. Another element that could be detected in addition to the bronze components was chlorine, which seems to originate from an exterior pollution on the belt's back (fig 4.17(c)).

4.6. Analysis of a 7th century iron belt mount

4.6.1. Object

The iron belt mount shown in figure 4.18(a), dated to the middle third of the 7th century, was provided by the Hungarian National Museum, Budapest for analysis. The object has been excavated at an ancient cemetery in *Környe*, Hungary. It consists of one front and one back iron plate. On the front iron plate several glass, silver,

copper and brass inlays are attached for decoration.

From the archaeological point of view it was interesting to analyze the exact structure of the two iron plates and to determine if the space between the plates is void or filled with some filling material. If there is filling material between the plates its composition was of interest; it was assumed to be a calcium based or organic material [Hun08]. Furthermore the composition of the sticking material used to attach the glass and metal inlays should be measured, if possible.

4.6.2. Measurements

A PGAA measurement performed at the Budapest Research Reactor showed a high amount of iron and silver, some copper and a small amount of hydrogen in the iron belt [Kis]. The other expected elements, e.g. zinc from the brass inlays, could not be detected by PGAA, due to the sensitivity limits of the method.

The imaging measurements were later performed at FRM 2 and started with a Neutron Tomography. This tomography revealed that there is in fact some filling material between the two iron plates. It also delivered the exact structure of the plates, e.g. the shape of the holes that hold the decorating inlays (figure 4.18(d)).

With the help of the NT eight representative measurement positions for a PGAI measurement have been determined (figure 4.18(a)), which were measured for an acquisition time of 4 hours for each point. Due to the flat shape of the object again the PGAI chord-configuration has been chosen for the measurements.

4.6.3. Results

The results of the PGAI measurements are listed in table 4.18(b). Additionally to the elements found in the PGAA measurement some chlorine was detected at positions #2, #3, #5 and #6, which may be again due to some exterior pollutions. The composition of the filling material and the material used to fix the glass inlays could neither be determined with the PGAA measurement at the Budapest Research Reactor nor with the PGAI measurement at FRM 2. Probably the cross-sections of the present elements are to low to be detected.

4.7. Analysis of a disc fibula from the 6th century

4.7.1. Object

A disc fibula (fig. 4.19(a)), dated to the second half of the 6th century, was provided by the Hungarian National Museum in Budapest for extensive analysis. The fibula was excavated at an ancient cemetery in *Kölked-Feketekapu*, Hungary.

The main structure of the fibula, e.g the outer ring, appeared to be out of iron, covered by gold lined almandine[4] inlays on the front. A pearl of unknown composition

[4] Almandine, a mineral of the garnet family, has the chemical formula $Fe_3Al_2Si_3O_{12}$.

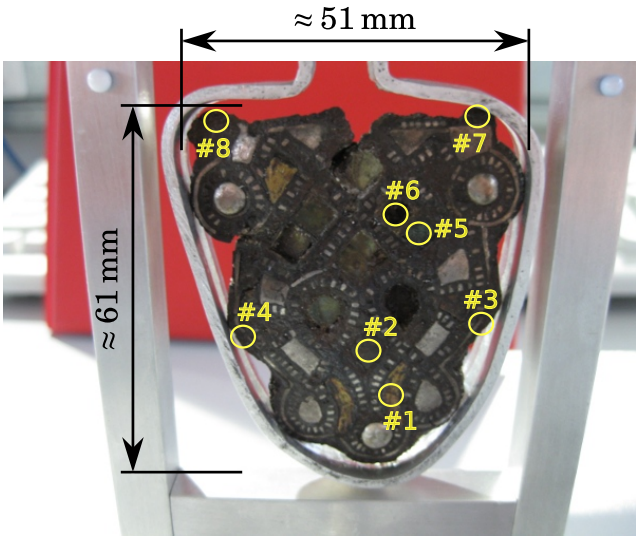

(a) Belt mount from 7th century. The PGAI measurement positions are labeled.

Position	Elements
#1	Fe, Cu, Ag
#2	Fe, Cu, Cl
#3	Fe, Ag, Cl
#4	Fe, Ag
#5	Fe, Cu, Cl
#6	Fe, Cu, Cl
#7	Fe, Ag
#8	Fe, Ag

(b) Elements found at the measured belt mount positions

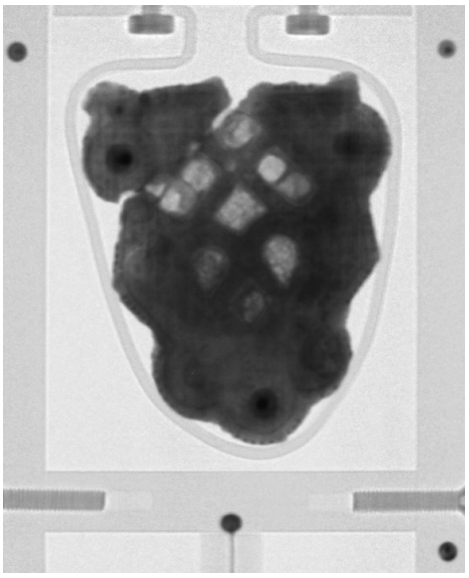

(c) Radiography of the belt mount

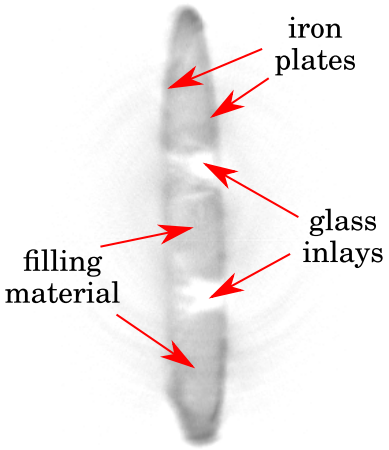

(d) Slice in the NT reconstruction

Figure 4.18.: Analysis of the *Környe* belt mount

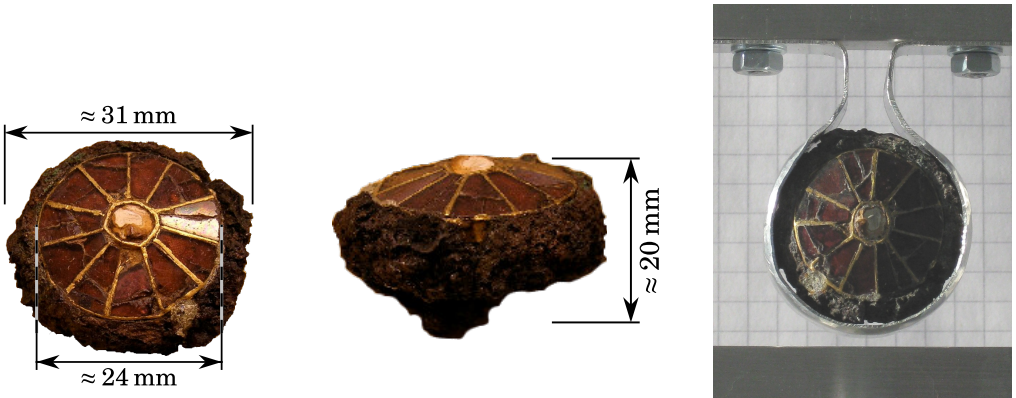

(a) Front view [Kas06a] (b) Side view [Kas06a] (c) Fibula in sample support

Figure 4.19.: Disc fibula from the second half of the 6th century

is placed on the front, enclosed by the almandine inlays. The back-plate consists of bronze [Hun08].

The iron structure is seen as quite uncommon for such an object and it is not clear if it is part of the original fibula structure or if it has been used as part of a repair [Kas06a]. An answer to this question could help to identify the original place of manufacture. It was unclear whether another metal, possibly iron, is located below the bronze back-plate. The gold lining of the almandine inlays is also quite uncommon. Usually these linings are made from silver [Hun08], thus the complete gold distribution inside the fibula was of archaeological interest. Furthermore the identification of the pearl and the filling material of the fibula were desired.

4.7.2. Measurements

The analysis of the fibula was started with a bulk PGAA measurement at the Budapest Research Reactor, to obtain an overview of the fibula's composition [Kis]. With this information the expected activation of the fibula during the further imaging analysis could be estimated. Also the knowledge of the bulk composition eases the later PGAI analysis significantly, because the time consuming elemental identification only has to be done once and not for all PGAI spectra separately. The results of this PGAA measurement are listed in table 4.2. The imaging measurements were started with a Neutron Tomography at the PGAA setup at FRM 2 to guide the further elemental mapping (fig. 4.20). The appointment of measurement positions for a 3D-PGAI scan of the fibula was then done utilizing the NT reconstruction. Due to the symmetry of the fibula it was decided to limit the scan to one quadrant and extrapolate the obtained results to the other fibula quadrants. In this quadrant three layers were scanned in steps of 2 mm × 2 mm: The first layer was placed at the position of the almandine inlays, the second layer in the middle of the fibula and the third layer at the back-plate

Table 4.2.: Detected elements from a bulk PGAA measurement on the *Kölked* disc fibula [Kis]

Element	relative mass (normalized to 100 %)
Fe	64.5 %
S	15.3 %
Au	7.9 %
Cu	7.2 %
H	2.2 %
Al	1.2 %
Ag	0.9 %
Mn	0.7 %
Cl	0.1 %

of the fibula (see figure 4.21(a)). In the first layer the full part of the quadrant that is covered by the almandine inlays was scanned with highest precision (fig. 4.21(b)) while for the other layers a coarser grid was configured (fig. 4.21(c) and (d)) to save measurement time.

From the NT it got clear that these parts are relatively homogeneous, thus the information gained through a finer measurement grid would probably not justify the much longer measurement time. Overall 30 positions in the first (front) layer, 27 positions in the second (middle) layer, and 20 positions in the third (back) layer were measured for an acquisition time of 180 min, each, resulting in a full measurement time of about 10 days for all 77 positions. The fibula was orientated under an angle of 45° with respect to the beam during the measurements, to minimize self-shielding and self-absorption effects.

4.7.3. Results

For the elemental mapping of the fibula the analysis was restricted to one or maximal up to three peaks in the same energy region per element. Because the spatial resolution of the γ-collimator is energy dependent (see chapter 3.2.3) the mixture of peak intensities from very different energy regions may disturb the spatial mapping. When possible lower energetic peaks were preferred during the analysis, because of the better γ-collimator resolution for these energies. The detector efficiency is also decreasing for higher energetic γ-rays, which lowers the already low count-rates for PGAI measurements even more. Unfortunately at lower peak energies the general γ-ray background is increased and the general peak density is higher, which results in a higher likelihood of mutual peak interferences in the spectra. Both factors may hamper exact peak fitting. The peaks that were finally used for the analysis were selected with these considerations in mind. The mapped elemental distributions are shown on pages 75 – 82. All given intensity numbers are given in relative masses.

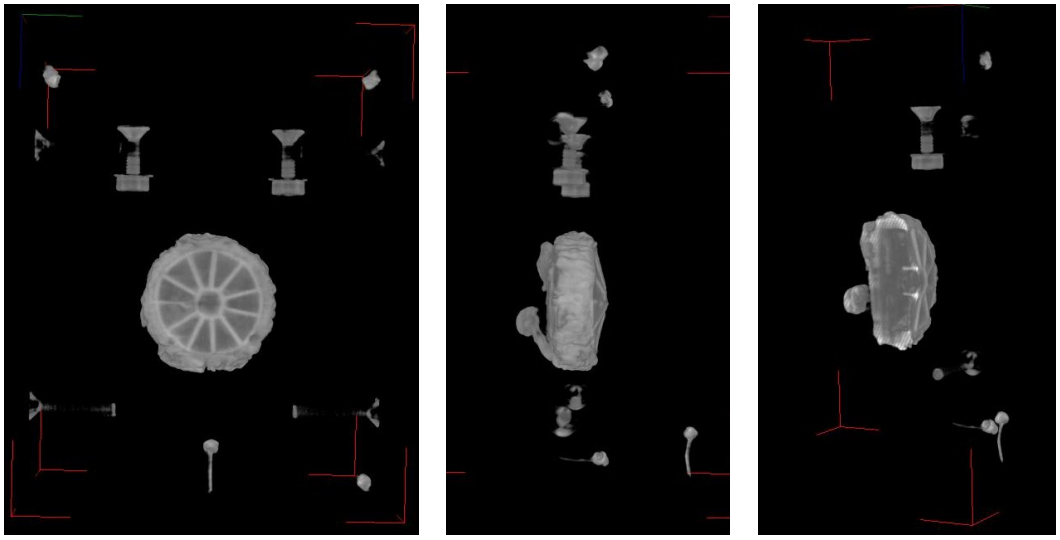

(a) Front view (b) Side view (c) Cut into disc fibula

Figure 4.20.: NT reconstruction of the *Kölked* disc fibula

Iron

The iron distribution map is shown in figure 4.22. Iron was detected all-over the fibula with relatively high intensities. The highest intensities are visible on the outer ring and the back-plate, but the mapped iron densities are unexpectedly high in the inner part. This may be due to the limited spatial resolution of the γ-collimator, compared with the resolution of the neutron-collimator. Due to the selected measurement orientation of 45°, and the high amount of iron in the outer ring and the back-plate of the fibula, it is likely that for most measurement positions high amounts of iron were lying close to the isocenter and have been irradiated by the collimated neutron beam. To minimize this effect, instead of the strongest iron peaks at 7631 keV and 7645 keV,

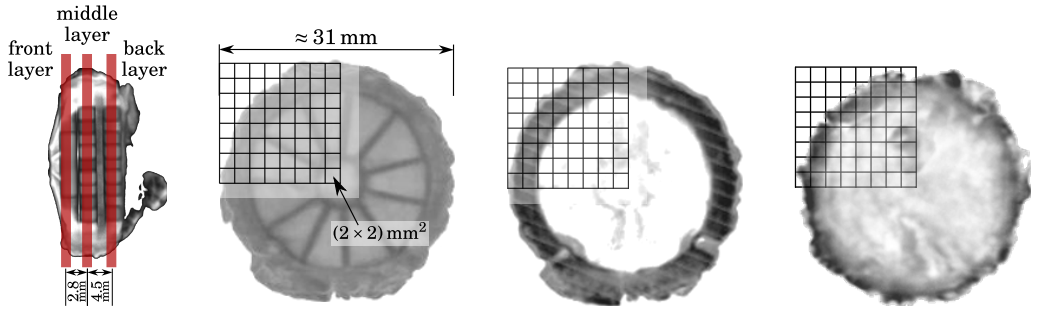

(a) Layers (b) Positions in front layer (c) Positions in middle layer (d) Positions in back layer

Figure 4.21.: PGAI measurement positions in the *Kölked* disc fibula

the lower energetic peak at 352 keV has been used for the iron mapping, which should show a better spatial resolution.

Sulfur

Sulfur is mainly found in the inner part of the fibula (fig. 4.23), thus it is probably a component of the filling material. The non-uniform sulfur distribution in the back layer which can be observed in figure 4.23(g) may be due to some irregularities in the back-plate structure.

Gold

The highest gold intensities are seen on the front, the ring, and the back-plate (see figure 4.24). The low gold intensity in the inner part can be explained by the influence of the high intensities in the neighboring volumes. The gold distribution in the front layer was expected from the lining of the almandine inlay. From the mapped gold intensities in the front layer the position of the gold linings can be sensed (fig. 4.24(f)). The high gold intensity at the ring in the middle layer is probably partly influenced by the outer gold lining in the front layer, but it is too high to be explained solely by that. The intensity in the back layer is higher than in the middle layer, so it is not caused by the gold in the front layer. Maybe the high gold intensities in the middle and back layer are due to a former gilding of the fibula.

Copper

Copper is nearly exclusively visible in the back layer (fig. 4.25), which was expected due to the back-plate, which is manufactured from bronze. The few copper occurrences in the middle layer may be due to some extensions of the back plate into the outer iron ring, maybe to clamp or fix these two parts. The single copper abundance in the front layer is not so easy to explain. It may be a component of the pearl, but in this case the neighboring positions that cover the pearl should show some copper, too. In figure 4.19(c) one can see a small “blister” at the lining of the pearl of unexplained origin, which is exactly at the position of the observer copper abundance. Maybe this “blister” is the origin of the unexpected copper abundance.

Hydrogen

The hydrogen distribution is shown in figure 4.26. It can be seen that hydrogen is distributed quite homogeneously in the front and middle layer, while for the back layer the intensity is significantly less at the outer upper part. Hydrogen seems to be another component of the filling material.

Aluminum

The aluminum mapping is shown in figure 4.26. Aluminum is part of the almandine inlays on the front of the fibula, thus we see a relatively high intensity there. In the middle and back layer the sample holder (fig. 4.19(c)) is clearly visible on the outer ring part. Because this contribution is by far the highest (see figure 4.27(a) and (b)) the scale of the layer distributions has been adjusted for better differentiation of lower aluminum intensities in figure 4.26(e), (f) and (g). Aluminum is visible in the inner part of the fibula, although it is only expected at the positions of the almandine inlays.

The main reason for this mapped abundance is probably the same as explained above for the iron distribution, but for the shown aluminum map an additional explanation can be given: The strongest peak following the neutron capture of the stable ^{27}Al is a decay peak originating from the β^--decay of the formed ^{28}Al with a half-life of 2.25 min. The intensest prompt γ-peak is about four times less intense and lies with $E_\gamma = 7724$ keV in an energy region where the detection efficiency of the γ-detector is rather low. Following peak intensities are again significantly lower. Due to the low statistics of PGAI measurements in general the less intense prompt γ-peaks showed to be quite inappropriate for the mapping of aluminum in this case. Compared to the acquisition time of 3 hours per measurements point the half-life of the 1779 keV decay peak is quite short and thus its influence on succeeding measurements points should be rather low, so it has been used for the aluminum mapping. Anyway it may give a small contribution to the following measurement positions due to the lasting decay, which is a further explanation for the small aluminum intensities seen at the measurement positions inside the fibula.

Silver

Silver is only seen in the front and middle layer (fig. 4.28) and its highest intensities follow the lines of the inlays linings. Hence, it can be assumed that the linings of the almandine inlays are not solely out of gold, but consist of gilded silver. As mentioned above silver linings were much more common for fibulas of this kind. The high silver intensities in the middle layer follow the outer lining ring of the inlays, either because this ring is reaching a bit into the inner part of the fibula, or again due to the influence of the high silver intensities of the lining ring in the front layer.

Manganese

Unfortunately, the manganese distribution could not be mapped with the PGAI measurement, because the strongest manganese peak at 847 keV is originating from the long-lasting β-decay of the produced ^{56}Mn ($T_{1/2} = 2.58$ h) and is thus unsuitable for PGA Imaging. The intensest prompt peak is about four times less intense and could not be detected in the PGAI spectra.

Chlorine

Chlorine is only seen at some distinct positions in the fibula (fig. 4.29) at the outer parts (back-plate and outer ring). Probably this chlorine abundances are due to some external pollutions. If this is the case, the extrapolation of the chlorine distribution from the measured fibula quadrant to the rest of the fibula is questionable. Anyway, it has been done in figures 4.29(a), (b) and (c) for reasons of consistency.

4.7.4. Discussion

From the archaeological point of view the questions after the full gold distribution and the abundance of a possible other metal beyond the back-plate could be answered. Also some components of the filling material, namely sulfur and hydrogen, could be reliably identified. Iron and aluminum may be components of the filling material,

too, but this is questionable due to the high intensities induced by the outer fibula material and the sample holder. The almandine inlay linings were confirmed to be made from silver and gold.

Still unknown is the composition of the pearl in the middle of the fibula. The detected copper intensity at the pearl's position is unlikely to originate from the pearl. Probably the pearl's components are low-cross-section elements, which are difficult to detect with Prompt Gamma-ray Activation. The pearl is also nearly invisible in the NT reconstruction, which is another indication for this assumption.

Real mollusk pearls consist a high amount of calcium carbonate. For the stable ^{40}Ca, which has a cross-section for the production of the strongest prompt γ-peak at $E_\gamma = 1943\,\text{keV}$ of $\sigma_{n,\gamma} = 0.348\,\text{b}$, and an abundance of 97 % among the the stable Ca isotopes, we expect a similar detection efficiency as for e.g. the stable ^{32}S (abundance of 95 %, strongest peak at $E_\gamma = 841\,\text{keV}$, $\sigma_{n,\gamma} = 0.352\,\text{b}$), thus we can assume that it would have been detected if it had been a major component of the pearl. Another assumption was that the pearl is a replica out of glass. Glasses may contain multiple different components, but many glass types contain silicon dioxide as major component. The detection efficiency for silicon is lower than for e.g. sulfur. For the strongest prompt γ-peak of ^{28}Si at $E_\gamma = 3539\,\text{keV}$ the production cross-section is only $\sigma_{n,\gamma} = 0.118\,\text{b}$. To make things worse, silicon is a component of the γ-ray background at the PGAI setup at FRM 2, thus small silicon intensities can be easily covered, even with a proper background correction. Hence, we cannot exclude that the pearl is a replica out of glass.

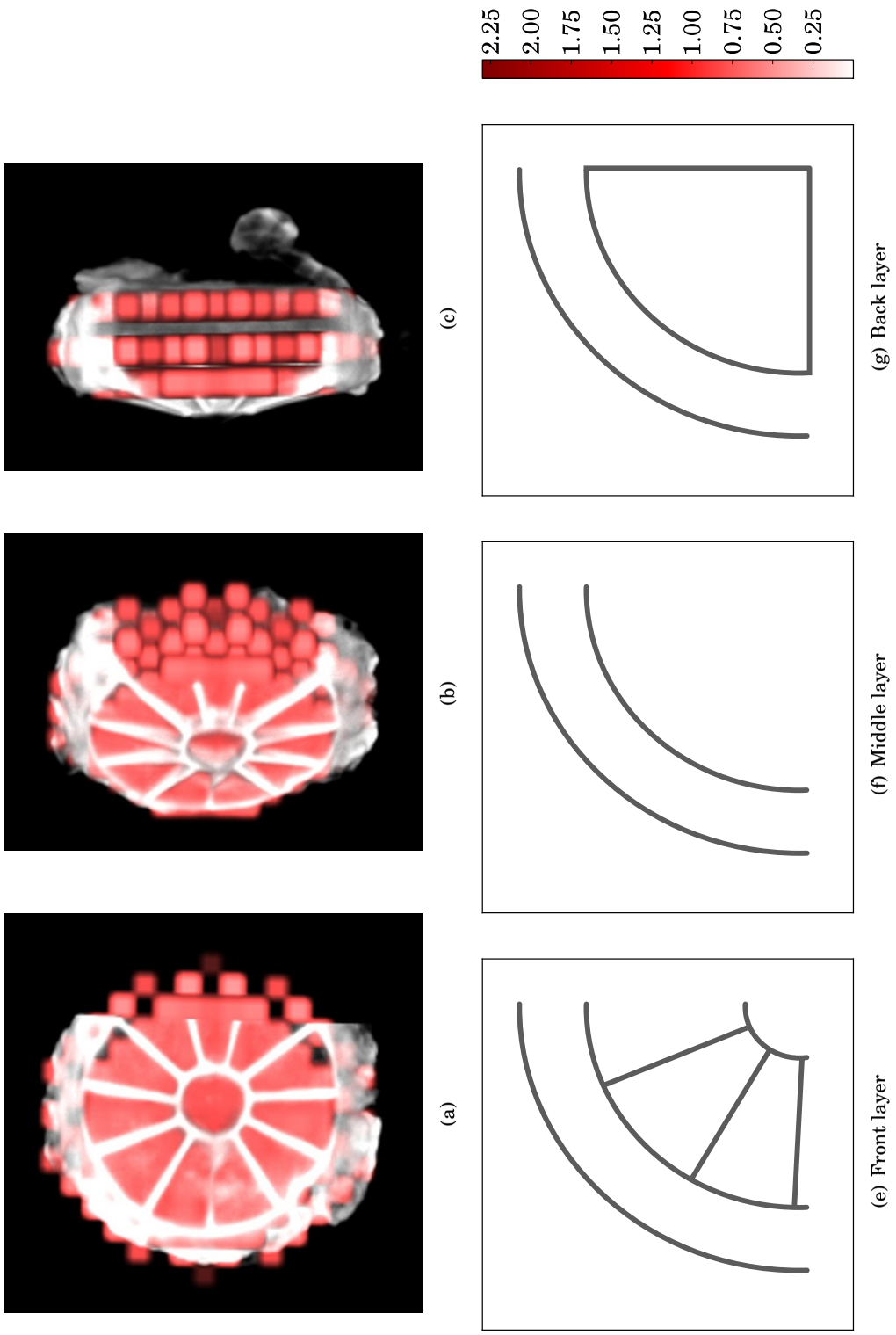

Figure 4.22.: Iron distribution in the *Kölked* disc fibula

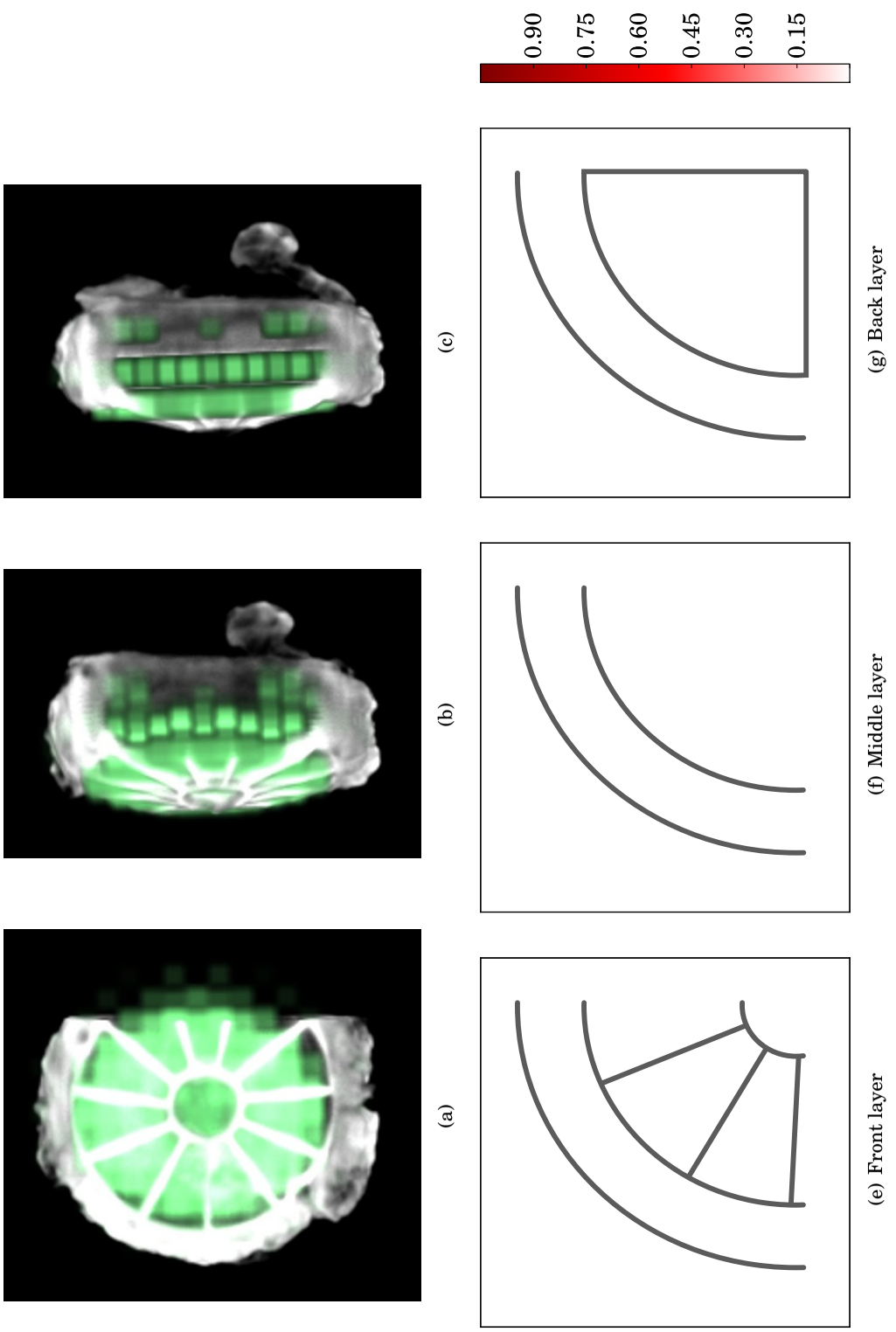

Figure 4.23.: Sulfur distribution in the *Kölked* disc fibula

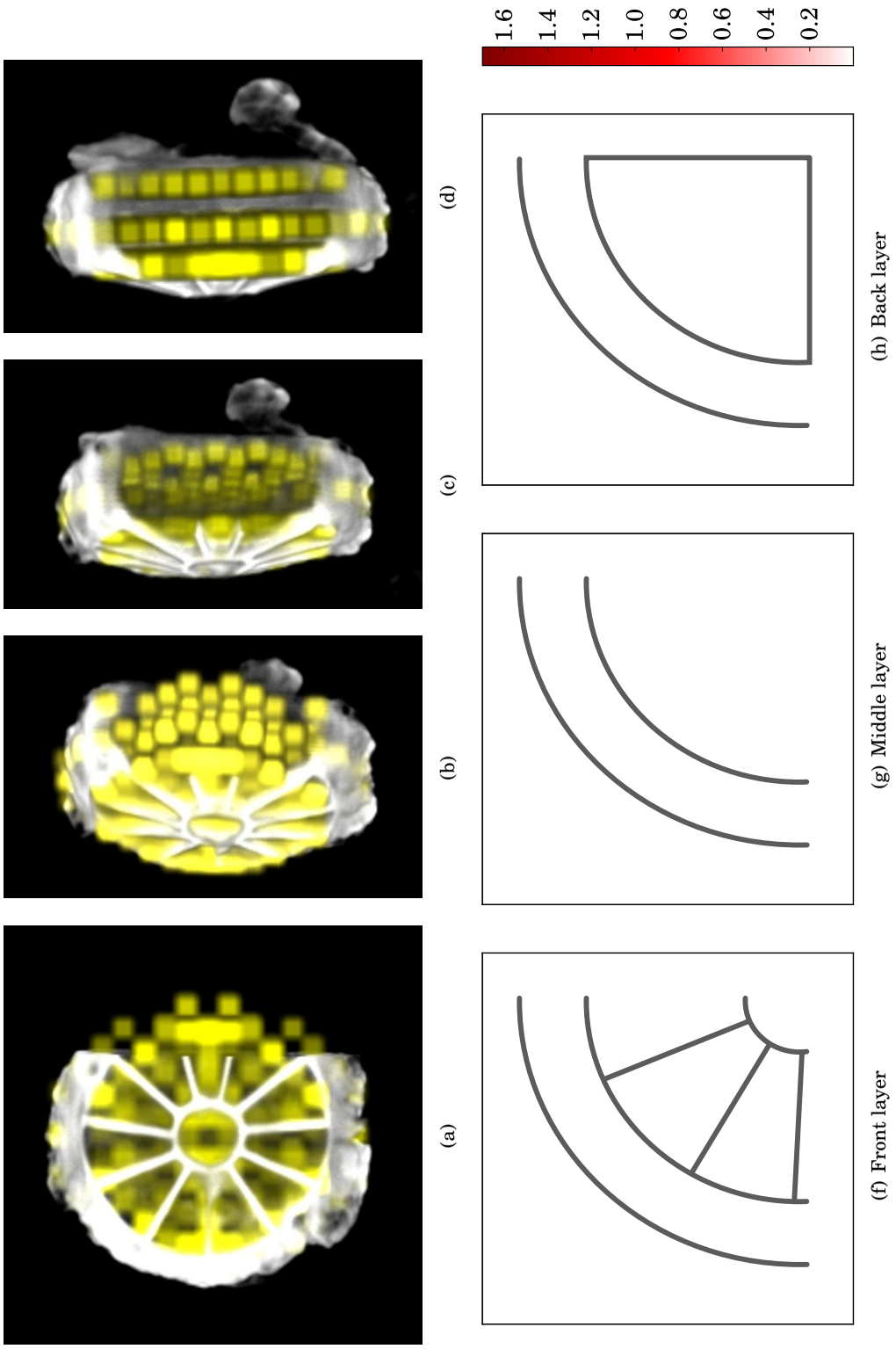

Figure 4.24.: Gold distribution in the *Kölked* disc fibula

Figure 4.25.: Copper distribution in the *Kölked* disc fibula

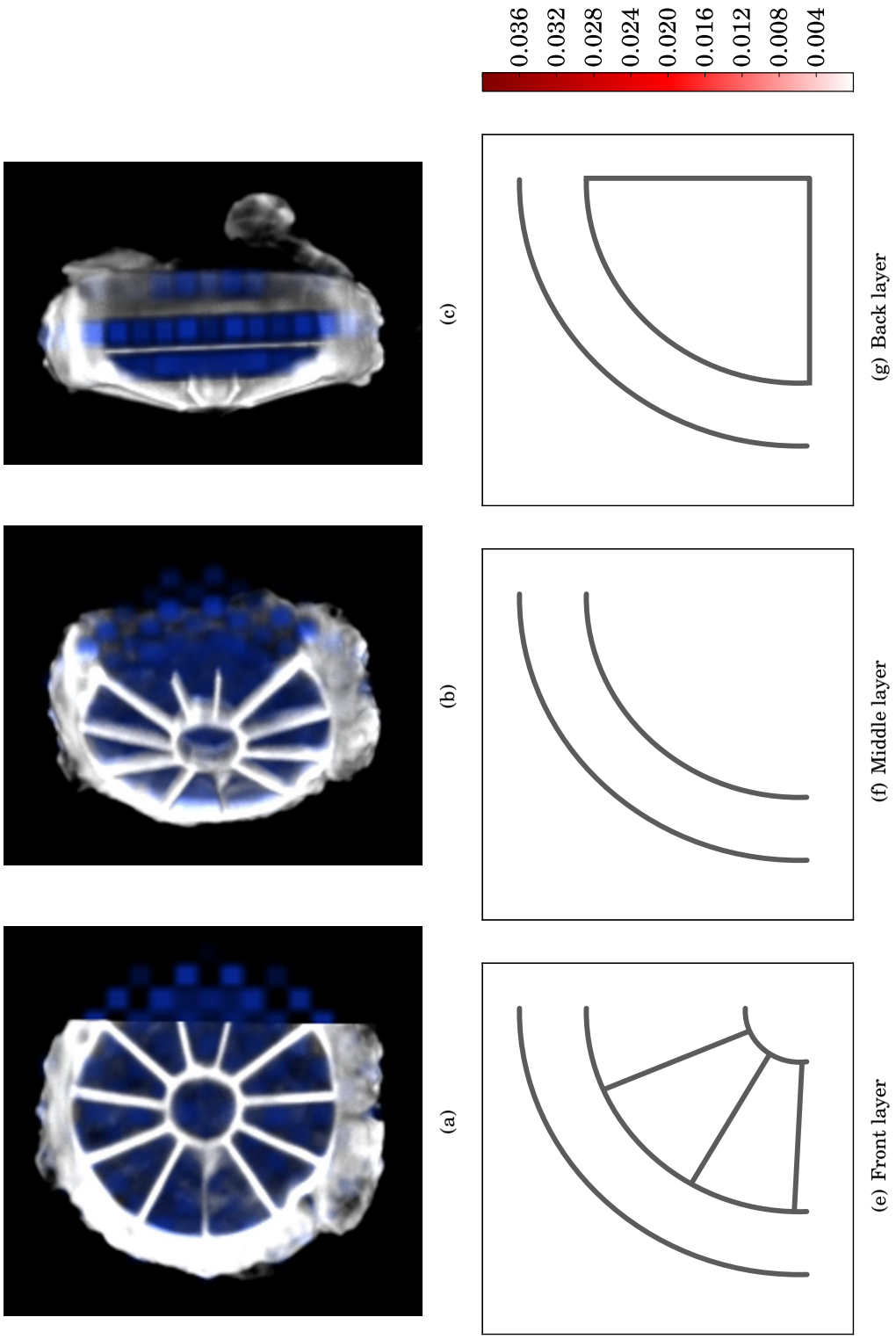

Figure 4.26.: Hydrogen distribution in the *Kölked* disc fibula

Figure 4.27.: Aluminum distribution in the *Kölked* disc fibula

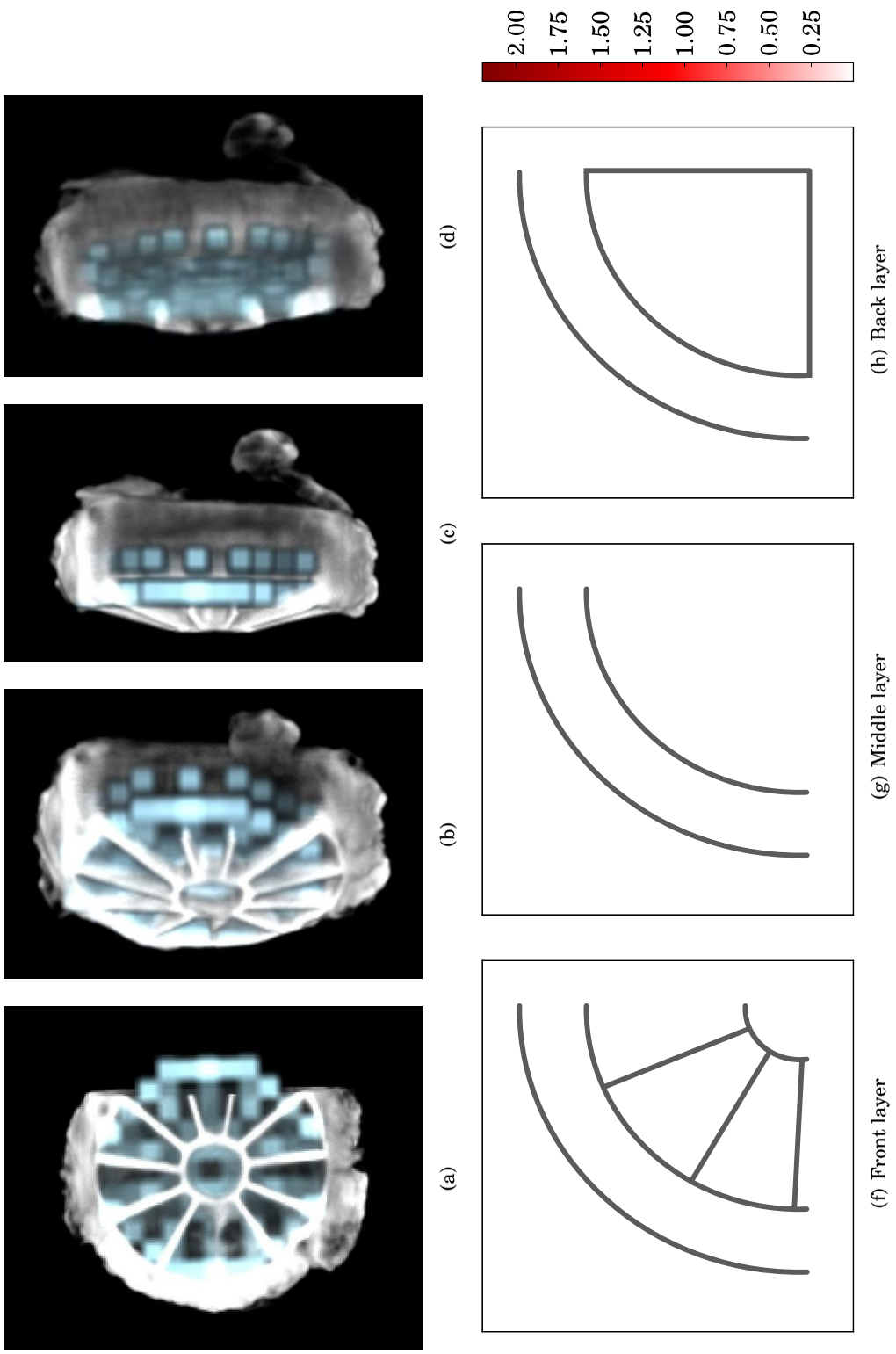

Figure 4.28.: Silver distribution in the *Kölked* disc fibula

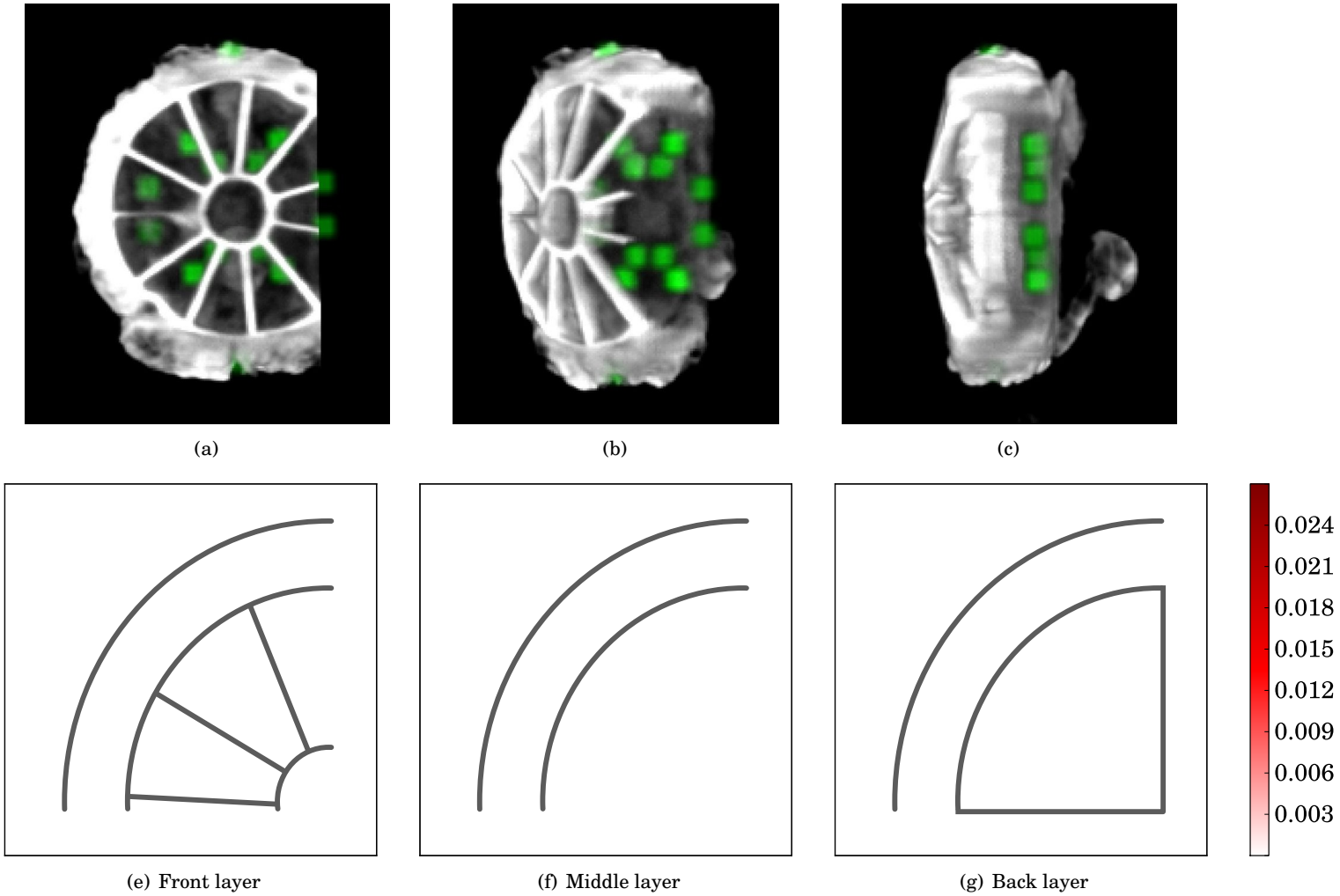

Figure 4.29.: Chlorine distribution in the *Kölked* disc fibula

5. Conclusions and outlook

The presented work showed the development of the well-established PGAA method into the new elemental imaging method PGAI/NT and introduced the new PGAI/NT configuration of the PGAA setup at FRM 2. Practical considerations, like setup alignment and data-set registration, have been covered as well as a suggestion how to correct for neutron self-shielding inside the sample. The use of PGAI as surface method is, to our knowledge, a complete new application of the PGA principle and may be a supplement to other X-ray or proton based surface methods, for depths of a few hundred micro-meter. Surface PGAI can deliver qualitative depth profiles of the elements in the surface layers of a sample as has been shown in chapter 4.3, but it is strongly dependent on the sample geometry, thus not always applicable.

Several methods on objects of cultural heritage interest have been shown with the use of PGAI as 2D- and 3D-method, which generated partly new information for the archaeological investigations of the samples or confirmed existing assumptions. Especially the full 3D-mapping of the elemental abundances in the disc fibula sample in chapter 4.7 is, to our knowledge, the first measurement of this kind and shows the potential of the 3D-PGAI method.

Despite the promising results for this method the major drawbacks for PGA Imaging became clear in the analysis. The most severe problem is the strongly reduced statistics compared to bulk PGAA due to the heavily collimated neutron beam and γ-detector. Obviously this leads to much longer measurement times, but, because the γ-ray background is not reduced in the same amount as the usable γ-ray count-rate, also to a lowered detection sensitivity. On the other hand for elements that are only present at a few distinct positions in the sample it may be possible to detect abundances that are covered in bulk PGAA measurements with PGAI. This was e.g. the case in chapter 4.6, where the chlorine abundances at some inlay positions were not detected with the previous PGAA measurement.

To address the problem of low γ-ray count-rates and the resulting long measurement times, two approaches are currently in preparation at the PGAA setup at FRM 2. The first approach is the optimization of the available neutron flux at isovolume position. The use of the elliptical "nose" of the PGAA is expected to increase the available flux by a factor of about $2-2.5$ (see chapter 3.1), but the problems of the resulting very divergent neutron beam are not so easy to solve. The focal point of the neutron beam has to be determined exactly and the position of the γ-collimator has then to be adjusted accordingly. The rectangular shape of the γ-collimator may be inappropriate for the resulting beam, because the high divergency may cause irradiation of sample volumes above and below the ideal isovolume and hence strongly decrease the spatial resolution in z-direction. If this decrease shows to be to high to be ac-

ceptable, the height of the γ-collimator will have to be reduced, which may eliminate the count-rate gain achieved through the elliptical "nose". If we assume that in this case the γ-collimator has to be changed to a symmetric shape of a circle with 3 mm diameter, the collimator area will be reduced by a factor of about 3.8 compared to the (3×9) mm^2 collimator used so far. The final design and positioning will be a task of extensive and careful optimizations.

The second approach is even more challenging and should be pursued in two steps. In the first step multiple positions in the sample should be measured simultaneously by using a position sensitive γ-ray detector [Mat06] with a laminated γ-collimator and a collimated neutron pencil beam. This way elemental abundances along the irradiated line in the sample may be measured with significantly (depending on the sample size and the dimensions of the laminated collimator) less steps. In the second step then the position sensitive γ-detector should be sectioned into a grid over its full height and width with two laminated γ-collimators that are rotated to each other by 90°. Together with an open neutron beam the two-dimensional elemental abundances over the area covered by the grid can be measured in, in the optimal case, four measurements, by shifting the sample in height and along the neutron beam. This alone does not give a 3D-distribution, because due to the open neutron beam the measured abundances are a projection of the abundances along the full sample width. To obtain a 3D-distribution from these projections one then may use the tomography principle (chapter 2.2), by rotating the sample in front of the γ-detector. Because the tomographic method relies on quantitative information for reconstruction the effects of neutron self-shielding and γ-ray self-absorption will probably have a significant influence here. Again a high beam-divergency will complicate these measurements, so it may be advisable to start with a lower neutron flux, but better defined pencil beam, as it has been done during this work.

For all proposed methods an improvement of limited spatial resolution of the γ-collimator compared to the neutron-collimator is desirable. A simple reduction of the collimator's area is counterproductive, because this will strongly decrease the count-rates, as mentioned above. A better approach is probably to extend the γ-collimator, to better shield against off-axis high-energetic γ-rays. This may be especially difficult for the tomographic approach with the two rotated laminated collimators.

Conclusively it can be said that PGAI in its current state is already a useful method for selected samples and will hopefully be enhanced to a more efficient elemental imaging method for the regular measurement of samples from various fields of research.

A. Appendix

A.1. Nessas NT

For the calculation of the present neutron flux at each PGAI measurement position inside samples (chapter 4.2) the program NESSAS NT[1] [Sch10] has been written. The program takes the reconstruction slices obtained by a NT measurement of the analysed objects and converts the gray-value sums along the neutron flight path into cold neutron attenuation factors. A linear relationship between these two figures is taken for the conversion with adjustable slope and offset parameters (listing A.1). From the initially given neutron flux (option "`--nflux`") it then subtracts at each position the number of neutron that were attenuated so far. The calculations may be done for a uniform neutron flux or for an inhomogeneous flux as it is present in a real neutron beam. For the latter case the program option "`--flatfield`" has to be used to specify a flat-field, or open beam image of the used neutron beam. The given neutron flux than is taken as the maximal flux present in the flat-field image, given by the highest gray-value. Additionally the slice number of the reconstruction slice has to be given in this case, which should correspond to the height in the flat-field image given in pixels.

A rather important parameter is the gray-value threshold (option `--threshold`), which describes the minimal gray-value in the reconstruction to be used for the calculation. This is useful to minimize distortion due to reconstruction noise. If this threshold is chosen to low, the overall attenuation may be calculated to high, because reconstruction artifacts are included in the calculations. Too high values of course will have the opposite effect, because real values will be ignored then.

Other program options are "`--percent`", which will calculate the resulting neutron fluxed in percentages of the initial maximal neutron flux, and "`--radiography`", which can be used to create a simulated radiography with the calculated neutron fluxes at scintillator position. For the creation of such a simulated radiography the program has to be called multiple times for all slices of the reconstruction with the same output radiography filename.

For the determination of the slope and offset parameters of the conversion function the helper utility NESSAS_CAL has been written, which can be used to calculate the pairs "gray-value-sum"↔"overall neutron attenuation" for all pixels in a radiography from a flat-field image, a sample radiography and the reconstruction slices. These data pairs may then be fitted with standard fitting programs (see e.g. figure 4.5 in chapter 4.2).

[1] **N**eutron **S**elf **S**hielding correction in **A**rchaeological **S**amples via **N**eutron **T**omography

```
0
   #ifndef PARAMETER_H
   #define PARAMETER_H
   /* Configurable parameter */

5  /* Parameters for the conversion from gray-value in
    * reconstructed slice to neutron attenuation
   */

   /* Grey values in reconstruction slices will be divided by
10  * this factor for easier calculations
    */
   #define SLICE_GREY_MAGNITUDE    1.e6

   /* Default noise threshold in reconstruction slice below
15  * which gray-values will be ignored
    */
   #define SLICE_NOISE_THRESHOLD   8500.

   /* Slope of gray-value<->neutron attenuation function */
20 #define SLICE_GREY_2_NATTEN_A 0.528607/SLICE_GREY_MAGNITUDE

   /* Offset of "gray-value"<-> "neutron attenuation" function.
    * Should be close to zero, or threshold is probably wrong.
    */
25 #define SLICE_GREY_2_NATTEN_B -0.0171937

   /* Width and height of radiographies */
   #define RADIO_WIDTH     590
   #define RADIO_HEIGHT    750
30 #endif
```

Figure A.1.: Source code file “parameter.h” for the definition of some standard calculation parameters

A.2. PacSy hardware control libraries

A.2.1. Multi-Channel-Analyzer control

Hardware

For the acquisition of the γ-spectra a Multi-Channel-Analyzer (MCA), which was developed by the electronics workshop of the Institute of Nuclear Physics, Cologne, was used. This MCA features [Pas]:

- Two independent ADC channels with separate gates,
- selectable number of spectrum bins: 2k, 4k, 8k, 16k,
- differential non-linearity of $\leq 1\,\%$,
- integral non-linearity of $\leq 0.01\,\%$,
- dead-time of $1.6 \ldots 6.4\,\mu s$,
- parallel and USB interface [Bra08] .

libcomca

For the communication with the Cologne MCA at least two different software packages existed. Unfortunately, both software packages did not feature the desired network interface for MCA control, thus it was decided to write a new driver library (libCoMCA – lib **Co**logne **M**ulti-**C**hannel-**A**nalyzer) for the control and configuration of the MCA. Because the MCA control code is now moved to a generic library instead of living in a single program it is now easily possible to include control code for the Cologne MCA into existing or newly developed programs, e.g. the new spectrum analysis program HDTV [Bra10].

libcomca supports the USB interface of the MCAs as well as the parallel port interfaces and allows full configuration and control of the MCA. Advantages over the existing solutions for the control of the Cologne MCA are:

- Easy inclusion in own software projects.
- Support for the simultaneous control of multiple MCAs.
- Bindings for the C and Python programming language.

A basic program to start a timed acquisition utilizing libcomca is shown in A.2.

A.2.2. Sample table control

Hardware

For the PGAA and PGAI/NT setup two different sample positioning systems are used. For the PGAI/NT measurements, where sample movements in (x, y, z, ω)-directions

```c
#include <stdio.h>
#include <stdlib.h>
#include <string.h>
#include <unistd.h>
#include <comca.h>

FILE *specfile;

int main(void) {

  ComcaDev *mca;
  ComcaSpectrum spectrum[16384];
  int i;
  double time = 0.0;
  specfile = fopen("spectrum.dat", "w+");

  comca_init(&mca, comca_usb_pp); /* Init MCA */
  comca_open(mca, NULL); /* Open MCA */
  comca_set_num_bins(mca, 0, 16384); /* 16k spec */
  comca_start_acq(mca, 0); /* Start acquisition */

  while(time < 10.) { /* Wait for live time of 10s */
    time = comca_get_live_time(mca, 0);
    sleep(1);
  }

  comca_stop_acq(mca, 0);
  comca_read_spec(mca, 0, spectrum);

  for(i = 0; i < 16384; i++) { /* Write spectrum */
    fprintf(specfile, "%d\t␣%ld\n",
    i, (long int)spectrum[i]);
  }

  fclose(specfile);
  comca_close(mca);
  comca_deinit(&mca);
}
```

Figure A.2.: Simple example C-program to collect a 16k spectrum for 10 seconds with channel 0 of the Cologne MCA utilizing libcomca (error-checking omitted for better readability).

was necessary, a positioning table from the company STANDA[2] was bought during the ANCIENT CHARM-Project [Fes09a]. The necessary code to control the positioning table was implemented in the aforementioned IGOR PRO-Software.

For PGAA measurements a movement of the sample during the measurement is not necessary, but it is desired to have the possibility to prepare several measurements in advance and then let them run unattended, e.g. during the night. A "sample ladder", with six different "windows" for sample placement is used for this task. By moving the ladder up or down the next sample can be positioned in the beam. The sample ladder is driven by a stepper motor for exact, reproducible positioning. Two reference/limit switches allow reliable position recalibration. The stepper motor and limit switches are controlled via a TMCM-301 3-axis stepper motor controller [Tri08b, Tri07], mounted on a BB-301S-baseboard for stepper motor control [Tri10, Tri06], both manufactured by the company TRINAMIC[3]. The BB-301S-baseboard is equipped with a RS485-interface for the communication with a computer. It is programmable with the **T**RINAMIC **M**otion **C**ontrol **L**anguage (TMCL) [Tri08a].

libtmcl

The **T**RINAMIC **M**otion **C**ontrol **L**anguage defines commands and the transmission protocol for the configuration and control of TRINAMIC-motor-control-modules. This includes the conversion of `ASCII`-commands and arguments to binary bit structures and checksums, and the expected replies of motor-control-modules. Because the raw programming of the motor-control-modules involves a lot of these operations, a library, called libtmcl, has been written, which handles the necessary conversion, checksumming, transmission and error checking for the programmer. Support for most of the commands defined by the TMCL specification has been implemented. The missing commands can be easily added to the library if needed, or alternatively the corresponding command codes defined in [Tri08a] may be used. The library is aware of different "dialects" of the TMC Language that are necessary to program other TRINAMIC modules.

A small example program to control a TRINAMIC TMCM-301-controller is shown in A.3

A.2.3. Beam control and safety management

Hardware

For the operation of the PGAA setup at FRM 2 several safety aspects have to be considered [Sch08]:

- It must be guaranteed that the neutron beam is never opened as long as people remain inside the PGAA measurement chamber.

[2] Standa Ltd.: http://www.standa.lt/
[3] TRINAMIC Motion Control GmbH & Co. KG: http://www.trinamic.com

```
#include <stdio.h>
#include <stdlib.h>
#include <tmcl/tmcl.h>

#define DEVICE "/dev/ttyS2"
#define ADDRESS 1
#define BANK 0

int main(int argc, char *argv[]) {

  TMCLInterface *Interface;
  TMCLMotor *Motor;
  int position;
  int current_pos;

  if(argc != 2) {
    printf("Usage: %s <position>\n", argv[0]);
    exit(1);
  }
  position = atoi(argv[1]);

  /* Initialization */
  tmcl_init_interface(&Interface, TMCL_RSXXX,
  NULL, NULL, NULL, NULL);
  tmcl_open_interface(Interface, DEVICE);
  tmcl_init_motor(&Motor, Interface, TMCM301,
  ADDRESS, BANK, TMCL_RSXXX);

  tmcl_move_to_pos_abs(Motor, position); /* Move */

  do { /* Wait until motor reaches position */
    sleep(1);
    current_pos = tmcl_get_position(Motor);
  } while(current_pos != position);

  tmcl_deinit_motor(&Motor);
  tmcl_close_interface(Interface);
  tmcl_deinit_interface(&Interface);
}
```

Figure A.3.: Simple example C-program to move a motor with a TRINAMIC TMCM-301 motor-controller with serial interface using libtmcl (error-checking omitted for better readability).

- The neutron beam has to be closed automatically when someone tries to enter the measurement chamber without closing the beam beforehand.
- A clearly noticeable warning has to be given some seconds before the beam is opened.
- A warning light has to be lit during beam operation.
- It must be easy to reach emergency buttons, which stop the beam immediately in case of unforeseen events.

For the realization of these safety aspects the programmable modular safety-system PNOZMULTI [Pil07] of the company PILZ is in common use at FRM 2. Because the PNOZMULTI-module is freely programmable with a graphical development environment from PILZ it could be adjusted to the needs at the PGAA setup at FRM 2 and could even be used for the control of some non-safety related aspect, like the beam attenuators. For the integration of this safety-system in the acquisition system it was extended by a programmable fieldbus-module, which can be accessed via the standardized MODBUS-Protocol [MO10] over a TCP/IP-Ethernet connection.

libpilz

For the remote access to the PNOZMULTI via MODBUS the open-source library libmodbus [Rai10] was used. A small wrapper library (libpilz) was written to simplify the control of the PNOZMULTI-module. Again, a small example program is shown in A.4.

A.2.4. Camera

Hardware

For the acquisition of the neutron radiographies necessary for a full NT, the digital CCD camera pco.1600 from the PCO AG was used. The camera features [PCO08]:

- A Firewire interface,
- 14 bit color-depth (grayscale),
- a Peltier cooled CCD-chip for less noise,
- an image resolution of 1600 × 1200 pixel, and
- a configurable exposure time in the range of 5 µs…49 d.

```c
#include <stdio.h>
#include <stdlib.h>
#include <pilz.h>

/* Input and output pin definitions */
#define INP_SHUTTER_OPEN  3  /* Open shutter input    */
#define INP_RC            6  /* Remote control enable */
#define INP_SHUTTER_CLOSE 4  /* Close shutter input   */
#define OUT_SHUTTER_OPEN  3  /* Shutter open output   */

int main(int argc, char **argv) {

  PILZDevice *PILZBox;

  /* Initialization */
  pilz_init(&PILZBox, "172.25.23.22");
  pilz_connect(PILZBox);

  /* Enable fieldbus control */
  pilz_set_input(PILZBox, INP_RC);
  /* Open shutter */
  pilz_push_input(PILZBox, INP_SHUTTER_OPEN);

  /* Wait 6000ms for 'open' output to become "1" */
  if(pilz_wait_output(PILZBox, OUT_SHUTTER_OPEN, 1,
                      6000) == 0) {
    printf("Shutter␣open\n");
  } else {
    printf("TIMEOUT␣waiting␣for␣shutter␣to␣open\n");
  }

  /* Disable fieldbus control */
  pilz_unset_input(PILZBox, INP_RC);

  /* Cleanup */
  pilz_disconnect(PILZBox);
  pilz_deinit(&PILZBox);
}
```

Figure A.4.: Example C-program to open the shutter at PGAA@FRM 2 utilizing libpilz (error-checking omitted for better readability).

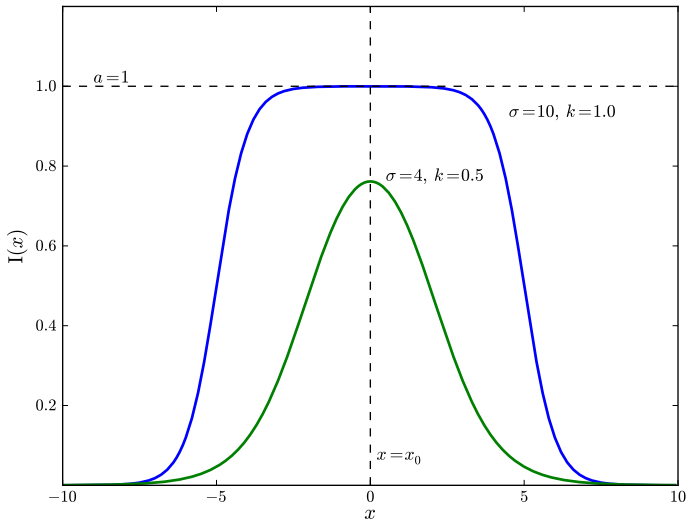

Figure A.5.: "Bump" functions for two pairs of σ and k ($x_0 = 0$, $a = 1$ and $k_1 = k_2$ for both plots)

A.3. FWHM approximation for the "bump" function

The "bump" function (fig. A.3)

$$\mathrm{I}(x) = a \cdot \left(\frac{1}{1+\exp\left(-2k_1\left(x - x_0 + \frac{\sigma}{2}\right)\right)} - \frac{1}{1+\exp\left(-2k_2\left(x - x_0 - \frac{\sigma}{2}\right)\right)} \right) \tag{A.1}$$

proved to describe the collimator responses quite well in ch. 3.2.3 and 3.2.4. Unfortunately it is analytically very difficult to obtain the import *full width at half maximum* (FWHM) parameter from this function.

As one can see in figure A.3 the maximum height of the function decreases for small values of σ and k, which means that the function does not reach the full plateau height a. For larger σ and k the function forms a quite constant plateau at height a. To have a practical approximation for the FWHM value one can make the following considerations.

If we assume, that height of the plateau a can normally be determined to an accuracy of about 5 % it is sufficient to have an approximation of the FWHM that:

$$\frac{1}{2} \cdot \mathrm{I}(x = x_0) - \mathrm{I}\left(x = \pm\frac{\mathrm{FWHM}}{2}\right) \leq 5\,\% \cdot \mathrm{I}(x = x_0). \tag{A.2}$$

It gets clear from figure A.3 and can be shown analytically that$\mathrm{I}(x = x_0)$ is the maximum value of $\mathrm{I}(x)$. Equation (A.2) says that we are happy with our approximation of the FWHM, if we have a parameter that describes the width of the function at a height, that has a deviation of less than 5 % from the maximum height.

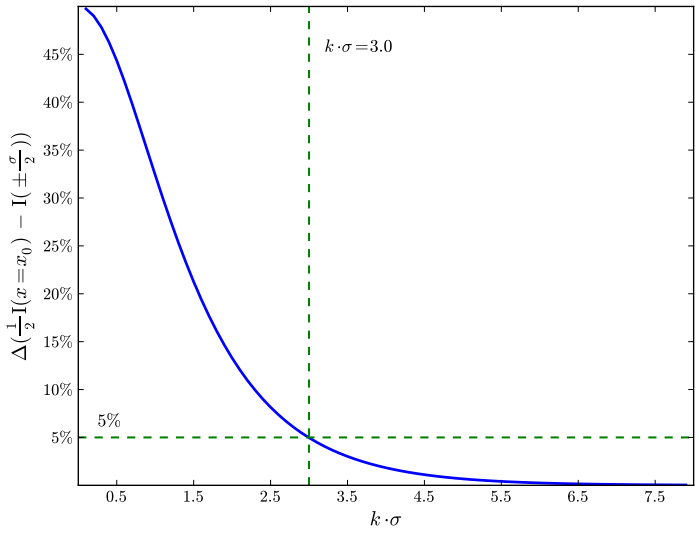

Figure A.6.: Percental deviation of half-maximum of "bump" function to its value at $\pm\frac{\sigma}{2}$

The parameter σ seems to be a natural candidate for this parameter. Looking at $x = \frac{\sigma}{2}$ (we take $x_0 := 0$ from now on, because it only changes the offset of the "bump"):

$$\overset{(A.2)}{\Rightarrow} \quad \frac{1}{2} - \frac{\mathrm{I}\left(x = \frac{\sigma}{2}\right)}{\mathrm{I}(x = x_0 = 0)} \quad \leq \quad 0.05 \tag{A.3}$$

$$\Rightarrow \quad \frac{1}{2} - \frac{\frac{1}{1+\exp(-2k_1\sigma)} - \frac{1}{2}}{\frac{1}{1+\exp(-k_1\sigma)} - \frac{1}{1+\exp(k_2\sigma)}} \quad \leq \quad 0.05 \tag{A.4}$$

For our approximation we assume $k_1 = k_2$; if an asymmetric form is desired the following considerations have to be fulfilled for both k_i. Equation (A.4) can be solved analytically. A clearer way to obtain the solution is to plot eq. (A.4). From figure A.3 we can see, that σ is a good (in the sense of eq. (A.3)) parameter for our FWHM if

$$k \cdot \sigma \gtrsim 3. \tag{A.5}$$

A.4. HDTV extensions

For the analysis of γ-ray spectra a the new software HDTV is currently under development at the Institute of Nuclear Physics of the University of Cologne [Bra10, Bra08]. HDTV is proposed as a modern successor to the currently used software TV [The94]. HDTV is based on the ROOT data analysis framework developed at CERN[4] and written in the C++ and Python programming languages. It has been designed to be easy

[4] http://root.cern.ch

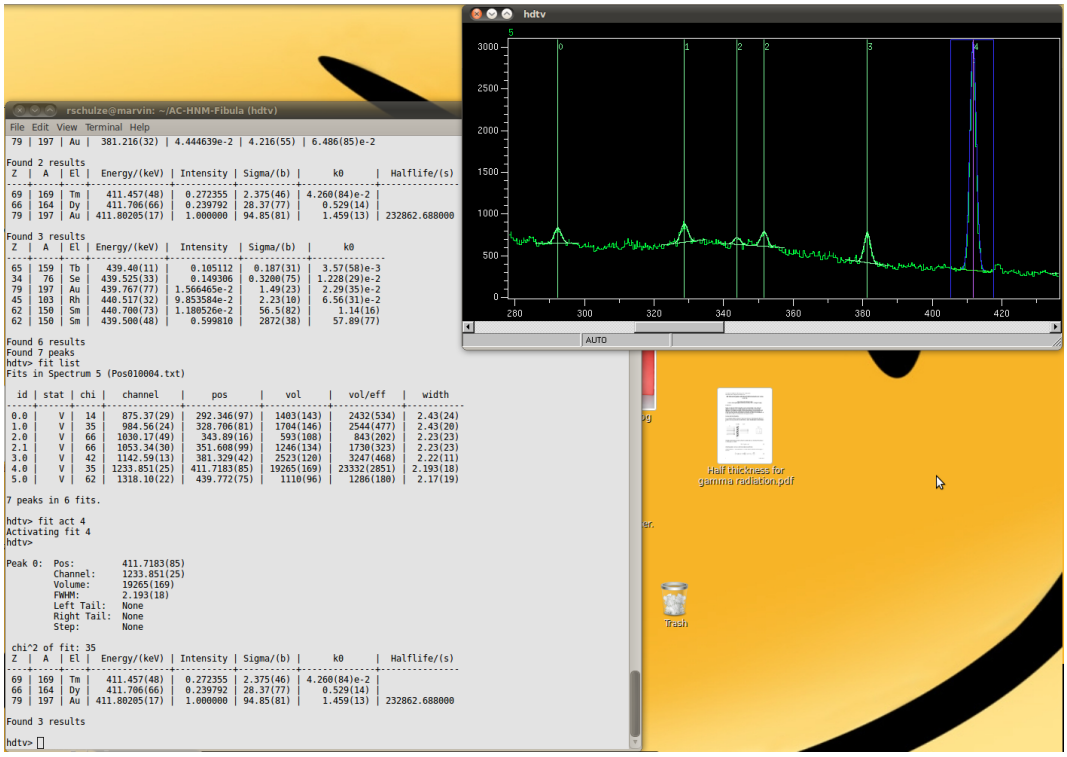

Figure A.7.: Screenshot of the HDTV spectra analysis software

extensible by Python plugins and the underlying routines can easily be used in self-written analysis programs, thus allowing a higher grade of automation. For the analysis of the measurements performed during this work HDTV was extended by e.g.

- a peakfinder for the automatic location and fitting of γ-peaks,
- functionality for the fitting and calculation of three different efficiency functions including error calculations,
- PGAA databases for the identification of prompt γ-ray peaks directly during the peak fitting, and
- the possibility to copy peak markers from one spectrum to multiple other spectra, and automatically repeat and store the fits for further analysis.

HDTV, although already usable, is currently under heavy development, which results in frequent changes of the user interface. The development is accompanied by the creation of documentation, which can be found at [Bra10].

B. Acknowledgments

The present work would not have been possible without the support of many people. Some of them should be mentioned here, not necessarily in the order of importance.

Thanks to

- ⋆ **Prof. Jan Jolie** for his supervision, the chance to participate in the ANCIENT CHARM project, and the years I was allowed to spend at the Institute for Nuclear Physics in Cologne;
- ⋆ **Petra Kudějová** for her supervision, her support and advice, and the nice working atmosphere;
- ⋆ **Lea Canella** for her extensive help during the measurements, advice and discussions, lots of memorable moments during the measurements and the Tequila afterwards, and the way we worked together;
- ⋆ **Thomas Materna** for his invaluable advice, very fruitful ideas and discussions, help in deep troubles and the always quick and helpful answers;
- ⋆ **Tamás Belgya, László Szentmiklósi and Zoltan Kis** for the pleasant and fruitful cooperation, their hospitality and everything they taught me about PGAA and PGAI;
- ⋆ **all people of the ANCIENT CHARM collaboration** for the friendly atmosphere, pleasant cooperation and all the things I was able to see and learn;
- ⋆ **Stefan Thiel and the whole fine mechanics workshop** for all the outstanding construction work, the wonderful cooperation and Stefan's enduring interest on the status of the PGAA station;
- ⋆ **Christoph Görgen, Gheorghe Pascovici and the electronics workshop** for the overall support, advice and perpetual help;
- ⋆ **Michael Pfeiffer** for a *Kölsch* at the right times, his overall support and much more;
- ⋆ **Benedikt Birkenbach** for the excellent teamwork on the computer administration and much more;
- ⋆ **Norbert Braun** for his competent advice, fruitful discussions and his work on HDTV;

⋆ **Prof. Eckart and Prof. Altland** for their willingness to judge this thesis and to chair the defense of my thesis;

⋆ **Erika Kroppen-Matenaer** for the help and cooperation during many administrational tasks,

⋆ **Prof. Peter Reiter and Tanja Kotthaus** for giving me “asylum” during the writing of my thesis;

⋆ **Christoph Fransen, Nigel Warr** for the technical support they gave so many times;

⋆ **Jens Klenke** for advices, discussions and help on many occasions;

⋆ **the staff of FRM 2, especially Christian Breunig, Jens Krüger, Jörg Pulz, Manual Stowasser and the team from the radiation protection office** for all the friendly and quick help on multiple occasions.

⋆ Special thanks to **Tina Tosetti**, **Petra Kudějová, Thomas Materna, Lea Canella,** and **Gunnar Frießner** for proof-reading my thesis.

⋆ Thanks to **my parents and my sister** for their support during my complete studies.

⋆ Most of all I thank **Tina Tosetti** for always being there for me.

List of Figures

List of Tables

Bibliography

[Alf95] ALFASSI, Z. B. and C. CHUNG, eds.; *Prompt Gamma Neutron Activation Analysis*; CRC Press, Boca Raton, Florida (**1995**); ISBN 978-0849351495

[Anc08] ANCIENT CHARM COLLABORATION; *Ancient Charm Periodic Activity Report*; Tech. Rep. (**2008**); internal document

[Bae01] BAECHLER, S., T. MATERNA, J. JOLIE, P. CAUWELS, M. CRITTIN, V. HONKIMAKI, H. U. JOHNER, B. MASSCHAELE, W. MONDELAERS, J. KERN, and M. PIBOULEE; *Non-destructive analysis of a bulky sample from a natural fossil reactor*; Journal of Radioanalytical and Nuclear Chemistry (**2001**); 250(1), 38–45; doi:10.1023/A:1013255912430

[Bae03] BAECHLER, S., P. KUDĚJOVÁ, J. JOLIE, and J.-L. SCHENKER; *The k_0-method in cold-neutron PGAA*; Journal of Radioanalytical and Nuclear Chemistry (**2003**); 256(2), 239–245; doi:10.1023/A:1023977015725

[Bal96] BALOGUN, F. A., N. M. SPYROU, and C. A. ADESANMI; *Neutron induced gamma-ray emission tomography*; Nuclear Instruments and Methods in Physics Research Section B: Beam Interactions with Materials and Atoms (**1996**); 114(3-4), 387–393; doi:10.1016/0168-583X(96)00150-4

[Bal07] BALLHAUSEN, H.; *Methoden und Anwendungen fur bildgebende Verfahren mit hohen Neutronenflüssen*; Ph.D. thesis; Ruprecht-Karls-Universität; Heidelberg (**2007**)

[Bel06] BELGYA, T. and Z. KASZTOVSZKY; *Half thickness for gamma radiation and for thermal neutrons in various materials*; Institute of Isotopes Hungarian Academy of Sciences, Budapest, Hungary (**2006**)

[Bel07] BELGYA, T., Z. KIS, L. SZENTMIKLÓSI, Z. KASZTOVSZKY, G. FESTA, L. ANDREANELLI, M. DE PASCALE, A. PIETROPAOLO, P. KUDĚJOVÁ, R. SCHULZE, T. MATERNA, and THE ANCIENT CHARM COLLABORATION; *Working PGAI/NT system*; Deliverable report; The Ancient Charm collaboration (**2007**)
http://ancient-charm.neutron-eu.net/FILES/DeliverableD3.pdf

[Bel08a] BELGYA, T., Z. KIS, L. SZENTMIKLÓSI, Z. KASZTOVSZKY, G. FESTA, L. ANDREANELLI, M. P. PASCALE, A. PIETROPAOLO, P. KUDĚJOVÁ, R. SCHULZE, T. MATERNA, and THE ANCIENT CHARM COLLABORATION;

A new PGAI-NT setup at the NIPS facility of the Budapest Research Reactor; Journal of Radioanalytical and Nuclear Chemistry (**2008**); 278(3), 713–718; doi:10.1007/s10967-008-1510-0

[Bel08b] BELGYA, T., Z. KIS, L. SZENTMIKLÓSI, Z. KASZTOVSZKY, P. KUDĚJOVÁ, R. SCHULZE, T. MATERNA, G. FESTA, P. A. CAROPPI, and THE ANCIENT CHARM COLLABORATION; *First elemental imaging experiments on a combined PGAI and NT setup at the Budapest Research Reactor*; Journal of Radioanalytical and Nuclear Chemistry (**2008**); 278(3), 751–754; doi:10.1007/s10967-008-1605-7

[Bel08c] BELGYA, T. and THE ANCIENT CHARM COLLABORATION; *Workpackage 2 Progress Report*; in *Ancient Charm Periodic Activity Report*; pp. 39–40 (**2008**); internal document

[Bra56] BRACEWELL, R. N.; *Strip Integration in Radio Astronomy*; Australian Journal of Physics (**1956**); 9, 198–217
http://adsabs.harvard.edu/abs/1956AuJPh...9..198B

[Bra08] BRAUN, N.; *Study of collectivity in* ^{88}Zr *with the* HORUS *spectrometer*; Master's thesis; Institute for Nuclear Physics; Cologe (**2008**)

[Bra10] BRAUN, N., T. KOTTHAUS, and R. SCHULZE; *HDTV - a proposed successor to TV*; Project website (**2010**)
http://www.ikp.uni-koeln.de/projects/hdtv/

[Byr95] BYRNE, J.; *Neutrons, Nuclei and Matter*; Institute of Physics Publishing, Bystrol and Philadelphia (**1995**)

[Can09] CANELLA, L., P. KUDĚJOVÁ, R. SCHULZE, A. TÜRLER, and J. JOLIE; *PGAA, PGAI and NT with cold neutrons: Test measurement on a meteorite sample*; Applied Radiation and Isotopes (**2009**); 67, 2070–2074; doi:10.1016/j.apradiso.2009.05.008

[Can10] CANELLA, L., P. KUDĚJOVÁ, R. SCHULZE, A. TÜRLER, and J. JOLIE; *Characterisation and optimisation of the new Prompt Gamma-ray Activation Analysis (PGAA) facility at FRM II*; Nuclear Instruments and Methods in Physics Research, Section A (**2010**); (in preparation)

[Cor63] CORMACK, A. M.; *Representation of a Function by Its Line Integrals, with Some Radiological Applications*; Journal of Applied Physics (**1963**); 34(9), 2722–2727; doi:10.1063/1.1729798

[Cor89] CORTE, F., A. SIMONITS, A. WISPELAERE, and A. ELEK; *k0-Measurements and related nuclear data compilation for (n, γ) reactor neutron activation analysis*; Journal of Radioanalytical and Nuclear Chemistry Articles (**1989**); 133(1), 3–41; doi:10.1007/BF02039969

[Die04] DIERICK, M.; *Tomographic Imaging Techniques using Cold and Thermal Neutron Beams*; Ph.D. thesis; Universiteit Gent (**2004**)

[Ebe09] EBERT, M.; *Untersuchung archäologischer Objekte mit Neutronen*; Master's thesis; Universität zu Köln (**2009**)

[Fes08] FESTA, G., R. CATTANEO, and THE ANCIENT CHARM COLLABORATION; *Preparation and transport of archaeological samples*; Deliverable report; The Ancient Charm collaboration (**2008**)
http://ancient-charm.neutron-eu.net/FILES/Transport_Report_italian.pdf

[Fes09a] FESTA, G.; *Neutron-based imaging applied to Cultural Heritage*; Ph.D. thesis; Università degli studi di Roma 'Tor Vergata' (**2009**)

[Fes09b] FESTA, G., C. ANDREANI, M. P. DE PASCALE, R. SENESI, G. VITALI, S. PORCINAI, A. M. GIUSTI, R. SCHULZE, L. CANELLA, P. KUDEJOVA, M. MÜHLBAUER, B. SCHILLINGER, and THE ANCIENT CHARM COLLABORATION; *A nondestructive stratigraphic and radiographic neutron study of Lorenzo Ghiberti's reliefs from paradise and north doors of Florence baptistery*; Journal of Applied Physics (**2009**); 106(7); doi:10.1063/1.3204514

[Fre08] FREITAS, M. C., Z. RÉVAY, L. SZENTMIKLÓSI, I. DIONÍSIO, H. M. DUNG, and A. M. G. PACHECO; *Different methodologies in neutron activation to approach the full analysis of environmental and nutritional samples*; Journal of Radioanalytical and Nuclear Chemistry (**2008**); 278(2), 381–386; doi:10.1007/s10967-008-0804-6

[Gen00] GENNILOUD, L.; *Gamma-ray spectroscopy using the (n,γ) and (α,2nγ) reactions*; Ph.D. thesis; l'Université Fribourg; Fribourg, Suisse (**2000**)

[Gor07] GORINI, G. and THE ANCIENT CHARM COLLABORATION; *Ancient Charm: A research project for neutron-based investigation of cultural-heritage objects*; Il Nuovo Cimento (**2007**); 30(1), 47–58; doi:10.1393/ncc/i2006-10035-9

[Has06] HASSANEIN, R. K.; *Correction Methods for the quantitative evalutaion of thermal neutron tomography*; Ph.D. thesis; Swiss Federal Institute of Technology Zürich (**2006**); doi:10.3929/ethz-a-005273682

[Hib97] HIBIKI, T. and K. MISHIMA; *Prediction of measurement error due to low gray scale and spatial resolution of an imaging system on quantification of neutron radiographic image*; Nuclear Instruments and Methods in Physics Research Section A: Accelerators, Spectrometers, Detectors and Associated Equipment (**1997**); 388(1-2), 204–211; ISSN 0168-9002; doi:10.1016/S0168-9002(97)00315-X

[Hou73] HOUNSFIELD, G. N.; *Computerized transverse axial scanning (tomography): Part 1. Description of system*; Britisch Journal of Radiology (**1973**); 46(552), 1016–1022; doi:10.1259/0007-1285-46-552-1016

[Hun08] HUNGARIAN NATIONAL MUSEUM; *Datasheet for cultural heritage objects to be analysed*; Tech. Rep. (**2008**)
http://www.ace.hu/acharm/obj_datasheet_HNM.pdf

[IAE07] IAEA; *Database of prompt gamma-rays from slow neutron capture for elemental analysis*; Tech. Rep.; International Atomic Energy Agency; Vienna (**2007**)
http://www-pub.iaea.org/MTCD/publications/PDF/Pub1263_web.pdf

[Kak88] KAK, A. C. and M. SLANEY; *Principles of Computerized Tombgraphic Imaging*; IEEE Press, New York (**1988**)

[Kar03] KARDJILOV, N., S. BAECHLER, M. BASTÜRK, M. DIERICK, J. JOLIE, E. LEHMANN, T. MATERNA, B. SCHILLINGER, and P. VONTOBEL; *New features in cold neutron radiography and tomography Part II: applied energy-selective neutron radiography and tomography*; Nuclear Instruments and Methods in Physics Research Section A: Accelerators, Spectrometers, Detectors and Associated Equipment (**2003**); 501(2-3), 536–546; ISSN 0168-9002; doi:10.1016/S0168-9002(03)00423-6

[Kas06a] KASZTOVSKY, Z., T. BELGYA, and THE ANCIENT CHARM COLLABORATION; *Non-destructive Investigations of Cultural Heritage Objects with Guided Neutrons: The Ancient Charm Collaboration*; Archeometriai Műhely (**2006**); 1, 12–17
http://www.epa.hu/00800/00846/00006/pdf/AM-2006-1-KZS.pdf

[Kas06b] KASZTOVSZKY, Z., T. BELGYA, and THE ANCIENT CHARM COLLABORATION; *From PGAA to PGAI From Bulk Analysis to Elemental Mapping*; Archeometriai Műhely (**2006**); 2, 16–21
http://epa.niif.hu/00800/00846/00007/pdf/am-2006-2-kzs.pdf

[Kir08] KIRFEL, A.; *Construction and description of the UNIBONN black boxes*; Archeometriai Műhely (**2008**); 1, 21–34; ISSN HU 1786-27!X
http://www.ace.hu/am/2008_1/AM-08-01-AK.pdf

[Kis] KIS, Z., T. BELGYA, and L. SZENTMIKLÓSI; *PGAA results from Hungarian National Museum objects*; private communication

[Kis08] KIS, Z., T. BELGYA, L. SZENTMIKLÓSI, Z. KASZTOVSZKY, P. KUDĚJOVÁ, and R. SCHULZE; *Prompt Gamma Activation Imaging on 'black boxes' in the Ancient Charm Project*; Archeometriai Műhely (**2008**); 1, 41–60

[Kud05a] KUDĚJOVÁ, P.; *Two new installations for non-destructive sample analysis: PIXE and PGAA*; Ph.D. thesis; Universität zu Köln; Köln (**2005**)

[Kud05b] KUDĚJOVÁ, P., T. MATERNA, J. JOLIE, A. TÜRLER, P. WILK, S. BAECHLER, Z. KASZTOVSZKY, Z. RÉVAY, and T. BELGYA; *On the construction of a new instrument for cold-neutron prompt gamma-ray activation analysis at the FRM-II*; Journal of Radioanalytical and Nuclear Chemistry (**2005**); 265(2), 221–227; doi:10.1007/s10967-005-0812-8

[Kud08a] KUDĚJOVÁ, P., G. MEIERHOFER, K. ZEITELHACK, J. JOLIE, R. SCHULZE, A. TÜRLER, and T. MATERNA; *The new PGAA and PGAI facility at the research reactor FRM II in Garching near Munich*; Journal of Radioanalytical and Nuclear Chemistry (**2008**); 278(3), 691–695; doi:10.1007/s10967-008-1506-9

[Kud08b] KUDĚJOVÁ, P. and THE ANCIENT CHARM COLLABORATION; *Supports for accurate positioning and alignment of archaeological objects*; Deliverable report; The Ancient Charm collaboration (**2008**)
http://ancient-charm.neutron-eu.net/FILES/AC_DeliverableD04_final.pdf

[Lin03] LINDSTROM, R. M.; *Using k_0 in PGAA: Perspectives*; Journal of Radioanalytical and Nuclear Chemistry (**2003**); 257(3), 557–560; doi:10.1023/A:1025488514894

[Mat03] MATTEINIA, M., C. LALLIA, I. TOSINIA, A. GIUSTIA, and S. SIANO; *Laser and chemical cleaning tests for the conservation of the Porta del Paradiso by Lorenzo Ghiberti*; Journal of Cultural Heritage (**2003**); 4, 147–151; doi:10.1016/S1296-2074(02)01190-1

[Mat06] MATERNA, T., B. BRUYNEEL, J. JOLIE, A. LINNEMANN, N. WARR, H. G. BÖRNER, M. JENTSCHEL, P. MUTTI, and G. SIMPSON; *Corrective optics for diffraction of γ-rays*; Nuclear Instruments and Methods in Physics Research Section A: Accelerators, Spectrometers, Detectors and Associated Equipment (**2006**); 569(3), 890–893; ISSN 0168-9002; doi:10.1016/j.nima.2006.08.131
http://www.sciencedirect.com/science/article/B6TJM-4M33SJM-5/2/ad6893d766c344e000bad60fbab27a15

[MO10] MODBUS-ORGANIZATION; *Modbus protocol*; Website (**2010**)
http://www.modbus.org/specs.php

[Mol98] MOLNÁR, G. L., Z. RÉVAY, R. L. PAUL, and R. M. LINDSTROM; *Prompt-gamma activation analysis using the k_0 approach*; Journal of Radioanalytical and Nuclear Chemistry (**1998**); 234(1-2), 21–26; doi:10.1007/BF02389741

[Mol04] MOLNÁR, G. L., ed.; *Handbook of Prompt Gamma Activation Analysis with Neutron Beams*; Kluwer Academic Publishers (**2004**); ISBN 1-4020-1304-3

[Mug81] MUGHABGHAB, S. F., M. DIVADEENAM, and N. E. HOLDEN; *Neutron Resonance Parameters and Thermal Cross Sections, Part A, Z=1-60*; vol. 1 of *Neutron Cross Sections*; Academic Press, New York (**1981**)

[Mug84] MUGHABGHAB, S. F.; *Neutron Resonance Parameters and Thermal Cross Sections, Part B, Z=61-100*; vol. 1 of *Neutron Cross Sections*; Academic Press, New York (**1984**)

[Pan83] PAN, S. and A. KAK; *A computational study of reconstruction algorithms for diffraction tomography: Interpolation versus filtered-backpropagation*; IEEE Transactions on Acoustics, Speech and Signal Processing (**1983**); 31(5), 1262 – 1275

[Pas] PASCOVICI, G. and C. GÖRGEN; *Cologne MCA specificactions*; private communication

[Pau95] PAUL, R. L.; *The use of element ratios to eliminate analytical bias in cold neutron prompt gamma-ray activation analysis*; Journal of Radioanalytical and Nuclear Chemistry Articles (**1995**); 191(2), 245–256; doi:10.1007/BF02038220

[Pau00] PAUL, R. L. and R. M. LINDSTROM; *Prompt gamma-ray activation analysis: Fundamentals and applications*; Journal of Radioanalytical and Nuclear Chemistry (**2000**); 243(1), 181–189; doi:10.1023/A:1006796003933

[PC07] PERELLI-CIPPO, E. and THE ANCIENT CHARM COLLABORATION; *Design of neutron and gamma collimators for PGAI/NT*; Deliverable report; The Ancient Charm collaboration (**2007**)
http://ancient-charm.neutron-eu.net/FILES/DeliverableD8.pdf

[PC08] PERELLI-CIPPO, E., G. GORINI, M. TARDOCCHI, R. CATTANEO, N. J. RHODES, E. M. SCHOONEVELD, T. NAKAMURA, P. RADAELLI, W. A. KOCKELMANN, A. PIETROPAOLO, and THE ANCIENT CHARM COLLABORATION; *Simulations and design of detectors for imaging with epithermal neutrons*; Measurement Science and Technology (**2008**); 19(3), 034027; doi:10.1088/0957-0233/19/3/034027

[PC09a] PERELLI-CIPPO, E. and THE ANCIENT CHARM COLLABORATION; *Design and GEANT4 simulations of a neutron collimator optimized for NRCI at the INES beamline*; Deliverable report; The Ancient Charm collaboration (**2009**)
http://ancient-charm.neutron-eu.net/FILES/Report_collimatore_NRCI.pdf

[PC09b] PERELLI-CIPPO, E. and THE ANCIENT CHARM COLLABORATION; *Simulated response of NRCI gamma detector bank*; Deliverable report; The Ancient Charm collaboration (**2009**)
http://ancient-charm.neutron-eu.net/FILES/D9.pdf

[PCO08] PCO; *PCO.1600 camera product details*; Kelheim, Germany (**2008**)
http://www.pco.de/sensitive-cameras/pco1600/

[Pil07] PILZ; *PNOZ m0p datasheet* (**2007**)
http://www.pilz.com/imperia/md/content/documentation/offen/sich/datenblatt/pnoz_m0p/PNOZ_m0p_en.pdf?redirected=true

[Por] PORCINAI, S.; private communication

[Pyt10] PYTHON SOFTWARE FOUNDATION; *The Python Standard Library: xmlrpclib – XML-RPC client access* (**2010**)
http://docs.python.org/library/xmlrpclib.html

[Rad17] RADON, J.; *Über die Bestimmung von Funktionen durch ihre Integralwerte längs gewisser Mannigfaltigkeiten*; Berichte der Säschsischen Akademie der Wissenschaften (**1917**); 69, 262–277; see [Rad86] for translated publication

[Rad86] RADON, J.; *On the Determination of Functions from Their Integral Values along Certain Manifolds*; IEEE Transactions on Medical Imaging (**1986**); 5(4), 170; doi:10.1109/TMI.1986.4307775; translation of [Rad17]

[Rai10] RAIMBAULT, S.; *A Modbus library for Linux, Mac OS X and FreeBSD*; Project website (**2010**)
http://github.com/stephane/libmodbus

[RC10] RIVERBANK-COMPUTING; *PyQt* (**2010**)
http://www.riverbankcomputing.co.uk/software/pyqt

[Sch99] SCHILLINGER, B.; *Neue Entwicklungen zu Radiographie und Tomographie mit thermischen Neutronen und zu deren routinemäsigem Einsatz*; Ph.D. thesis; Technischen Universität München (**1999**)

[Sch08] SCHULZE, R. and G. MEIERHOFER; *Dokumentation der Sicherheitsschaltung (PGAA-Station)* (**2008**); internal document

[Sch09] SCHULZE, R. and THE ANCIENT CHARM COLLABORATION; *Calibration objects, software tools and calibration procedure*; Deliverable report; The Ancient Charm collaboration (**2009**)
http://ancient-charm.neutron-eu.net/FILES/D15.pdf

[Sch10] SCHULZE, R., T. MATERNA, and THE ANCIENT CHARM COLLABORATION; *Software for integrated reconstruction of data from PGAI/NT and NRCI/NRT*; Deliverable report; The Ancient Charm collaboration (**2010**) http://ancient-charm.neutron-eu.net/FILES/DeliverableD16_Final.pdf

[Sia03] SIANO, S., R. SALIMBENI, R. PINI, A. GIUSTI, and M. MATTEINI; *Laser cleaning methodology for the preservation of the Porta del Paradiso by Lorenzo Ghiberti*; Journal of Cultural Heritage (**2003**); 4, 140; doi:10.1016/S1296-2074(02)01138-X

[Sim75] SIMONITS, A., F. DE CORTE, and J. HOSTE; *Simonits1974 - Single-comparator methods in NAA*; Journal of Radioanalytical Chemistry (**1975**); 24, 31–46; doi:10.1007/BF02514380

[SK87] SPYROU KUSMINARTO, N. M. and G. E. NICOLAOU; *2-D reconstruction of elemental distribution within a sample using neutron capture prompt gamma-rays*; Journal of Radioanalytical and Nuclear Chemistry Articles (**1987**); 112(1), 57–64; doi:10.1007/BF02037276

[Spy87] SPYROU, N. M.; *Prompt and delayed radiation measurements in the elemental analysis of biological materials: The case for neutron induced gamma-ray emission tomography*; Journal of Radioanalytical and Nuclear Chemistry (**1987**); 110(2), 641–653; doi:10.1007/BF02035553

[Sze08a] SZENTMIKLÓSI, L.; *Combining prompt gamma activation analysis and off-line counting*; Journal of Radioanalytical and Nuclear Chemistry (**2008**); 278(3), 657–660; doi:10.1007/s10967-008-1404-1

[Sze08b] SZENTMIKLÓSI, L., Z. KIS, T. BELGYA, Z. KASZTOVSZKY, P. KUDĚJOVÁ, T. MATERNA, R. SCHULZE, and THE ANCIENT CHARM COLLABORATION; *A new PGAI-NT setup and elemental imaging experiments at the Budapest Research Reactor* (**2008**) NRC7 - Seventh International Conference on Nuclear and Radiochemistry

[The94] THEUERKAUF, J.; *Die Analyse von zwei- und mehrdimensionalen $\gamma\gamma$-Koinzidenzen: Beispiele aus Hochspinexperimenten in der Massengegend um* ^{146}Gd; Ph.D. thesis; Institute für Kernphysik, Universität zu Köln; Köln (**1994**)

[Tri06] TRINAMIC; *BB-301S Manual*; Hamburg, Germany; 1.01 edn. (**2006**) http://www.trinamic.com/tmc/media/Downloads/modules/Baseboards/BB-301S_manual.pdf

[Tri07] TRINAMIC; *TMCM-301 manual*; Hamburg, Germany; 1.13 edn. (**2007**) http://www.trinamic.com/tmc/media/Downloads/modules/TMCM-301/TMCM-301_manual.pdf

[Tri08a] TRINAMIC; *TMCL reference and programming manual*; Hamburg, Germany; 2.22 edn. (**2008**)
http://www.trinamic.com/tmc/media/Downloads/modules/TMCL/TMCL_reference.pdf

[Tri08b] TRINAMIC; *TMCM-301 3-axis controller specification*; Hamburg, Germany (**2008**)
http://www.trinamic.com/tmc/media/Downloads/modules/TMCM-301/TMCM-301_ShortSpec.pdf

[Tri10] TRINAMIC; *BB-301S baseboard for stepper motors specification*; Hamburg, Germany (**2010**)
http://www.trinamic.com/tmc/media/Downloads/modules/Baseboards/BB-301_ShortSpec.pdf

[US03] USERLAND-SOFTWARE; *XML-RPC specification* (**2003**)
http://www.xmlrpc.com/spec

[Yon96] YONEZAWA, C.; *Multi-Element Determination by a Cold Neutron-Induced Prompt Gamma-Ray Analysis.*; Analytical Sciences (**1996**); 12(4), 605–613; doi:10.2116/analsci.12.605

Ich versichere, dass ich die von mir vorgelegte Dissertation selbstständig angefertigt, die benutzten Quellen und Hilfsmittel vollständig angegeben und die Stellen der Arbeit — einschließlich Tabellen, Karten und Abbildungen —, die anderen Werken im Wortlaut oder dem Sinn nach entnommen sind, in jedem Einzelfall als Entlehnung kenntlich gemacht habe; dass diese Dissertation noch keiner anderen Fakultät oder Universität zur Prüfung vorgelegen hat; dass sie — abgesehen von unten angegebenen Teilpublikation — noch nicht veröffentlicht worden ist sowie, dass ich eine solche Veröffentlichung vor Abschluss des Promotionsverfahrens nicht vornehmen werde.

Die Bestimmungen der Promotionsordnung sind mir bekannt. Die von mir vorgelegte Dissertation ist von Prof. Dr. J. Jolie betreut worden.

Köln, 22. Juli 2010

Ralf Schulze

Teilpublikationen

BELGYA, T., Z. KIS, L. SZENTMIKLÓSI, Z. KASZTOVSZKY, G. FESTA, L. ANDREANELLI, M. P. PASCALE, A. PIETROPAOLO, P. KUDĚJOVÁ, R. SCHULZE, and T. MATERNA; *A new PGAI-NT setup at the NIPS facility of the Budapest Research Reactor*; Journal of Radioanalytical and Nuclear Chemistry (**2008**); 278(3), 713–718

BELGYA, T., Z. KIS, L. SZENTMIKLÓSI, Z. KASZTOVSZKY, P. KUDĚJOVÁ, R. SCHULZE, T. MATERNA, G. FESTA, P. A. CAROPPI, and THE ANCIENT CHARM COLLABORATION; *First elemental imaging experiments on a combined PGAI and NT setup at the Budapest Research Reactor*; Journal of Radioanalytical and Nuclear Chemistry (**2008**); 278(3), 751–754

FESTA, G., C. ANDREANI, M. P. DE PASCALE, R. SENESI, G. VITALI, S. PORCINAI, A. M. GIUSTI, R. SCHULZE, L. CANELLA, P. KUDĚJOVÁ, M. MÜHLBAUER, B. SCHILLINGER, and THE ANCIENT CHARM COLLABORATION; *A nondestructive stratigraphic and radiographic neutron study of Lorenzo Ghiberti's reliefs from paradise and north doors of Florence baptistery*; Journal of Applied Physics (**2009**); 106(7)

KIS, Z., T. BELGYA, L. SZENTMIKLÓSI, Z. KASZTOVSZKY, P. KUDĚJOVÁ, and R. SCHULZE; *Prompt Gamma Activation Imaging on 'black boxes' in the Ancient Charm Project*; Archeometriai Műhely (**2008**); 1, 41–60

SCHULZE, R. and THE ANCIENT CHARM COLLABORATION; *Calibration objects, software tools and calibration procedure*; Deliverable report; The Ancient Charm collaboration (**2009**)

SCHULZE, R. and THE ANCIENT CHARM COLLABORATION; *Software package for alignment and visualization of multiple 3D image data sets*; Deliverable report; The Ancient Charm collaboration (**2009**)

SCHULZE, R., T. MATERNA, and THE ANCIENT CHARM COLLABORATION; *Software for integrated reconstruction of data from PGAI/NT and NRCI/NRT*; Deliverable report; The Ancient Charm collaboration (**2010**)

SZENTMIKLÓSI, L., Z. KIS, T. BELGYA, Z. KASZTOVSZKY, P. KUDĚJOVÁ, T. MATERNA, R. SCHULZE, and THE ANCIENT CHARM COLLABORATION; *A new PGAI-NT setup and elemental imaging experiments at the Budapest Research Reactor* (**2008**)NRC7 - Seventh International Conference on Nuclear and Radiochemistry